8-1-2014

Speciation Behavior of Americium Higher Oxidation States for the Separation of Americium from Curium

Catherine Lynn Riddle
University of Nevada, Las Vegas, riddlec6@unlv.nevada.edu

SPECIATION BEHAVIOR OF AMERICIUM HIGHER OXIDATION STATES FOR THE SEPARATION OF AMERICIUM FROM CURIUM

by

Catherine Lynn Riddle

Bachelor of Science in Chemistry
Idaho State University
2000

Master of Science in Chemistry
University of Idaho
2005

A dissertation submitted in partial fulfillment
of the requirements for the

Doctor of Philosophy - Radiochemistry

Department of Chemistry
College of Sciences
The Graduate College

University of Nevada, Las Vegas
August 2014

UNLV
UNIVERSITY OF NEVADA LAS VEGAS

THE GRADUATE COLLEGE

We recommend the dissertation prepared under our supervision by

Catherine Lynn Riddle

entitled

Speciation Behavior of Americium Higher Oxidation States for the Separation of Americium from Curium

is approved in partial fulfillment of the requirements for the degree of

Doctor of Philosophy - Radiochemistry
Department of Chemistry

Kenneth R. Czerwinski, Ph.D., Committee Chair

Gordon Jarvinen, Ph.D., Committee Member

Patricia Paviet-Hartmann, Ph.D., Committee Member

Ralf Sudowe, Ph.D., Graduate College Representative

Kathryn Hausbeck Korgan, Ph.D., Interim Dean of the Graduate College

August 2014

ABSTRACT

Speciation Behavior of Americium Higher Oxidation States for the Separation of Americium from Curium

by

Catherine Lynn Riddle

Dr. Kenneth R. Czerwinski, Examination Committee Chair
Professor of Chemistry
Radiochemistry Program Director
University of Nevada, Las Vegas

Several countries are currently expanding the use of nuclear energy as a method for the safe generation of carbon free energy and a number are evaluating starting up a nuclear power program. Closed fuel cycle technologies may be key to waste reduction and a sustainable nuclear energy future and to support the development of more efficient fuel cycles, the investigation of the chemical properties of key actinides is at the forefront of separations research. In this work the characterization of higher oxidation states of americium (Am) has been performed using spectroscopic methods. Americium in the formal oxidation state of Am(V) has been prepared by oxidation of Am(III) to Am(VI) in acid solution using sodium bismuthate ($NaBiO_3$) followed by reduction of Am(VI) to Am(V). The oxidation state and stereochemical arrangements of atoms in close proximity to Am have been determined by x-ray absorption fine structure spectroscopy (XAFS), consisting of EXAFS (extended x-ray absorption fine structure spectroscopy) and XANES (x-ray absorption near-edge spectroscopy) analysis. Density Functional Theory (DFT) was used to create a model of Am(V) and Am(VI) using the data from these studies. Future work should focus on using this knowledge of Am higher oxidation states to design new more selective extraction processes for the separation of Am from

curium (Cm) as well as lanthanide fission products from actinides in used nuclear fuel reprocessing and recycling.

ACKNOWLEDGMENTS

The demands associated with graduate school take on new meaning when they are balanced with being a full time staff scientist at a national laboratory. It has been a delicate balance between home, work, and school and I am thankful for the support of friends, colleagues, and family who joined me on this adventure. I would like to thank the members of my examination committee, Dr. Ken Czerwinski, Dr. Patricia Paviet, Dr. Gordon Jarvinen, and Dr. Ralf Sudowe for their encouragement, inspiration, and dedicated support of my goals. Many thanks to my fellow graduate students and staff; Nick Smith, Narek Gharibyan, Dallas Reilly, Keri Campbell, Janelle Droessler, Maryline Ferrier, Ed Mausolf, Audrey Roman, Wendee Johns, and all of the radchemstuds for helping me more than you know and making me feel like one of the group whether I was on campus or in Idaho, you are all awesome! Thank you to Dr. Frederic Poineau and Dr. Steven Conradson for pointers on XAFS and also to Dr. Philippe Weck and Dr. Eunja Kim for showing me how cool DFT is! To my colleagues at INL; Bruce Mincher, John Baker, Chris McGrath, Leigh Martin, Peter Zalupski, Dean Peterman, Travis Grimes, Rockland McDowel, Dawn Scates, Jacqueline Fonnesbeck, Jack Law and Terry Todd; thank you for pushing my limits and persevering with me, it is my great privilege to count you among my friends. I would also like to thank DOE and INL Nuclear Science and Technology Division for funding this work under contract DE-AC07-05ID14517.

Finally, to my husband Glen, you never let me give up…thank you. This was a journey I had to take, but you were not obligated to come along, and yet you did willingly, with enthusiasm, support and the courage I sometimes could not find in myself. You will always have my love, respect, and undying appreciation.

In Memory of John D. Baker

1947 – 2009

Mentor, Colleague, and Friend…I will miss our conversations.

TABLE OF CONTENTS

LIST OF TABLES

LIST OF FIGURES

LIST OF ACRONYMS

ANL	Argonne National Laboratory
AP	Aqueous Polishing
APS	Advanced Photon Source
ATW	Accelerated Transmutation of Nuclear Waste
BESSRC-CAT	Basic Energy Sciences Synchrotron Radiation Center Collaborative Access Team
CCD	Charge-Coupled device
DFT	Density Functional Theory
DOE	Department of Energy
EC	Electron Capture
EXAFS	Extended X-ray Absorption Fine Structure
FP	Fission Product
FPEX	Fission Product Extraction
GGA	Generalized Gradient Approximation
GC	Gradient Corrected
HLW	High Level Waste
INL	Idaho National Laboratory
LDA	Local Density Approximation
LLFP	Long-Lived Fission Products
LLW	Low Level Waste
LRO	Long Range Order
LWR	Light Water Reactor
MFFF	Mixed Oxide Fuel Fabrication Facility
MOX	Mixed Oxide
NE	Nuclear Energy
NEXAFS	Near Extended X-ray Absorption Fine Structure
NNSA	National Nuclear Security Administration
PUREX	Plutonium and Uranium Recovery by Extraction
SESAME	Selective Extractions of Americium by Electrochemical Method
SF	Spontaneous Fission
SRNL	Savannah River National Laboratory
SRO	Short Range Order
SRS	Synchrotron Radiation Sources
SSRL	Stanford Synchrotron Radiation Lightsource
TALSPEAK	Trivalent Actinide-Lanthanide Separations by Phosphorus reagent Extraction from Aqueous Complexes
TRUEX	Transuranic Extraction
UREX	Uranium Extraction
XAFS	X-ray Absorption Fine Structure
XANES	X-ray Absorption Near Edge Structure
XRD	X-ray Diffraction

CHAPTER 1

INTRODUCTION

Nuclear energy supplies approximately 20 percent of the Nation's electricity and over 70 percent of the clean, non-carbon emitting electricity. As of January 2014, there were 100 nuclear power plants currently operating within the United States, providing reliable and affordable base load electricity without air pollution or emissions of greenhouse gases [1]. The long-term sustainability of nuclear power as a viable energy resource is largely dependent upon the optimization of the nuclear fuel cycle [2]. Key to the reprocessing or recycling of used nuclear fuel and production of transuranic fuel or targets is having in depth accurate models of the behavior of the minor actinides, especially americium (Am). High-level nuclear waste can generate considerable quantities of heat over a number of years after removal from a reactor. This is referred to as thermal or heat loading in a geological repository [3]. Heat limits for repositories are imposed to prevent damage to one or more barriers to radionuclide migration from the waste form to the accessible environment. Almost all repository decay heat from used nuclear fuel (UNF), shown in Figure 1, is produced from five elements: cesium (^{137}Cs), strontium (^{90}Sr), plutonium (Pu: multiple isotopes), Am (multiple isotopes), and Cm (multiple isotopes). There are other heat-generating radionuclides, but these decay away quickly and pose little addition to the heat loading. The high-heat radionuclides (HHRs) can be divided into two categories: shorter-lived HHRs (^{137}Cs and ^{90}Sr) and long-lived HHRs (Pu, Am, and Cm) [4].

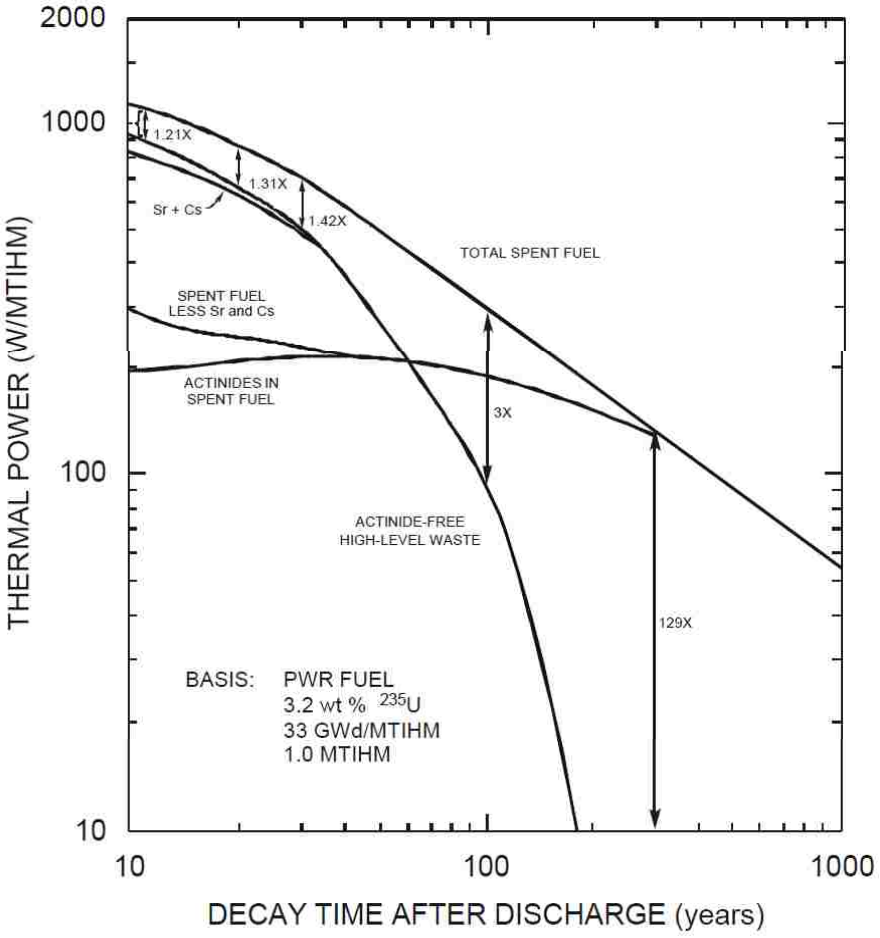

Figure 1 Decay heat from UNF [2]

For some repositories concepts, Am will need to be separated from the UNF with an efficiency of 99.9% to address the repository heat load issues [2]. Currently, interest in energy nuclear production has increased based upon two key factors: the desire to become independent from foreign energy sources and the goal of generating fewer greenhouse gas emissions [5]. At this time, policy makers are viewing nuclear energy as part of the mix for our future needs along with natural gas, renewable, and fossil fuel. The United States has embarked on a long-term program to significantly advance the science and technology of nuclear energy (NE) [6]. This is in response to the overall

national plan for accelerated development of domestic energy resources on several fronts, punctuated by recent dramatic events that have emphasized the need for the US to reduce its dependence on foreign petroleum supplies.

The planned efforts involve near-term and intermediate-term improvements in fuel utilization and reprocessing or recycling in current nuclear power reactor systems as well as the longer-term development of new nuclear energy systems that offer vastly improved fuel utilization, proliferation-resistance processes, reduced requirements for waste disposal, and continued advances in operational safety [7]. Reprocessing or recycling could cut storage costs by transmuting some very-long-lasting isotopes in the fuel cycle, allowing for storage of compact fission-product waste forms with less long-term heat within a facility or repository [3]. The success of the overall NE effort will depend not only on sophisticated system engineering, but also on advances in the supporting sciences and technologies for used nuclear fuel reprocessing or recycling.

In previous work [8-11], oxidation states have played a significant role in actinide separation chemistry especially since some actinides can exist simultaneously in more than one oxidation state, each with different chemical behavior. Therefore the control and determination of actinide oxidation states present in a particular system is of primary importance. Oxidation-reduction cycles for the separation of Am from Cm have shown promise in which the Am in solution is oxidized to the pentavalent (V) or hexavalent (VI) state, with Cm remaining trivalent (III) throughout [11]. The efficient separation of Am from Cm has become a significant goal in the reprocessing or recycling arena and to meet this goal the in-depth analysis of Am oxidation states is an important area of research. A clean separation of Am from Cm is necessary for the removal of isobaric interferences in

Cm isotopic analysis, which can enhance safeguards methods. Furthermore a facile separation of Am from trivalent fission product lanthanides would greatly simplify current designs for nuclear fuel cycle closure. Higher oxidation states of Am are known and provide opportunities for separations development, but few options for their production in acidic media are available [12].

This work contributes to modeling of Am higher oxidation states behavior that can be used to better design future separations with reduced cost relative to current approaches. It could potentially lead to new and novel paths for Am and Cm separations. It could also potentially answer questions concerning problems with current separation processes. Because other actinides share similar properties, the in depth analysis of Am higher oxidation state behavior could potentially allow us to evaluate trends in the actinides. This will expand foundational information on these elements and the 5f electrons. Detailed studies using X-ray Absorption Fine Structure (XAFS), Single Crystal X-ray Diffraction (XRD), and Density Functional Theory (DFT) will be used to better understand speciation and coordination chemistry of Am in higher oxidation states. By better understanding these actinide oxidation states, the next generation of solvent extraction systems for used nuclear fuel reprocessing or recycling will be more efficient, robust, and safer.

1.1 Dissertation Overview

Chapter 1 provides a general overview of the dissertation which includes the motivation and projects goals for this work. Chapter 2 gives background information on used nuclear fuel reprocessing or recycling and the need for investigation into higher

oxidation states. The analysis used in this work as well and information on experimental facilities related to the synchrotron beam necessary for XAFS measurements is also provided. Chapter 3 presents a detailed literature review of Am oxidation, crystallography, and DFT. Chapter 4 covers the analytical and spectroscopic techniques utilized in this work. Chapter 5, 6 and 7 provide experimental details followed by the presentation of results, discussions and future work for three different experiments related to speciation behavior of Am in higher oxidation states. The conclusions are covered in Chapter 8. The raw data of the results as presented in figures can be found in the Appendix.

1.2 Motivation for Research

Used Nuclear Fuel Reprocessing or Recycling

One of the benefits of reprocessing or recycling and closing the nuclear fuel is that it provides commercial utilities with an additional source of domestic nuclear fuel, thus providing a hedge against global uranium (U) prices and promoting energy security. Additionally, reprocessing or recycling "allows for early movement of freshly discharged used fuel from utilities' sites…and provides more efficient use of potential geologic repositories, avoiding the need for an additional repository beyond this century and expanding repository options" [13]. Finally, whether the future belongs to fast reactors or light water reactor (LWR), the behavior of minor actinides will remain an important issue in either system and is therefore an important topic.

Oxidation-reduction cycles for the separation of Cm from Am have shown the best promise and are used in solutions in which the Am is oxidized to the pentavalent or

hexavalent state, with Cm remaining trivalent [9]. A more in-depth characterization of higher oxidation states of Am is needed in an effort to understand the interaction of these oxidation states with respect to current and future separation schemes. Increasing the understanding of Am oxidation, especially kinetic behavior in the redox process, will provide flexibility in the development of transuranic separation schemes. This work will contribute to a better understanding of the chemical interactions of Am(V) and Am(VI) in acidic solution. Ultimately, an in-depth knowledge of these Am higher oxidation states will lead to a model of Am behavior for the design of next generation solvent extraction processes. This type of model, based on experimentally produced data and augmented by computation, will give researchers the ability to explore new areas for nuclear fuel design, actinide separations, and waste storage.

Reprocessing or recycling refers to the chemical partitioning of irradiated nuclear fuel. In industrial practice, this has primarily involved recovery of U and Pu from the used fuel. The World War II-era Manhattan Project developed reprocessing or recycling technology for Pu recovery in the successful effort to build the first atomic bomb. With the development of commercial nuclear power after the war, reprocessing or recycling was considered necessary because of a perceived scarcity of U. Federally sponsored breeder reactor development included research into advanced reprocessing or recycling technology. Several commercial interests in reprocessing or recycling foundered due to economic, technical, and regulatory issues. In 1977 President Carter terminated federal support for reprocessing or recycling in an attempt to limit the proliferation of nuclear weapons material and reprocessing or recycling for nuclear weapons production ceased, in the United States, shortly after the Cold War ended. The Department of Energy

currently proposes developing a new generation of "proliferation-resistant" reactors and reprocessing or recycling technology [14].

Most energy obtained from nuclear reactors comes from the naturally occurring fissionable isotope ^{235}U. Non-enriched U oxide contains 0.7% ^{235}U, a small amount of ^{234}U (0.0055% from the decay of ^{238}U), with the remaining majority of the material being composed of the isotope ^{238}U. After enrichment of the natural U to about 4% ^{235}U, the material can be converted into fuel rods that will be used in the core of a power reactor. When the fissionable U content of the fuel falls too low or the concentration of the neutron-absorbing fission products becomes too high, fuel rods are replaced and the fuel is defined as "used" [13]. Used LWR fuel usually contains about 96% U (mostly ^{238}U), 1% Pu, 0.1% minor actinides (Np, Cm, and Am), and 3% fission products. Only around 1% of the fission products pose long terms hazards. The U, which can be separated from the rest of the used fuel products, still has most of its fertile energy content and could be either reused or disposed of as low-level waste (LLW) [15].

Commercial-scale used nuclear fuel reprocessing or recycling is currently conducted in France, Britain, Japan and Russia, however, Japan's facility is currently shut down. The recycled ^{239}Pu is blended with U to make mixed-oxide (MOX) fuel [16], in which the fissile ^{239}Pu largely substitutes for ^{235}U. Two French reprocessing plants (UP 2-800 and UP 3) at La Hague can each reprocess up to 850 metric tons [15] of used nuclear fuel per year, while Britain's THORP facility at Sellafield has a capacity of 900 metric tons per year. Russia has a 400-ton plant at Ozersk, and Japan has an 800-ton plant at Rokkasho and a 90-ton demonstration facility at Tokai Mura which is currently not running. Major commercial reprocessing or recycling plants are operating worldwide

with a total capacity of over 4000 tons of used fuel per year [15]. The product from these re-enters the fuel cycle and is fabricated into fresh MOX fuel elements. About 200 tons of MOX is used each year, avoiding the need to obtain 2,000 tons of U_3O_8 for U isotope enrichment [16]. A few countries have chosen to reprocess used nuclear fuel for three reasons: first, there are no other energy resources available (such as France and Japan), second, reprocessing or recycling recovers significant energy value from used nuclear fuel that contributes to energy security, and third, reprocessing or recycling substantially reduces the volume and radiotoxicity of high-level nuclear waste [17]. The once-through nuclear fuel cycle, the current practice in the United States, is an enormous waste of potential energy as shown in Table 1.

Table 1 Composition of used nuclear fuel and different processes [18].

	Composition	Once Through	PUREX	UREX+ with ATW
Actinides				
Uranium	95.60%	Repository	Reused or LLW	Reused or LLW
Plutonium	0.90%	Repository	MOX Fuel	MOX or ATW
Minor Actinides	0.10%	Repository	Repository	
Fission Products				
Stable/Short Lived	3%	Repository	Repository	Repository
Cesium/Strontium	0.30%	Repository	Repository	Repository
Iodine/Technetium	0.10%	Repository	Repository	ATW

As mentioned previously, nuclear waste is over 90% U. Thus, the reactor raffinate still contains 90% usable U that can be chemically processed and placed in advanced fast reactors to *close the fuel cycle*. A closed fuel cycle means less nuclear waste will be produced and considerably more energy can be extracted from the raw ore [18]. Figure 2 depicts the build-up of decay products and the decay chains for minor

actinides which could be separated for fabrication of MOX fuel in a closed fuel cycle reprocessing or recycling scheme.

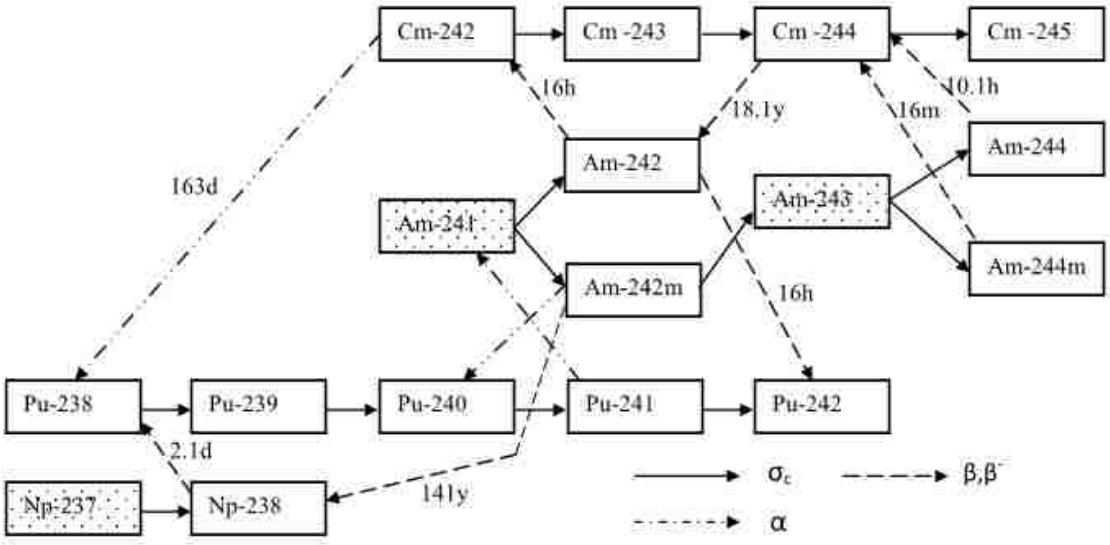

Figure 2 Buildup and decay chains for the minor actinides. Shaded boxes represent materials with long half-lives that make them of particular interest for transmutation [19].

Over the past two decades, various reprocessing or recycling schemes have been proposed for the extraction of actinides from fission products and other elements present in used nuclear fuel. The most current reprocessing or recycling schemes operate using a tri-*n*-butyl phosphate (TBP) based extractions including the PUREX process referred to in literature by the following excerpt, "As originally defined, PUREX was an acronym for Plutonium, Uranium, Reduction, Extraction. PUREX has also been defined by some authors to stand for PURification by EXtraction or for Plutonium and Uranium Refining by EXtraction. In recent times, at least in the US, PUREX is accepted as an acronym for Plutonium URranium Extraction." [20]. Plutonium and Uranium Recovery by Extraction

is considered the current standard used nuclear fuel reprocessing or recycling method [21]. The PUREX process is a liquid-liquid extraction method which exploits the redox properties of actinides selectively extracting actinide cations in even oxidation states IV and VI. Thus, PUREX is used to reprocess used nuclear fuel for the extraction of U and Pu, independent of each other, from the fission products. The irradiated fuel is first dissolved in nitric acid (HNO_3) and forms the aqueous solution phase. An organic solvent composed of 30% tributyl phosphate (TBP) in odorless kerosene or isoparaffinic diluent is used to recover the U and Pu while the fission products remain in the aqueous nitric phase as depicted in Figure 3.

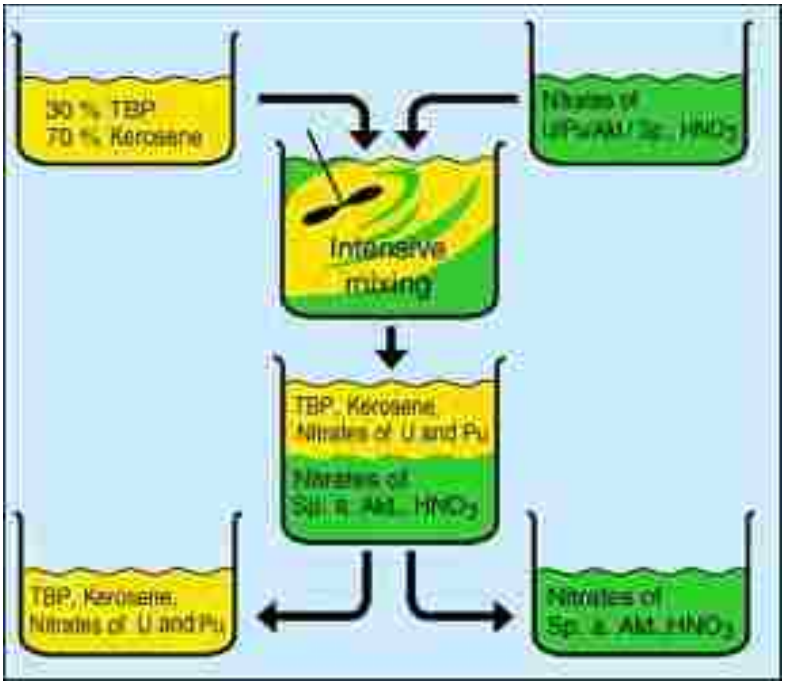

Figure 3 Principle of the PUREX process for the separation of uranium and plutonium from fission products [21].

Several countries have been using PUREX to recycle used nuclear fuel since the late 1950s. France has long made a practice of reprocessing or recycling its used nuclear fuel using PUREX and has developed storage facilities allowing for a 250 year strategic reserve of U [22]. Currently, reprocessing or recycling of 1150 tons of used fuel per year, including the weight of the metal cladding and fuel bundle structure, produces 8.5 tons of Pu and 815 tons of reprocessed U. Of this about 650 tons is converted into stable oxide form for storage. France began using the PUREX process in the Magnox plants at Marcoule in 1958 and at La Hague in 1967 where each plant processed ~400 MT/yr. In recent years, the French processing plants, UP2 (1976) and UP3 (1990) in La Hague, have been reprocessing or recycling 850 MT/yr initial weight of heavy metal of LWR fuel.

In liquid-liquid extraction, the immiscible organic and aqueous phases are contacted to perform the extraction. The complexes formed with the metal ions will partition into two phases until an equilibrium has been reached [23]. Once fission products are removed, further processing steps allow separation of Pu from U. The first steps in the PUREX process rely on solvent-exchange chemistry. The key is that after dissolving many transition metals and actinides in nitric acid, the addition of 30% TBP in an organic solvent results in the selective extraction of U and Pu [21]. This occurs because TBP preferentially coordinates to the UO_2^{2+} and Pu^{4+} in the presence of HNO_3, but not with most other cations such as di- and trivalent radionuclide products, Pu(III) or Np(V) [24].

The TBP is sparingly soluble in acidic water, but highly soluble (20% wt./wt. or more) in common organic solvents such as paraffin (kerosene). Therefore, agitating a

solution of dissolved nuclear fuel, HNO_3, TBP, and paraffin results in the transfer of $UO_2(NO_3)_2(TBP)_2$ and $Pu(NO_3)_4(TBP)_2$ complexes to the organic phase. The U and Pu complexes can be transferred back to aqueous media, resulting in solutions containing U and Pu, but not the other constituents of the original nuclear fuel [21]. The ratio of the concentrations of the complex in the phases is called the partition coefficient, K_d. The distribution ratio (D), is determined by equation 1-1:

$$D = \frac{[X]_{org}}{[X]_{aq}} \qquad \text{(Eq. 1-1)}$$

where $[X]_{org}$ and $[X]_{aq}$ are the concentration of the metal species in the organic phase and the aqueous phase, respectively. For the PUREX process, the partition coefficients for the distribution of U and Pu, Equation 1-2, are:

$$D_U = \frac{[UO_2(NO_3)_2 \bullet 2TBP]_{org}}{[U(VI)]_{aq}} \qquad D_{Pu} = \frac{[Pu(NO_3)_4 \bullet 2TBP]_{org}}{[Pu(IV)]_{aq}} \qquad \text{(Eq. 1-2)}$$

Where $[U(VI)]_{aq}$ and $[Pu(IV)]_{aq}$ represent all relevant aqueous species including free metal ions and nitrates. The PUREX process may find application as a preliminary separation step in processing actinide-containing wastes. Although it is probably not efficient enough to reach the very low levels required for removing actinides from wastes to the level necessary to make them non-TRU wastes, it could provide a suitably clean feed stream for a subsequent more efficient process [25-28].

Further spectroscopic characterization of Am(III,V,VI) will contribute new insight into the coordination number, bond distances, and speciation of these oxidation states. Including single crystal XRD for atomic level oxidation data and DFT for computational chemical analysis, along with XAFS, would add information coordination and speciation information useful for separations. This atomic level information that will be gained for Am higher oxidation states can be used to better understand what can be applied to future separation technologies based on fundamental behavior. It could potentially lead to new and novel paths for Am and Cm separations that could enhance current post PUREX processes or spawn new processes for actinide separations. An example of this is extraction under basic conditions, where the higher oxidation states are more stable. Because other actinides share similar properties, the in depth analysis of Am higher oxidation state behavior could potentially allow new conclusions to be drawn concerning the higher oxidation states trends of the actinides.

Additional information about Am in acidic solution and in a crystalline form can be gained through DFT calculations. The major advantages to using DFT methods include using property that exists in real molecules, not a just a mathematical simulation, and the wavefunction becomes more complicated mathematically as the number of electrons increases allowing an intricate electron density map of the molecule to be visualized. An overview of the DFT approach is provided in chapter 2.

Actinide and Lanthanide Separations

Accurate information on the interactions of Am in higher oxidation states will aid in actinide-actinide, lanthanide-lanthanide, and actinide-lanthanide separations. Managing Cm in a closed nuclear fuel cycle is a significant challenge, especially with

regard to handling this element in fabricating fast reactor fuels or targets [27]. One option is to separate the Cm from the other TRU elements and store it for decay. However, separating Am from Cm is a significant technical challenge because of the very similar chemistries of Am(III) and Cm(III). One key distinction between Am and Cm is that Am can be oxidized to a higher oxidation state in aqueous media. This difference in oxidation states (Table 2) can be exploited for both lanthanide and actinide separation schemes [25-27]. It is important in any separation process for fuel manufacturing that Am be removed from Cm since Cm is not a candidate for the development of MOX fuel due to its neutron production and neutron producing decay daughters such as ^{252}Cf (Figure 4) [29].

Table 2 Differences between lanthanides and actinides [29].

Lanthanides	**Actinides**
They have the ability to show a maximum oxidation state of + 4	Actinides show variable oxidation states of + 3, + 4, + 5, + 6 and + 7.
They have smaller tendency to form complexes.	They have a good tendency to form complexes with ligands such as thio-ethers.
All lanthanides are non-radioactive except promethium.	They are radioactive in nature.
They do not form oxo-ions	Actinides form oxo-ions such as UO_2^{2+}, NpO_2^{+}.

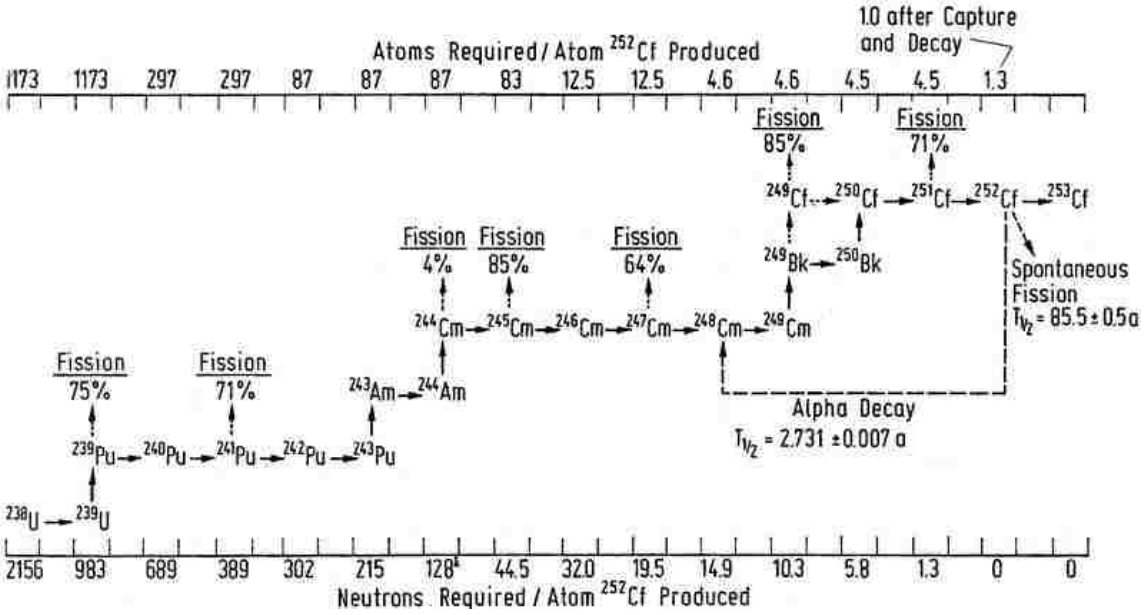

Figure 4 Scheme of the production of ^{252}Cf from ^{238}U by neutron irradiation.

The accessibility of the higher Am oxidation states can be exploited to separate Am from Cm, but the higher Am oxidation states are difficult to maintain [10]. Stabilizing either Am(V) or Am(VI) by using new oxidizing agents that do not complex with actinides, but instead act as a holding agent will be preferable to complexing with ligands selective for linear trans-dioxo actinyl ions due to stability issues related to radiolysis [30] and overall selectivity. To better understand how a holding agent inhibits the reduction of higher oxidation states of Am, it is necessary to study the redox reactions of Am(V/VI) in acidic aqueous solution.

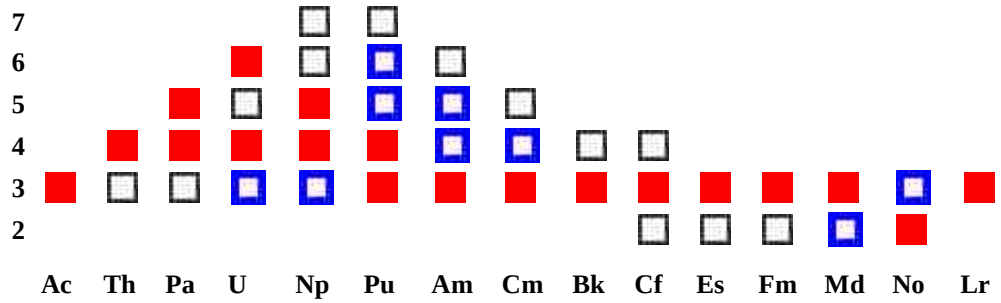

Figure 5 Known oxidation states of the actinides. Importance: ■ > ▣ > □

The known oxidation states of the actinides, and their relative importance in separation chemistry, are indicated in Figure 5. The separation of early actinides from fission products and from each other is generally accomplished by adjusting the oxidation state of the actinide ion in aqueous solution. This makes the coordination chemistry of the actinide ion substantially different from the other species to be separated [30]. The actinides are highly electropositive metals and form cationic species in aqueous solutions. These cations are hard Lewis acids and form strong complexes in solution with hard anions such as hydroxide and fluoride [31]. The oxidation states from III to VI are accessible in aqueous acidic solutions of U, Np, Pu, and Am. Actinides after Pu become more lanthanide-like with the coordination chemistry of the trivalent metal ion dominating. The pentavalent and hexavalent actinide ions are found in aqueous solutions as linear dioxo cations, such as NpO_2^+ and AmO_2^{2+} [32]. There are large differences in the coordination chemistry of actinide ions in solution due to the oxidation states making separation possible.

1.3 Project Goals

Overall Project

A systematic analysis of the effect of complex formation during the oxidation/reduction phase will provide new information on the behavior of different oxidation states of Am for the ultimate separation of Am from Cm. Although higher oxidation states of actinides have been studied for some time, only a limited number of studies on Am species using XAFS have been performed [33]. Even less work has been reported on single crystal of either Am(V) or Am(VI) [34]. The goal of this work is to spectroscopically characterize Am(V) and Am(VI) to evaluate the formal oxidation states and coordination chemistry, single crystal XRD to evaluate the structure, and DFT computational chemistry for molecular/electronic structure. Exploring the chemistry of Am higher oxidation states can be used to better understand what can be applied to future separations technologies. It could potentially lead to new and novel paths for Am and Cm separations. Because other actinides share similar properties, the in-depth analysis of Am higher oxidation state could potentially allow new conclusions to be drawn concerning the oxidation states of U, Pu, and Np. Using XAFS and DFT to unravel the behavior of higher oxidation states of Am and other actinides will help to develop more efficient separation systems used nuclear fuel reprocessing or recycling.

XAFS of Am(V/VI) Oxidation States

To facilitate the next generation of used nuclear fuel reprocessing or recycling processes, an in-depth characterization of Am(V) and Am(VI) is needed for a standardized atomic level model. The proposed characterization method involves using X-ray absorption fine structure spectroscopy (XAFS) analysis that examines the

stereochemical arrangements of atoms in close proximity to Am in different oxidation states.

XRD Analysis of Am (V) Crystal

The growth of these crystals and subsequent analysis with single crystal X-ray diffraction (XRD) will play an important role in the characterization of oxidized Am species. Single crystals can be used to determine compound coordination chemistry. In general, the electronic structure of a crystalline solid governs bonding, magnetism, and elasticity. Preliminary work will focus on the synthesis of an Am(V) crystal through multiple experimental routes and with actinide analogs for development of a satisfactory crystal synthesis procedure.

Computational Studies of Am(V/VI)

Density Functional Theory will be used to investigate the electronic structure for the oxidized states of Am. By incorporating the experimental structural information, it will be possible to derive properties for Am(V/VI) in a range from atoms, molecules, solids and solutions based on a determination of the electron density. Using this computational chemistry method the properties of a many-electron system for Am can be determined adding further information on the behavior of oxidized Am. In this study several variants of spin density functional theory including scalar relativistic corrections will be used to investigate the Am-containing systems. The exchange correlation will be calculated using both generalized gradient approximation (GGA) and hybrid functionals and a systematic comparison of their impact on the properties of the molecular systems will be carried out. The DFT implemented in the $DMol^3$ and Gaussian09 software will be used for most of the calculations [35].

CHAPTER 2

BACKGROUND

This chapter provides background information on the primary methods utilized in this work: Am oxidation and DFT. The last section gives a brief overview of the facilities used for Am oxidation work as well as for XAFS and single crystal XRD analysis.

2.1 Americium Oxidation

Separation techniques employing differences in oxidation states are very common for both radiochemical and non-radiochemical processes [34, 36-39]. Due to distinct differences in the chemical makeup and behavior of different oxidation states, it is possible to easily partition one state from another. Many methods are available to separate one element from another using higher oxidation states including liquid-liquid extraction, ion chromatography, and precipitation.

After the discovery of Am and its addition into the actinide series, work began on comparisons between Am and other actinides and lanthanide species. In a paper published in 1951, the first study of the absorption spectrum of Am(III) showed similarities to rare earth solutions [40-42]. The absorption spectrum of Am(III) showed an intense absorption at 503 nm in perchloric acid. The pentavalent state of Am (AmO_2^+) was studied by Werner and Perlman [38] by oxidizing an Am(III) carbonate solution with sodium hypochlorite. The hexavalent state of Am was reported by Asprey, Stephanou, and Penneman in 1951 [34]. They studied the oxidation of Am(III) using ^{243}Am and three different routes; ammonium peroxydisulfate, argentic oxide and electrochemical oxidation. Of the three routes tried, only the ammonium peroxydisulfate produced any

measurable amounts of oxidized Am. The trivalent state of Am has a characteristic pink color which, when oxidized, changes to a yellow color and finally to reddish-brown. The identification of Am(VI) was done by synthesis of a sodium americyl acetate crystal that showed a refractive index similar to the known uranyl, plutonyl, and neptunyl sodium acetate crystals. Figure 6 shows the spectral differences between Am(III), Am(V), and Am(VI) oxidation states of Am in perchloric solution.

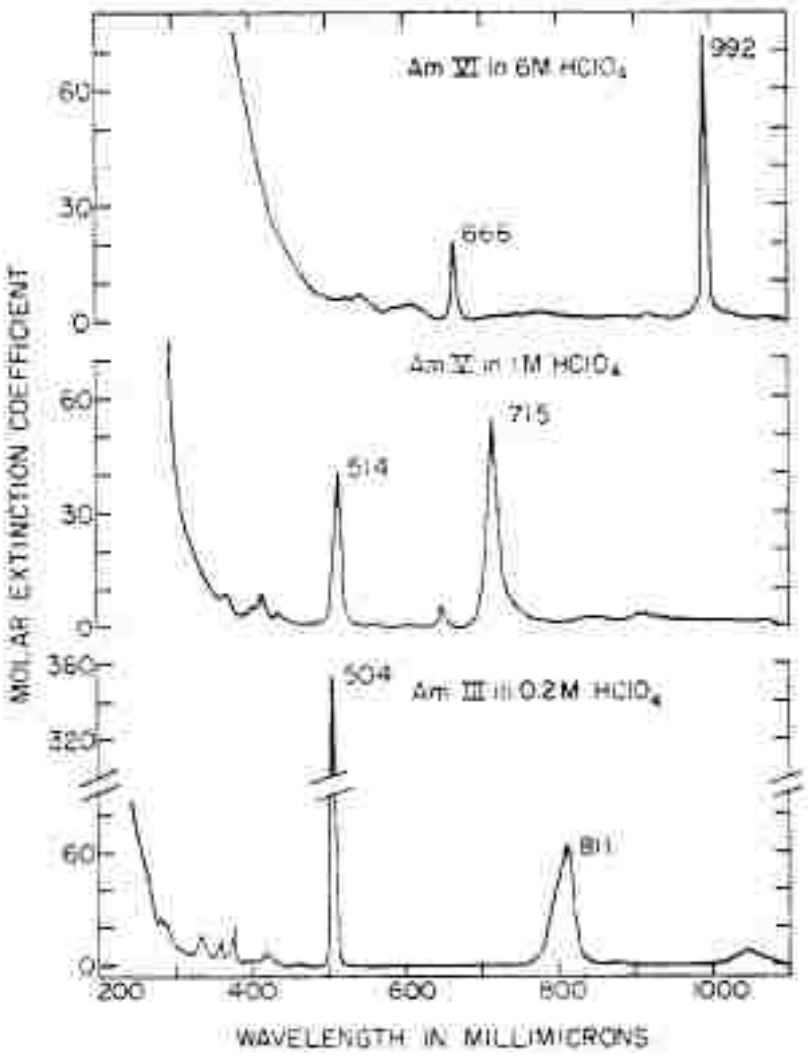

Figure 6 Absorption spectra of the Am(III), Am(V) and Am(V1) ions in $HC1O_4$ [43].

Asprey et al. found stability issues with the higher oxidation states of Am(V) and Am(VI) in acidic solution, however, details of the specific issues were not discussed. Later work was able to shed more light on the stability problems and it was found that the kinetics of the disproportionation of Am(V) to Am(III) and Am(VI) followed by auto reduction of Am(VI) to Am(V) were due to products of radiolysis [38]. The tetravalent Am oxidation state is unstable in acidic media but in strongly basic carbonate solutions Am(IV) is stable. In fact, in carbonate solutions, Am has been shown to be the second element, after Pu, to coexistence in all four oxidation states simultaneously [44]. In carbonate solutions, Am(VI) can oxidize Am(III) by means of the equilibrium in equation 2-1:

$$\text{Am (III)} + \text{Am (VI)} \leftrightarrow \text{Am (IV)} + \text{Am (V)} \qquad \text{(Eq. 2-1)}$$

Despite the stability problems associated with higher oxidation states, a large number of methods have been developed for the separation of Am and Cm by oxidizing Am [45-47]. The increased stability of the upper oxidation states of Am could prove invaluable in developing a procedure for the selective removal of Am from Cm and the lanthanides. Complexing ligands such as OH^-, or CO_3^{2-} can form strong complexes with the actinides in the order $An^{4+} > AnO_2^{2+} \geq An^{3+} > AnO_2^{+}$ [44]. Americium (VI) was quantitatively produced in 0.1 M $NaHCO_3$ containing a suspension of $Am(OH)_3$ when 5% ozone was passed through for one hour. Am(VI) has been produced in aqueous 2 M carbonate solutions as well through the oxidation of Am(III), Am(IV), or Am(V) with ozone giving an intensely red-brown Am(VI) carbonate complex [46, 48, 49].

In other methods, the separation of Am and Cm by oxidizing Am to the hexavalent state with peroxydisulfate followed by a precipitation of CmF_3 has been reported by Stephanou et al. [50]. Separation of Am(VI) from large quantities of the lanthanides has also been shown through precipitation of the lanthanide triflourides [51]. Although fluoride precipitations are capable of achieving > 90% separation they employ 3 - 4 M HF as the precipitating agent making the process less than desirable for commercial reprocessing or recycling due to difficulty in handling and the corrosive nature of fluoride solutions.

Over time, a variety of new separation methods were reported that employed oxidation of species to higher states. One of these methods, liquid-liquid extraction, used ammonium persulfate as an oxidizing agent to oxidize Am(III) to Am(VI) followed by reduction that produced Am(V) [52]. Other oxidizing agents used for the separation of trivalent actinides include: potassium persulfate [53] , sodium perxenate [54], sodium bismuthate [10], and electrolytic oxidation [55, 56]. There are inherent disadvantages to using the persulfates, perxenates and electrolytic oxidization routes [54, 57]. Therefore, one current focus for the oxidation of Am is centered around sodium bismuthate ($NaBiO_3$) [10-12]. Sodium bismuthate, with a structure shown in Figure 7, is commonly used in the determination of manganese.

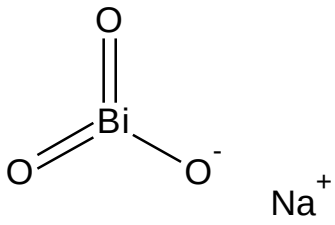

Figure 7 Structure of the sodium bismuthate oxidizing agent.

This method is known to be interfered by the presence of cobalt (Co) and cerium (Ce) because they are oxidized to Co(III) and Ce(IV) by sodium bismuthate, respectively. Therefore, the standard potential for the Bi(III) – Bi(V) are enough to oxidize Am(III) – Am(VI) using Bi(V), since the potentials for Co(II) – Co(III) and the Ce(III) – Ce(IV) are 1.95 volts and 1.74 volts, respectively [58]. The standard reduction potential for Am oxidation states, shown in Figure 8, when compared to those of the Bi(III) – Bi(V) at 2.03V, verifies the sodium bismuthate will sufficiently oxidize Am(III) to Am(VI).

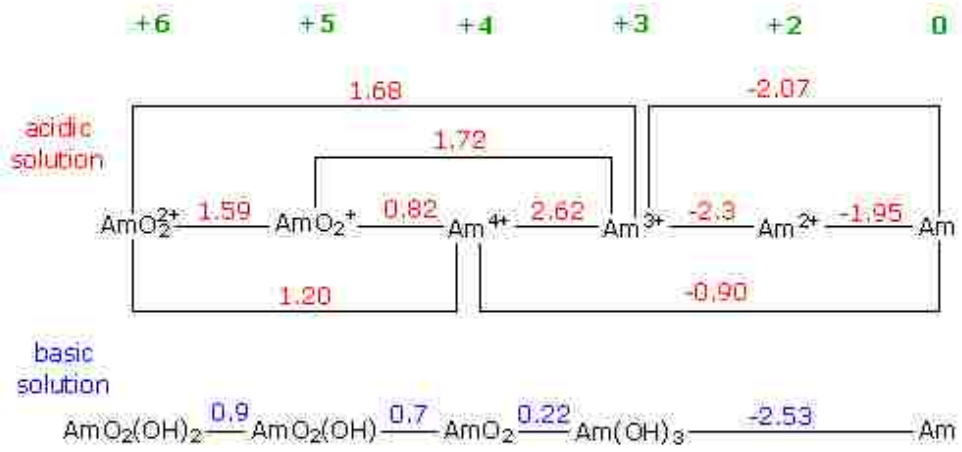

Figure 8 Standard reduction potentials of Am (Eo/V)

Even though sodium bismuthate is marginally soluble in HNO_3, it can be supersaturated to reasonable amounts with the remainder of the solid $NaBiO_3$ easily removed from solution prior to use in a separation process. The sodium bismuthate offers an oxidation route for Am that has very few disadvantages when compared to other oxidizing agents such as persulfate and ozone and for this reason it is the sole oxidizing agent used in this project. Some of the advantages of using sodium bismuthate are [10, 12, 59]:

- Am(V) can be prepared directly in acidic solution.
- Acts as a holding agent for Am(VI).
- Both Am(V) and Am(VI) are present in appreciable quantities over long periods of time.

Some of the disadvantages associated with sodium bismuthate are [10, 11, 12]:

- Low solubility in HNO_3, approximately 10% by volume.
- The need for excess solid present for complete oxidation.
- Slow oxidation kinetics on the order of hours.

2.2 Density Functional Theory

Density functional theory (DFT) is presently among the most successful methods to compute the electronic structure of matter, both in terms of accuracy and efficiency [60]. Its applicability ranges from atoms and molecules to solids, in a variety of chemical environments. A wealth of molecular properties can be derived from DFT calculations, including molecular structures, vibrational frequencies, atomization energies, ionization energies, electric and magnetic properties, and reaction paths [61, 62]. Nowadays most electronic structure calculations for solids and extended molecular systems are based on

DFT, which was formulated over four decades ago and has numerous theoretical extensions since then and quantum chemistry for solving the many body quantum mechanical problems [63]. The objective of this project is to use these methods to develop an atomic picture of Am in higher oxidation states in aqueous solution and use the data to better understand real reaction processes. Ultimately, if this work is a success it will result in an experimental data based model to be used in the separation of species with very similar chemical properties.

The cornerstones of DFT are the Hohenberg–Kohn theorem [62, 64] and the Kohn–Sham kinetic energy functional [64]. The Hohenberg–Kohn theorem establishes that for electrons moving in an external potential v(**r**), different potentials give rise to different ground-state electron densities, such that the external potential is a functional of the electron density. Since the knowledge of the ground state density then also uniquely determines - *via* the external potential - the Hamiltonian of the system, the ground state energy and other properties (including those of excited states) are a *functional* of the electron density $\tilde{n}(\mathbf{r})$. A functional is defined as a function of a function. A variational principle holds for the energy functional, such that the exact ground state density, is obtained by minimizing the energy functional $E[\tilde{n}]$. Density functional theory becomes a computational method through the introduction of *approximate* energy functionals for which one is able to find the density which minimizes this functional. This contrasts with wave function based methods where one strives for approximate solutions to the exact Hamiltonian [62, 64].

The breakthrough came with the suggestion by Kohn and Sham of an implicit functional for the kinetic energy which is the kinetic energy T_S of a fictitious system of non-interacting electrons having the same density, equation 2-2:

$$E[\rho] = T_s[\rho] + \int v(r)\rho(\mathrm{r})d\mathrm{r} + \tfrac{1}{2}\iint \frac{\rho(\mathrm{r}_1)\,\rho(\mathrm{r}_2)}{|\mathrm{r}_1 - \mathrm{r}_2|}\, d\mathrm{r}_1 d\mathrm{r}_2 + E_{\mathrm{xc}}[\rho] \qquad \text{(Eq. 2-2)}$$

where the third term is the Hartree term describing the electron-electron Coulomb repulsion, and $E_{\mathrm{xc}}[\rho]$ is the exchange-correlation functional which needs to be approximated as accurately as possible while keeping a form that makes the determination of the minimizing density computationally tractable.

The simplest approximate exchange-correlation functional is the *local density approximation* (LDA), equation 2-3:

$$E_{xc}[\rho] = \int \rho(\mathrm{r})\epsilon_{xc}(\rho(\mathrm{r}))d\mathrm{r} \qquad \text{(Eq. 2-3)}$$

where ε_{xc} is the exchange-correlation energy per electron of a homogeneous electron gas with constant density $\tilde{n}$. Although the resulting method is exact only for a homogeneous electron gas, it also gives generally good results for atomic and molecular systems despite their electron density being strongly inhomogeneous.

In an attempt to improve upon LDA, an additional requirement is that E_{xc} be exact for an inhomogeneous electron gas with a varying density, with the following functional form, equation 2-4, which involves a two-parameter function F_{xc} that depends on the density as well as its gradient.

$$E_{xc}[\rho] = \int F_{xc}(\rho(\mathrm{r}), |\nabla\rho(\mathrm{r})|)d\mathrm{r} \qquad \text{(Eq. 2-4)}$$

This so called GGA was pioneered by Langreth and Mehl [64] in the 1980's and from then on, a large number of different GGAs have been proposed, unlike the LDA which possesses only a 2 variants. More recently, extensions have been introduced, i.e. the so-called *hybrid* functionals, that use part of the Hartree–Fock exchange energy [62] or add the kinetic energy density as an additional variable in order to improve the accuracy of selected molecular properties.

In addition, spin density functional theories, in which the spin-up and spin-down densities are treated as two independent variables, have also been developed for open shell systems which require LDA and GGA (and *hybrids*) that depend on the spin-up and spin-down densities as well as their gradients. For systems containing elements Z > 36, relativistic effects have also been introduced as an extension of standard DFT methods, since the Schroedinger equation does not give the correct answer because its classical limit is nonrelativistic mechanics.

2.3 Experimental Facilities

Americium oxidation

For the experiments of interest in this work, ^{234}Am samples were prepared at the Radiochemistry Laboratory (RCL) at the Idaho National Laboratory (INL). Preparation of the liquid samples was carried out in the RCL's macro radioisotope lab as were the ^{243}Am, ^{238}U crystal synthesis experiments.

XAFS Experiments

Once the liquid samples had been prepared, they were shipped to the synchrotron beam at either the Advanced Photon Source at Argonne National Laboratory (APS, ANL) or the Stanford Synchrotron Radiation Lightsource (SSRL) to conduct XAFS experiments on the oxidized (AmO_2^+, AmO_2^{2+}) solutions. Within the APS, there are 5 main components that make up the technical facility: the linear accelerator, the booster synchrotron, the electron storage ring, insertion devices, and the experiment hall shown in Figure 9 [65]. The APS synchrotron is an electron beam that accelerates electrons to 450 MeV. The electrons are relativistic, traveling at >99.999% of the speed of light, which is 299,792,458 meters/second. Electrons are injected into the booster synchrotron and accelerated from 450 MeV to 7 GeV in one-half second. The high speed electrons are injected into a storage ring for use in a variety of research projects. The sequencing of magnets in the APS storage ring produces a beam of very small size and low angular divergence, qualities prized by users of synchrotron light sources. The sequenced magnets, or lattice, results in 40 straight sections, or sectors, in the storage ring of which 35 can be used for a variety of instrumentation including the XAFS instrument used for this work. The XAFS was performed at The Basic Energy Sciences Synchrotron Radiation Center (BESSRC) Collaborative Access Team (CAT) (BESSRC-CAT 11 BM) [65].

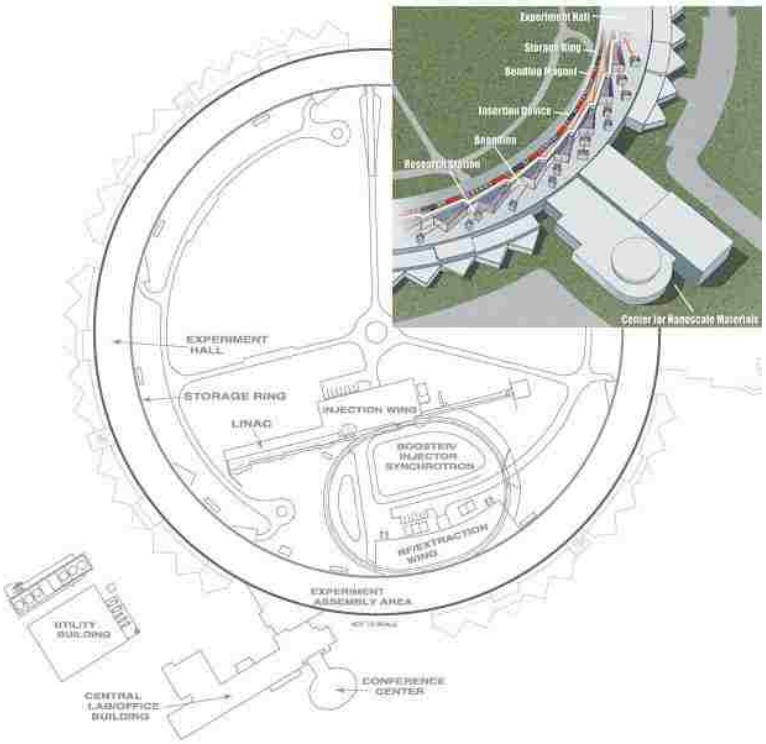

Figure 9 Schematic of the APS XAFS synchrotron, storage ring and experiment hall [65].

The SSRL, a directorate of the SLAC National Accelerator Laboratory, is an Office of Science User Facility operated for the U.S. Department of Energy by Stanford University. The SSRL facility has a similar synchrotron set up to APS, but at a lower energy, and produces extremely bright x-rays and supports numerous experimental setups including the XAFS analysis for this work. The SSRL facility utilizes x-rays produced by its accelerator, the Stanford Positron Electron Asymmetric Ring (SPEAR3). There are 26 experimental stations (hutches) on 10 main beam lines. SPEAR3 consists of a single ring some 80 meters in diameter, in which counter-rotating beams of electrons and positrons were circulated at energies up to 3 GeV. The SPEAR3 is filled with bunches of electrons and positrons traveling in opposite directions around the ring. The particles

circulate in an evacuated pipe. Dipole magnets placed at regular intervals provide the force to steer the particles around the ring. The particles are fed to SPEAR3 at the desired energy from an accelerator, originally the two mile SLAC LINAC. As the charged particles circulate they lose energy as synchrotron radiation. This electron energy is restored each time they pass through the accelerating cavity that is part of the ring. The electric fields in this cavity provide the force to reaccelerate electron bunches.

The SPEAR3 is used exclusively for synchrotron radiation physics at SSRL, with only a single beam of stored electrons. SSRL now has its own particle accelerator to feed it electron beams, so it can operate independently of the linac for a wide variety of synchrotron-radiation-based studies. XAFS experiments at SSRL covered in this work were performed at beam line 11-2 which has a focused energy range of 4.5 – 21.0 MeV, resolution ($\Delta E/E$) of $1x10^{-4}$, and a spot size (aperture) 0.5 x 3.0 mm. Beam Line 11-2 is a high-flux XAS station equipped with collimating and focusing optics, a "double double" Si(220) liquid nitrogen (LN_2)-cooled monochromator, grazing incidence XAS spectrometer, and HEPA-filtered controlled exhaust systems which continuously monitor for the presence of air-born radioactivity. It has an adjacent sample preparation room for handling and temporary storage of radioactive samples.

CHAPTER 3

LITERATURE REVIEW

This chapter provides a background on Am and Cm followed by a literature review on the separation methods. Also included in this chapter is a literature review of the separation processes under development for the separation of Am in its higher oxidation states for use in aqueous used nuclear fuel reprocessing or recycling.

3.1 Americium and Curium History

History

Am, element 95, was named after the Americas and is the sixth member of the actinide series, analogous to europium, Eu, of the lanthanide series [66]. Cm, element 96, is named after Pierre and Marie Curie, by analogy with its lanthanide congener, gadolinium (named after the Finnish chemist, J. Gadolin). Americium and Cm were first discovered in November of 1945 by Seaborg and Hamilton by bombardment using 40 MeV helium (He) ions on a ^{238}U target at the 60" cyclotron at the Radiation Laboratory of the University of California, Berkeley [67]:

$$^{238}U\ (\alpha,n)\ ^{241}Pu \xrightarrow{\beta^-} {}^{241}Am$$

$$^{239}Pu\ (\alpha,n) \longrightarrow {}^{242}Cm$$

The analysis of Am and Cm chemical and radioactive properties was performed at the Metallurgical Laboratory of the University of Chicago. After Seaborg's discovery of the actinides Am and Cm, it was necessary to find a way to chemically separate them from

the ^{239}Pu target that was used in their production [67]. Seaborg and Ghiorso established the first clear-cut evidence that the actinide series exists verifying Seaborg's theory that a new 5*f* element rare earth series would follow actinium (Ac) in the same way that the 4*f* lanthanides follows lanthanum (La) on the periodic table [66]. It was believed that Am and Cm should behave in similar fashion to the previous actinides and would oxidize to a +6 state the same as PuO_2^{2+}. Unfortunately, this was not the case and the chemistry needed for the separation of Am and Cm from the target would have to be changed. For this new chemical separation scheme, Seaborg took into consideration how other elements behaved on the periodic table such as cesium (Cs) and barium (Ba) which showed the same type of chemistry as francium (Fr) and radium (Ra). Figure 10 shows the new actinide series as Seaborg postulated it would look starting from actinium where the 5*f* shell electrons were to be populated [67].

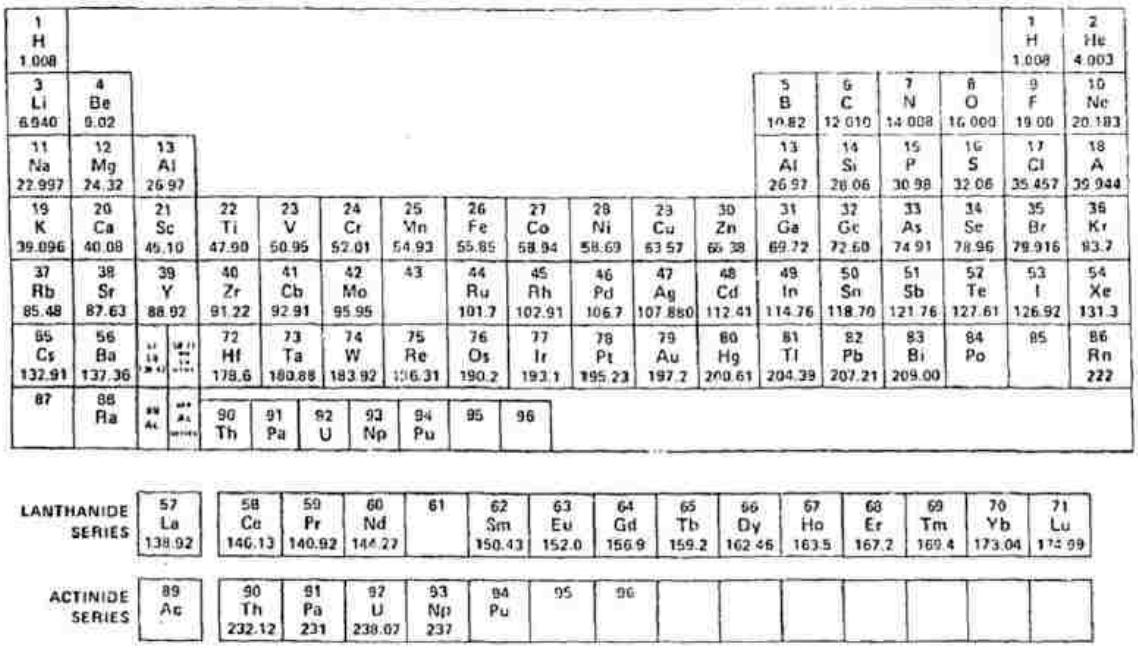

Figure 10 Periodic table arrangement according to Glenn T. Seaborg with heavy elements shown both as a new series, actinide, under the lanthanide series and as part of the main periodic table under the transition metals [67].

In the mid 1940s, more detailed information regarding the production of several isotopes of Am (238, 239, 241, 242) was provided in reports to the Atomic Energy Commission [68]. After that initial report, a paper was also published that included details on the preparation of both Am and Cm isotopes [68]. The report outlined alternative routes for production of ^{241}Am and ^{242}Cm that are still used today and offer the best method for the production of pure ^{241}Am.

$$^{239}\text{Pu}(n,\gamma)\,^{240}\text{Pu}(n,\gamma)\,^{241}\text{Pu} \xrightarrow{\beta^-} {}^{241}\text{Am}$$

$$^{241}\text{Am}(n,\gamma)\,^{242}\text{Am} \xrightarrow{\beta^-} {}^{242}\text{Cm}$$

Americium plays an important role in the actinide series; it lies directly below Eu in the periodic table, has nominally six 5*f* electrons, appears to be the first element in which the 5*f* electrons are localized, and is the last of the light actinides [68]. Currently, 20 isotopes of are known according to the National Nuclear Data Center with mass number 230-249 and half-lives ranging from ~17 seconds to 7370 years [69]. A great deal is known about Am with mass numbers 232, 234, and 237-247, however, much less is known about the neutron-deficient Am isotopes such as ^{233}Am, ^{235}Am, and ^{236}Am. The light isotopes up to ^{243}Am mainly decay by electron capture (EC), emission of alpha (α) particles, and spontaneous fission (SF). The isotopes beyond ^{243}Am are short-lived beta (β^-) emitters and ^{243}Am decays primarily by α (99.9+%) and very rare SF [68].

Due to their long half-lives, ^{241}Am ($t_{½}$ = 433 years) and ^{243}Am ($t_{½}$ = 7,370 years) are the most important of the Am isotopes and make up approximately 66% and 48% of the Am in used nuclear fuel, respectively. Production of ^{243}Am from ^{242}Pu is shown below.

$$^{242}\text{Pu}(n,\gamma)\ ^{243}\text{Pu} \xrightarrow[5\text{h}]{\beta^-}\ ^{243}\text{Am}$$

Commercial nuclear power reactors produce kilogram quantities of both ^{241}Am and ^{243}Am with the isotopic composition dependent on the reactor burn-up [70, 71]. Approximately 30 kg of Am are reported to be stored at US DOE Hanford waste site alone, storage will ultimately become limited and development of new and improved technologies for the separation of Am from Cm in nuclear fuel reprocessing or recycling will be needed [72]. It is possible that both Am and Cm could be added to a U/Pu MOX fuel before it is loaded into a fast reactor as one means of transmutation. However,

working with Cm is much more challenging than working with Am because Cm is a neutron emitter and the MOX production line would need to be shielded with both lead and water to protect the workers, or the fuel fabrication would need to be done remotely, at a substantial increase in cost.

The neutron irradiation of Cm generates the higher actinides, such as californium, which increases the neutron dose associated with the used nuclear fuel; this has the potential to pollute the fuel cycle with strong neutron emitters. As a result of the increased dose and associated facility cost, it is likely that Cm will be excluded from MOX fuels. Most of the standard methods, aqueous and non-aqueous, for separating and purifying Am from all kinds of sources and materials were developed in the 1950s, 1960s, and 1970s [73]. In contrast to earlier time periods, the research development of the 1980s, 1990s, and today focused on new or improved solvent extraction process technology for recovery and/or purification of Am [74].

As trivalent ions, Am and Cm are similar to each other as well as to the trivalent lanthanides (Ln) and they exhibit essentially the same behavior toward group reagents. The stable trivalent state of Cm in aqueous solution can be helpful in separations since it behaves in similar fashion to the lanthanides. However, if one must purify Cm from another exclusively trivalent "lanthanide-like" impurity, it can become very difficult [75]. Seaborg predicted that increased stability of the +3 states for the 5*f* series would become very stable around Am and Cm, similar to the chemical behavior observed in the lanthanides. Seaborg also showed that Cm should only exhibit the +3 oxidation state in solution given its half-filled *f* orbital, from $[Rn]5f^{7}6d^{7}s^{2}$ to $[Rn]5f^{7}$ [76, 77]. The separation of Am and Cm from each other, other actinides, and trivalent lanthanides have

been explored since their discovery. Both Am and Cm trivalent oxidation states in solution are very close in size with ionic radii of 0.975 Å and 0.97 Å, respectively [78]. The similarities in ionic size, common oxidation state, solubility, and complexation with other elements pose difficulties in the development of efficient separation methods for these trivalent actinides. However, Am can be oxidized to multiple higher oxidation states where as Cm only oxidizes to +4, making Am an excellent candidate for oxidation separations.

In aqueous solutions, Am can exhibit the +3, +4, +5, and +6 oxidation states. All four oxidation states can coexist under certain conditions in carbonate media. In dilute acid, only the aquo ions Am^{+3} and AmO_2^{+2} ions are stable, however, in alkaline solutions Am can exist in all four valance states. The highly charged ions in the +5 and +6 oxidation states are unstable and hydrolyze rapidly to form the linear trans-dioxo americyl cations, AmO_2^{+} and AmO_2^{2+}, respectively [79]. Similar to Np(VII) and Pu(VII), Am reportedly can be oxidized to Am(VII) in highly alkaline media, but this state is unstable and reduces to Am(VI) rapidly [80]. The pentavalent state of Am can undergo self-reduction with a zero-order rate in perchloric acid corresponding to ~2% per hour. The rate is somewhat variable in different media. However, it must be emphasized that this rate applies only to ^{241}Am with a half-life of 432 years and a specific activity of 7.12E8 decays/min/mg. The emitted alpha particles interact with the solution to produce radicals, the net effect of which reduces Am(VI) to Am(V) and Am(III). The rate of production of these radiolysis products is proportional to the total amount of alpha emitters and determines the rate of self-reduction. Thus, pentavalent Am containing the

longer lived ^{243}Am ($t_{½}$ = 7370 years), will undergo considerably slower self-reduction [81].

3.2 Higher Oxidation State Separations

Separation Methods Based on Different Oxidation States

Oxidation-reduction cycles for the separation of Am from Cm have shown the best promise and are used in solutions in which the Am is oxidized to the (V) or (VI) state, with Cm remaining trivalent throughout. A clean separation of Am from Cm is necessary for the removal of isobaric interferences in Cm analysis, and a good separation of Am from trivalent fission product lanthanides would greatly simplify current designs for nuclear fuel cycle closure. Of the four Am higher oxidation states, two are currently being used for separations development, however, few options for their production in acidic media have been tested [44]. Separation techniques employing differences in oxidation states are extremely common among many elements in the periodic table and are used in large and small scale chemical processes [82]. Using different oxidation states allows for simple and quick partitioning due to distinct variations in chemical behavior.

After the discovery of Am, and its addition to the actinide series, analogies with Eu, were realized. On the periodic table, Am lies just below Eu and it shares many similarities in chemical and physical properties to this lanthanide (see section 2.1). Issues related to the instability of the higher oxidation states of Am in acidic solution were reported by Asprey et al. [38]. Later studies by Stover et al. showed in greater detail the kinetics of the disproportionation of Am(V) to Am(III) and Am(VI) followed by auto

reduction of Am(VI) to Am(V) due to products of radiolysis [43]. The tetravalent Am oxidation state (IV) was reported in sodium carbonate-sodium bicarbonate medium along with Am(III), Am(V), and Am (VI) [38]. However, a very limited number of experiments have been reported in the literature for Am(IV) in solution, mostly due to the unstable state of tetravalent Am. Despite issues regarding the stability of higher oxidation states, a large number of methods have been developed for the separation of Am and Cm using oxidized Am. Separations employing the oxidation of Am prefer the Am(VI) over Am(IV) or Am(V), however, recent work has been looking more closely at the Am(V) oxidation state as being more stable than originally thought [34]. Many separation schemes have been developed over the past 73 years since the discovery of Am and Cm and some are still used today.

For the partitioning of actinides, there are a multitude of separation methods that have been proposed. Currently, the major separation areas for minor actinides and lanthanides include pyroprocessing [83], electrorefining [44, 84], advanced solvent extraction [59, 85], and ion exchange chromatography [72]. For the purpose of this project, separation work related to the oxidation of the minor actinides, specifically Am and Cm, were investigated.

In the mid 1960s, oxidation of Am for its separation from Cm was established using ozone, a very strong oxidizing agent, followed by precipitation using K_2CO_3[55, 86]. A method used under basic conditions employs ozone oxidation of $Am(CO_3)OH_{(s)}$ solubilizes Am from a lanthanide carbonate hydroxide solid phase to the aqueous phase as the $AmO_2(CO_3)_3^{4-}$ or $AmO_2(CO_3)_3^{5-}$ species. Complexing ligands such as OH^- or

CO_3^{2-} have been used in the past to form strong complexes with the actinides in the order $An^{4+} > AnO_2^{2+} \geq An^{3+} > AnO_2^{+}$ [87, 88].

Other separations reported include column chromatography extractions that use solubility differences to separate oxidized Am(VI) from Cm(III) by eluting Am(VI) from a calcium fluoride loaded column [89, 90]. Both ion exchange chromatography and liquid-liquid extraction methods were also established for Am(V) or Am(VI) separation from Cm(III) with the use of ammonium peroxydisulfate as an oxidizing agent [91]. Currently, a promising oxidizing agent continues to be investigated for maintaining Am in stable oxidation states. Sodium bismuthate was investigated by Hara and Suzuki [51] for the oxidation of Am(III) to Am(VI) and Am(V). Sodium bismuthate has previously been used for the determination of manganese (Mg). The low solubility of this reagent in HNO_3 solution could be an advantage because the reagent is only slightly soluble and can be easily removed from the reaction system. The amount of bismuthate dissolved in the solution can oxidize only a small amount of materials [92, 93]. Hara et al. discovered sodium bismuthate can be made more soluble by increasing the HNO_3 concentration as well as increasing the temperature and this information was used to determine optimal acid/bismuthate concentrations in Chapter 5.1 [11].

However, the concentration of Bi(III), which was equal to the difference between the concentrations of total bismuth and Bi(V), increased rapidly with the time of mixing at 30^{o} C especially at higher acidities, while it remained at lower levels at 0^{o} C as shown in Figure 11.

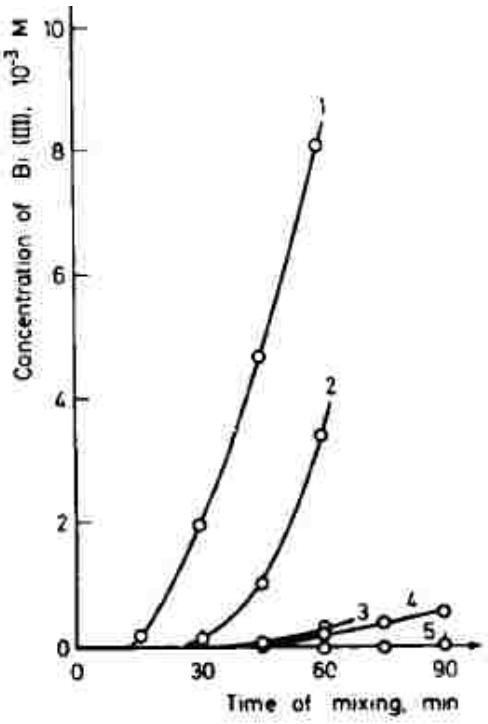

Figure 11 The concentration of Bi(III) in HNO_3 solution mixed with sodium bismuthate at the acidity of 4 M (curve 1), 2 M (curve 2), and 1 M (curve 3) at 30^o C and at the acidity of 4 M (curve 4) and 2 M (curve 5) at 0^o C [94].

Regardless of the oxidation method, Am(V) and Am(VI) eventually reduce to Am(III) and early work by Coleman et al. [83] showed radiolytic reduction at 4 %/hour as well as reduction by water from radiolysis products such as hydrogen peroxide. Most of the work done by Coleman et al. was in carbonate solution and lower stability issues were reported for acidic systems that showed around 1% per hour reduction rate in HNO_3 solution with sodium bismuthate as the oxidizing agent [10-12]. Throughout the years of testing with a variety of oxidizing agents one constant has held true, Am(V) and Am(VI) act as powerful oxidants and will reduce to Am(III) in the presence of higher acidic solution and/or organic extractants making new solvent extraction processes employing oxidizing agents a challenge to design.

CHAPTER 4

ANALYTICAL METHODS

Various analytical techniques have been utilized in the investigation of Am higher oxidation states. These include XAFS, UV Visible Spectroscopy (UV-Visible), Single Crystal X-ray Diffraction Spectroscopy, Scanning Electron Microscopy, and HPGe Gamma Spectroscopy. Information regarding each technique is presented in this chapter including: theory of operation, system specification, general procedure for sample preparation and measurement, and final data analysis.

4.1 X-ray Atomic Fine Structure (XAFS)

Synchrotron-based X-ray absorption fine structure spectroscopy is an important tool for a multitude of scientific research providing unique structural and composition information for solid, liquid, and gas sample compositions in either dilute or concentrated form. XAFS is an element-specific, bulk-sensitive, and nondestructive method for analysis of complex components. A potential drawback when using XAFS for the analysis of higher oxidation states in solutions is stability of the oxidation state during beam contact time. This is generally less of a problem with solid samples; however, solids are difficult to produce in higher oxidation states outside of certain crystal forms.

Theory of Operation

The intensities of XAFS spectra of metal ions are dependent on the concentration of metal ions on solid particles or in solution. If the concentration is low, the XAFS spectra of the metal ions generally have very high noise and cannot be used to get local

atomic structure information. X-rays are absorbed by matter primarily through the photoelectric effect, whereby at energies above the ionization threshold electrons from inner core states are excited into empty outer-lying states. Related edge energies for select actinides, Table 3, show a steady increase in energy with increasing Z. The XAFS spectra are obtained by measuring the X-ray absorption or fluorescence of a given sample as a function of the wavelength [95].

Table 3 X-ray K- and L-edge energies of select actinide elements in eV [95].

Z	Element	E(K)	$E(L_I)$	$E(L_{II})$	$E(L_{III})$
92	U	115606.1	21757.4	20947.6	17166.3
93	Np	118678.0	22426.8	21600.5	17610.0
94	Pu	121818.0	23097.2	22266.2	18056.8
95	Am	125027.0	23772.9	22944.0	18504.1
96	Cm	128200.0	24460.0	23779.0	18930.0

X-ray Absorption Fine Structure spectroscopy is a unique tool for studying, at the atomic and molecular scale, the local structure around selected elements that are contained within a material. X-ray Absorption Fine Structure can be applied not only to crystals, but also to materials that possess little or no long-range translational order: amorphous systems, glasses, quasicrystals, disordered films, membranes, solutions, liquids, metalloproteins – even molecular gases [96]. Because of the versatility of XAFS,

it can be used in a wide range of scientific disciplines from chemistry and physics to engineering and materials science.

The basic physical quantity that is measured in XAFS is the X-ray absorption coefficient $\mu(E)$, which describes how strongly X-rays are absorbed as a function of X-ray energy E. Generally $\mu(E)$ smoothly decreases as the energy increases (approximately as $1/E3$), i.e. the X-rays become more penetrating [97]. However, at specific energies that are characteristic of the atoms in the material, there are sudden increases called X-ray absorption edges. These occur when the X-ray photon has sufficient energy to liberate electrons from the low-energy bound states in the atoms. Absorption edges were first measured in 1913 by Maurice De Broglie, the older brother of quantum mechanics pioneer Louis De Broglie [98].

In 1920, using M. Siegbahn's vacuum spectrograph, Hugo Fricke first observed the "fine structure" – energy-dependent variations in the $\mu(E)$ – in the vicinity of the X-ray absorption edges of a number of elements. It would take the next fifty years for XAFS to become the significant scientific analysis tool it is today due, in part, to a controversy that existed over whether a model based on the long-range order (LRO) or short-range order (SRO) in the sample was more appropriate [98]. This controversy was cleared up around 1970 when Stern, Sayers, and Lytle demonstrated XAFS could be a practical tool for structure determination [99].

X-ray absorption fine structure is a broad term that encompasses several different techniques: EXAFS (Extended X-ray Absorption Fine Structure); XANES (X-ray Absorption Near Edge Structure); NEXAFS (Near Edge XAFS); and SEXAFS (Surface EXAFS) [100]. Although the basic physics of these techniques is fundamentally the

same, different approximations, techniques, terminology, and theoretical approaches may be employed in different situations, particularly when using low-energy (soft X-ray) and high-energy (hard X-ray) regimes [96]. X-ray Absorption Fine Structure spectroscopy has developed parallel with the growth of synchrotron radiation research. X-ray Absorption Fine Structure requires an X-ray beam of finely tunable energy; although it is possible to do limited experiments with a laboratory X-ray source, most experiments benefit enormously from the availability of synchrotron radiation. As a consequence, nearly all modern XAFS experiments are performed at Synchrotron Radiation Sources (SRSs) [96].

Extended X-ray Absorption Fine Structure

X-ray Absorption Fine Structure is the oscillating part of the X-ray Absorption Spectrum (XAS) that extends to about 1000 eV above an absorption edge of a particular element in a sample. Extended X-ray Absorption Fine Structure is caused when electrons are knocked out of an atom when the energy value of incident X-rays surpasses the ionization threshold (the edge energy). The interference of these outgoing photoelectrons with the scattered waves from atoms surrounding the central atom causes EXAFS in the same way a pebble thrown in a pond creates outgoing waves on the water. The regions of constructive and destructive interference are respectively seen as local maxima and minima giving rise to the oscillations in EXAFS. X-ray Absorption Fine Structure is a direct consequence of the wave nature of the photoelectron. As the photoelectron propagates away from the atom of interest it scatters from neighboring atoms and the interference at the core-hole atom creates oscillations. Figure 12 illustrates this

photoelectric effect, promotion of a core electron to a higher energy state, and a typical absorption spectrum of the K and L absorption edges.

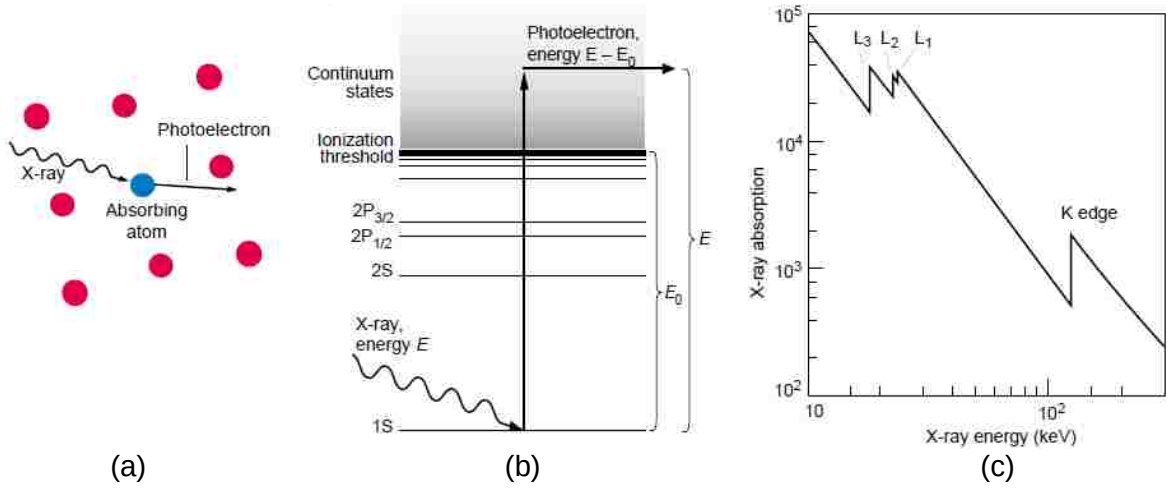

Figure 12 (a) An absorbing atom (blue) is shown surrounded by several other atoms (red). Whenever the energy of an X-ray is greater than the binding energy of one of the absorbing atom's core electrons, the electron is liberated. (b) Schematic of an energy-level diagram of an absorbing atom showing the atom's first few core-electron orbitals: 1S, 2S, $2P_{1/2}$, and $2P_{3/2}$. The ionization potential energy is denoted by E_0. With the absorption of a photon of energy E, the electron undergoes a transition to an unbound state in the continuum and, by conservation of energy, acquires a kinetic energy ($E - E_0$). (c) The peak jumps in this simplified absorption spectrum are the absorption edges, which correspond to the excitation of an electron from a specific orbital. The absorption edge due to excitation of the 1S electron is called the K edge, while excitations from the less strongly bound 2S, $2P_{1/2}$, and $2P_{3/2}$ electrons are called the L_1, L_2, and L_3 edges, respectively [101, 102].

Figure 13 depicts an XAFS spectrum of μ(E) for a platinum foil with the EXAFS and XANES regions identified. In this XAFS spectrum, small oscillations modify the basic absorption coefficient of the free atom μ_o (represented by the dashed line). The small peaks and shoulders that modify the absorption edge and extend about 30 eV

beyond it are the XANES region. The XANES region contains information about the ionization potential and formal oxidation state of a chemical species as well as features that are characteristic of molecular structures. The oscillations that begin approximately 30 eV beyond the absorption edge are the EXAFS region. The EXAFS region contains structural information, such as bond distance, type, and number of neighboring atoms [101].

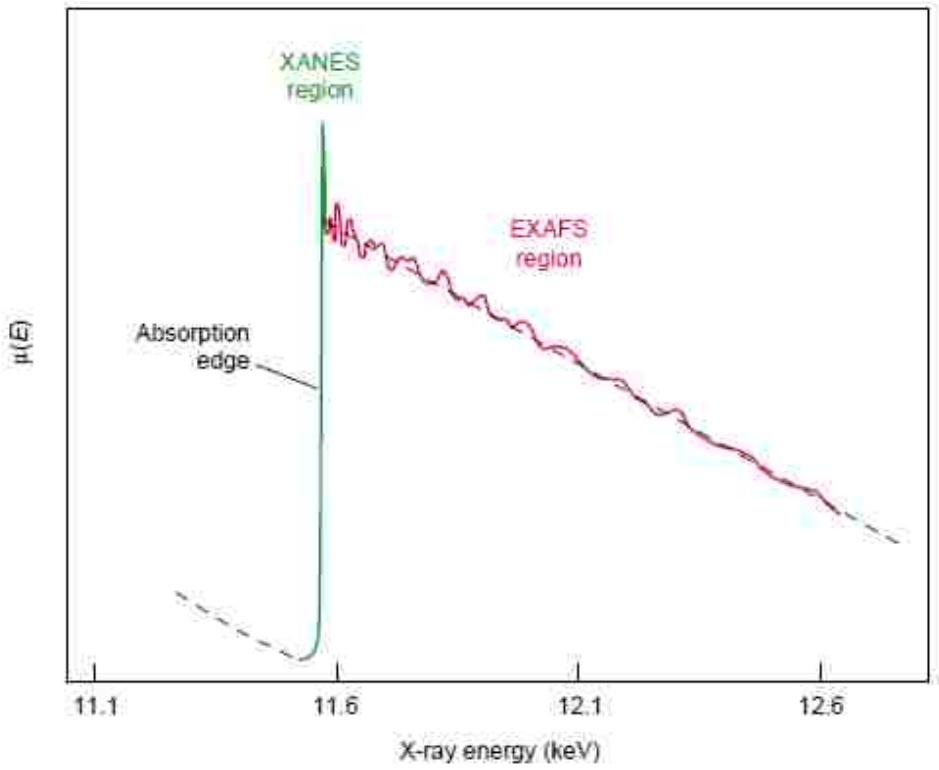

Figure 13 Typical XAFS spectrum showing the EXAFS and XANES region of platinum foil [101].

The main advantage of EXAFS analysis over X-ray Crystallography is that structures can be studied in non-crystalline forms such as liquids. Among other

applications, EXAFS has proven helpful in studying the behavior of non-crystalline materials, environmental samples, and metallo-proteins in their naturally occurring states. The significance of EXAFS lies in the information it gives about [98]:

- Distances between central and neighboring atoms.
- The number of neighboring atoms.
- The nature of neighboring atoms (their approximate atomic number).
- Changes in central-atom coordination with changes in experimental conditions.

The EXAFS equation and term definitions are explained in Equation 4-1 and 4-2 [98, 101, 102].

$$\chi = \sum_{shells} \frac{n_X \cdot S_0^2 \cdot f_X(k) \cdot e^{-2k^2\sigma^2}}{k \cdot r^2} \sin\left(2kr + \alpha_{MX}(k)\right) \qquad \text{(Eq. 4-1)}$$

where f(k) and α(k) are scattering properties of the atoms neighboring the excited atom, n is the number of neighboring atoms, r is the distance to the neighboring atom, S^2_0 is the amplitude reduction, and α^2 is the disorder in the neighbor distance [102]. In the EXAFS equation, if the scattering amplitude f(k) and phase-shift α(k) are known, then it is possible to solve for n, r, and α^2 [101, 102]. Figure 14 shows a typical XAFS set up [101].

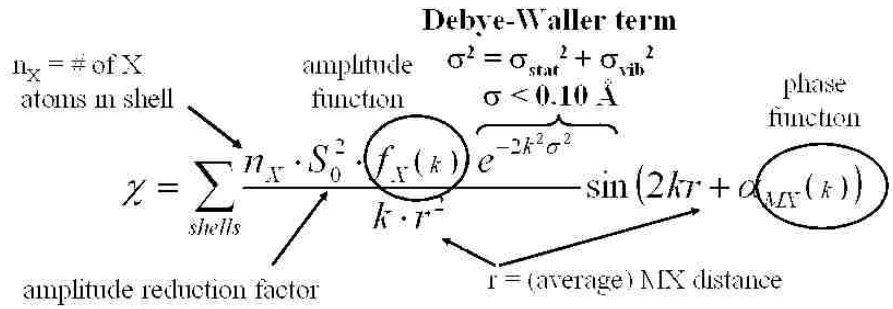

(Eq. 4-2)

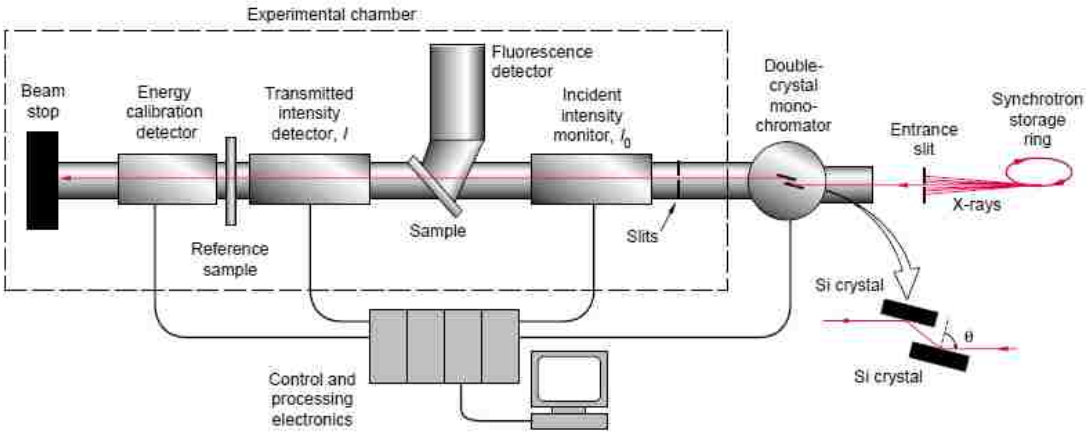

Figure 14 Typical experimental setup for XAFS [101].

The XAFS setup in Figure 14 starts with the full spectrum of x-rays emitted from a synchrotron passing through an entrance slit (which helps collimate the x-rays) before entering a double-crystal monochromator. The x-rays diffract off the crystals' lattice planes, which are aligned at an angle θ with respect to the incoming beam. Because of

the Bragg scattering condition shown in equation 4-3, only x-rays of energy $E_n = nhc/\lambda_i$ can reflect off the crystals.

$$n\lambda_i = 2d\sin\theta \qquad \text{(Eq. 4-3)}$$

Any of several techniques can eliminate the higher harmonics, so that only the fundamental (n = 1) makes it through the exit slits. Different x-ray energies can be selected by changing the angle θ of the crystals. The monochromatic beam passes through an ion chamber that monitors the beam intensity I_0 by absorbing part of it. The beam then passes through the sample, and the intensity of the transmitted x-ray I is measured by a second ion chamber. Taking the log of the ratio of I/I_0 gives the absorption. The sample's absorption can also be determined by measuring the intensity of its x-ray fluorescence with a detector that is out of the beam path. Finally, the beam passes through a reference sample whose absorption edge is used to help correct for uncertainties in the beam's energy [101].

In transmission mode, measurements of the intensity of the incident beam transmitted through the sample are taken. The fluorescence technique involves the measurement of the fluorescence radiation (over some sold angle) at right angle to the incident beam [98]. In transmission or fluorescence mode, EXAFS spectroscopy involves only X-ray measurements [103].

X-ray Absorption Near Edge Structure

The acronym XANES was first used in 1980 during interpretation of multiple scattering resonances in a spectra measured at the Stanford Synchrotron Radiation

Laboratory (SSRL) [102]. The first application of XANES for the determination of distortions in local structural geometry using multiple scattering theory was published on Fe samples [104]. In 1983 the first NEXAFS paper examining molecules absorbed on surfaces appeared. The first XAFS paper, describing the intermediate region between EXAFS and XANES, appeared in 1987 [102].

X-ray Absorption Near edge is an excellent method for examining the local and electronic structures surrounding atoms and has been used in the examination of radioactive materials in nuclear fuel [105]. In particular, XANES gives information on the electronic structures of an unoccupied molecular orbital and gives a unique opportunity to extract the information on the behavior of actinide compounds [105]. In between the pre-edge and the EXAFS regions is the XANES region which arises from effects such as many-body interactions, multiple scatterings, distortion of the excited states wavefunction by the Coulomb field, and band structures [103]. The XANES region begins at approximately 5 eV above the absorption threshold. Because of the low kinetic energy range (5-150 eV) the photoelectron backscattering amplitude by neighbor atoms is very large making multiple scattering events dominant in the XANES spectra. Another important area XANES contributes to is formal oxidation state of the species of interest. Since XANES is sensitive to the chemistry of the absorbing atom, the oxidation state can be determined by a chemical shift owing to electronic transitions.

The different energy range between XANES and EXAFS can also be explained by the comparison between the photoelectron wavelength λ and the interatomic distance of the photoabsorber-backscatter pair. The kinetic energy of the photoelectron is combined with the wavelength λ by the following relationship, Equation 4-4:

$$E_{kinetic} = h\nu - E_{binding} = \hbar^2 k^2/(2m) = (2\pi)^2\hbar^2/(2m\lambda^2) \qquad \text{(Eq. 4-4)}$$

Equation 4-4 shows that the EXAFS region wavelength is smaller than the interatomic distances at higher energy that correspond to a single scattering pattern. For XANES, the lower energy produces a λ which is larger than the interatomic distances and corresponds to multiple scattering.

System Specification

To make these types of measurements in a reasonable time frame synchrotron x-ray source is required in order to provide suitable x-ray intensity. All XAFS measurements were done at the BESSRC-CAT, BM 11 ID-D and Stanford Synchrotron Radiation Lightsource (SSRL) BM 11-2 located at the Advanced Photon Source (APS) in Argonne National Laboratory (ANL) and Stanford University, respectively. Further information on the beamline optics are provided by Beno et al. [106] and Conradson et al [101]. The basic components of a typical XAFS experiment are shown in Figure 15.

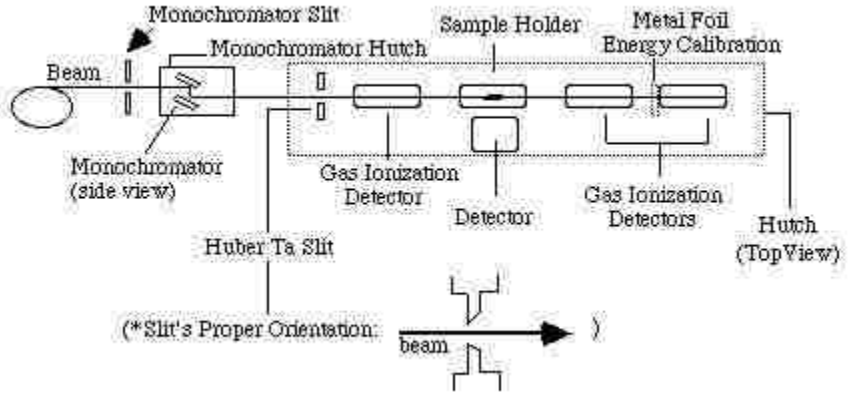

Figure 15 SSRL Hutch set up for XAFS.

X-rays are produced in the source and pass through an aperture before striking the monochromator. The aperture is a pair of slits that can be adjusted in order to control the size and energy resolution of the beam. Most monochromators at SSRL XAFS beam lines are double crystal designs. The first crystal of the pair can be detuned (rotated off of the Bragg condition) for precise alignment and for harmonic rejection [101]. After the beam enters the hutch, it passes through the Huber Ta slits. The beam then passes through the gas ionization chambers where its intensity is measured. The gas ionization chambers are generally used to measure the incident beam and filled with specific gas mixtures for this purpose. Lytle or Germanium detectors are then used to measure fluorescent x-rays from the samples. The hutch setup, including the sample holder for this experiment, is shown in Figure 16 and 17 [107, 108].

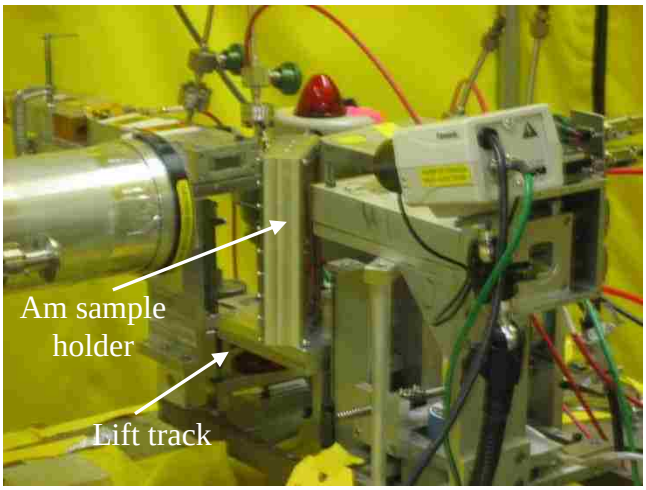

Figure 16 Secondary containment holder with four individual sample holders inside mounted in instrument hutch at SSRL. The holder moves up and down on a track placing each individual sample in the beam path.

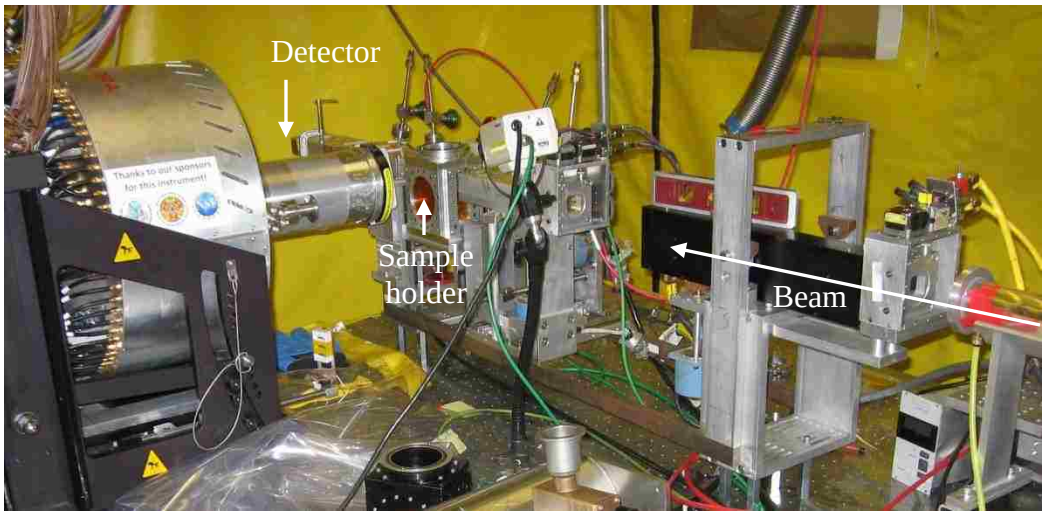

Figure 17 XAFS instrument setup for BM 11-2 at SSRL.

Sample Preparation and Measurement

The concentration of oxidized Am required to obtain sufficient results without self-absorption was approximately 1 mM to 20 mM ^{243}Am. Liquid samples for APS were prepared by loading specially designed sample holders composed of Teflon blocks with a well cut into one side to hold 100 µL of a 1 mM ^{243}Am solution. The holders were first covered by a thin sheet of poly-trifluorochloroethylene (TCFE) and held together between two aluminum plates. From the well, two small openings were cut to provide space for filling. Each filling port was covered by TCFE film and a small piece of rectangular Teflon block with an aluminum cover. The holders were assembled, filled with the 100 µL of oxidized Am sample solutions, sealed and shipped to ANL for the measurements. The samples were aligned, at BESSRC-CAT, BM 11 ID-D, in order to maximize transmittance and fluorescence signals. XAFS spectra were recorded at the L_3 edge (18509 eV) in fluorescence mode at room temperature using a 13 elements

germanium detector. A double crystal Si(220) was used as the monochromator and the energy was calibrated using zirconium foil (Zr-K edge = 17998 eV). The collected spectrum for each sample was an average of ten scans (20 minutes for each scan) and covered 0-14 $Å^{-1}$ in k space.

For SSRL, the concentration of analyte used was 20 mM ^{243}Am. The sample holders were comprised of individual holders of volume 0.5 mL each and loaded into a secondary containment holder containing four samples, maximum of eight samples in the secondary holder are possible (Figure 18).

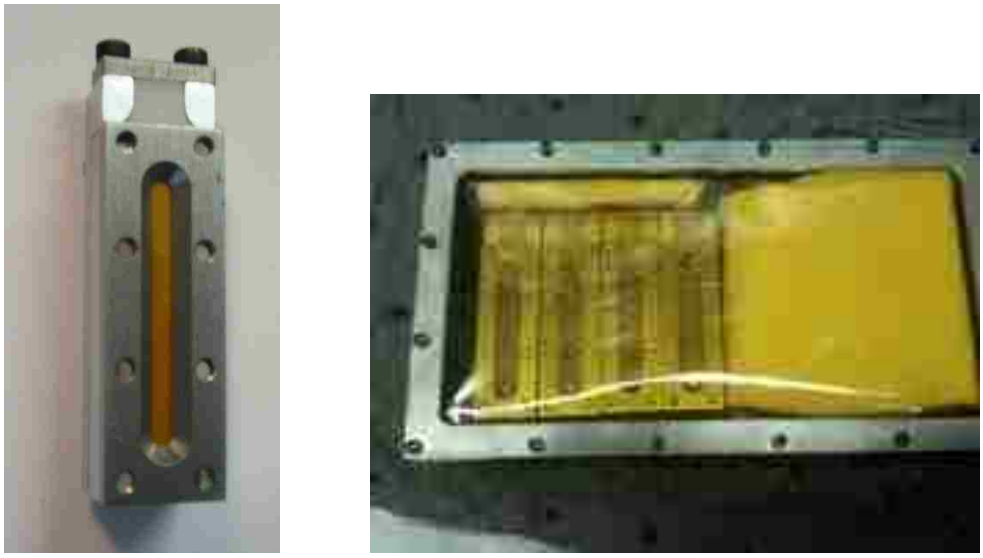

a b

Figure 18 a) SSRL individual holders loaded with ^{243}Am samples and b) secondary containment holder.

The individual sample holders are a Teflon shell with a well that holds 0.5 mL of liquid. A thin Mylar cover, Teflon gasket, and aluminum cover plate covering the front of Teflon holder is bolted into place. The fill hole on the top is covered with a flexible Teflon cap and an aluminum plate is bolted on top of the gasket for a leak proof seal. As shown in Figure 18a, there is a visible window on the sample holder for the beam to contact the sample liquid. There were six samples were loaded with a combination of oxidized ^{243}Am liquid, oxidized ^{243}Am and liquid plus solid oxidizing agent, and non-oxidized ^{243}Am. Two of the loaded sample holders developed a small breach in the seal and were not able to be decontaminated so they were not included in the shipment. The four remaining liquid/liquid solid loaded samples for the SSRL experiment were placed into a secondary containment holder (Figure 18b) and a Mylar window was bolted into place. The samples in the secondary holder were sent to SSRL for measurement.

Data Analysis – EXAFS and XANES

The background corrections were performed with AutoBK which is a program for the analysis of XAFS data [109]. It removes the "background function" from a measured XAFS spectrum, using an automated algorithm based on the Fourier content of the XAFS spectrum. Data analysis was accomplished using a WinXAS software program while amplitude and phase shift function for fitting protocols were calculated by FEFF 8.2 [110-112]. Atoms was used to produce crystallographic input files for generation of complexes structural information [113]. All k^3-weighted EXAFS spectra were adjusted using a $S^2_0 = 0.9$ constraint and single value energy shift (ΔE_0) was used for all scattering events.

4.2 Single Crystal X-ray Diffraction (XRD)

X-ray crystallography is the study of crystal structures through X-ray diffraction techniques. When an X-ray beam bombards a crystalline lattice in a given orientation, the beam is diffracted in a reproducible manner characterized by the atomic structure of the lattice. This diffraction occurs when the wavelength of X-rays and the interatomic distances in the lattice have a similar magnitude. X-ray crystallography is a well-known technique for understanding the three-dimensional structures of chemical compounds such as atomic composition, orientation, chemical bonding angles, and bond lengths between the atoms. This structural knowledge provides part of the basis for understanding and predicting the chemistry of the entire molecule, as well as its subcomponents and functional groups [114].

Theory of Operation

Monochromatic X-rays are coherently scattered from the electrons of an atom because the electron oscillates in the electric field of the beam. The oscillating electron then produces an X-ray with the same frequency of the incoming beam [115]. Each atom within an ordered crystalline compound will contribute to the overall pattern of scattering. The X-rays will add constructively or destructively depending upon the direction of the diffracted beam and the positions of the atoms within the unit cell. Constructive interference follows Bragg's law, equation 4-5 [116]:

$$2d \sin \theta = n\lambda \qquad \text{(eq. 4-5)}$$

where θ is the angle of incident (Bragg angle), λ is the wavelength of the incoming X-rays, d is the lattice plane spacing and n refers to the diffraction order. The d-spacings are based upon the positions of the atoms in the unit cell, while the intensities of the reflections are a function of the types of atoms present in the compound which leads to the structure factor, equation 4-6:

$$F_{hkl} = \Sigma F(h,k,l)\exp[-2\pi i(hx + ky + lz)] \qquad \text{(eq. 4-6)}$$

In single crystal X-ray diffraction experiments, λ is fixed and the diffraction conditions of the structure are solved by changing the orientation of the crystal. Since the intensity of the Bragg reflection is proportional to the square of the structure factor, a single crystal experiment can measure the position of the diffraction area, and its intensity. Ultimately, this gives the symmetry of the internal structure, the atomic positions, and the composition of the compound [116].

X-ray diffractometers consist of three basic elements, an X-ray tube, a sample holder, and an X-ray detector. X-rays are generated in a cathode ray tube by heating a filament to produce electrons. The electrons are then accelerated toward a target material by applying a voltage. When electrons have sufficient energy to remove the inner shell electrons of the target material, characteristic X-ray spectra are produced. These spectra contain several components with the most common being K_α and K_β. The K_α contains a $K_{\alpha1}$ and $K_{\alpha2}$ component where $K_{\alpha1}$ has a slightly shorter wavelength than $K_{\alpha2}$ and twice the intensity [117].

The specific wavelengths are characteristic of the target material. Filtering, by foils or crystal monochrometers, is required to produce monochromatic X-rays needed for diffraction. $K_{\alpha 1}$and $K_{\alpha 2}$ are sufficiently close in wavelength such that a weighted average of the two can be used. Molybdenum is the most common target material for single-crystal diffraction, with MoK_{α} radiation = 0.7107 Å. The X-rays are collimated, directed onto the sample, and constructive interference occurs when the correct geometry of the incident X-rays striking the sample is reached. A detector records and processes the X-ray signal, converts it to a count rate which is sent to a printer or computer for analysis. X-rays may also be produced using a synchrotron, which emits a much stronger beam [117]. Single-crystal diffractometers use either 3-circle or 4-circle goniometers. These circles refer to the four angles (2θ, χ, φ, and Ω) that define the relationship between the crystal lattice, the incident ray, and the detector. Figure 19 depicts these angles within the instrument using a diagram of a 4-circle goniometer [117].

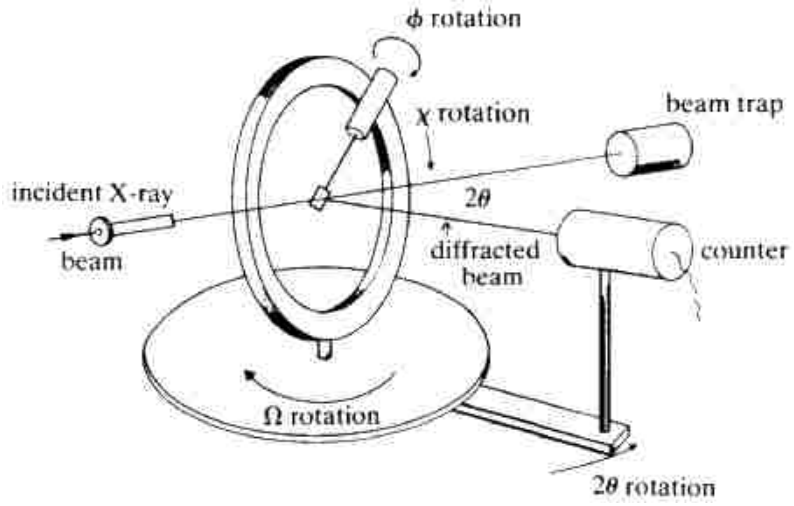

Figure 19 Schematic of 4-circle diffractometer; the angles between the incident ray, the detector and the sample [117].

Samples are mounted on thin fibers or into thin capillary tubes for radioactive samples, which are attached to brass pins and mounted onto a goniometer head. Adjustment of the X, Y, and Z orthogonal directions allows the crystal to be centered in the X-ray beam while the use of a collimator directs the X-rays at the sample. X-rays are either transmitted through the crystal, reflected off the surface, or diffracted by the crystal lattice. A beam stop is located directly opposite the collimator to absorb any transmitted X-rays and protect the detector. The detector will only collect X-rays that fit a predetermined alignment based on the X, Y, and Z angles [117]. Modern single-crystal diffractometers use CCD (charge-coupled device) technology to process the X-ray photons turning them into an electrical signal which can be analyzed by a computer program [117].

System Specification

Single crystal diffraction data was collected for suitable single crystals on a three circle Bruker single crystal X-ray diffractometer equipped with monochromatic MoKα(λ = 0.71073 Å) and an APEX II CCD detector. Charge-coupled device detectors are attributed with current advances in X-ray crystallography. The CCD detector allows for simultaneous recording of many reflections leading to a reduction of incorrect cells, faster data collections, and better crystal screening [118]. Diffraction data for all samples were collected at room temperature and standard atmospheric conditions. The Bruker instrument used for the Am crystal measurement is shown in Figure 20.

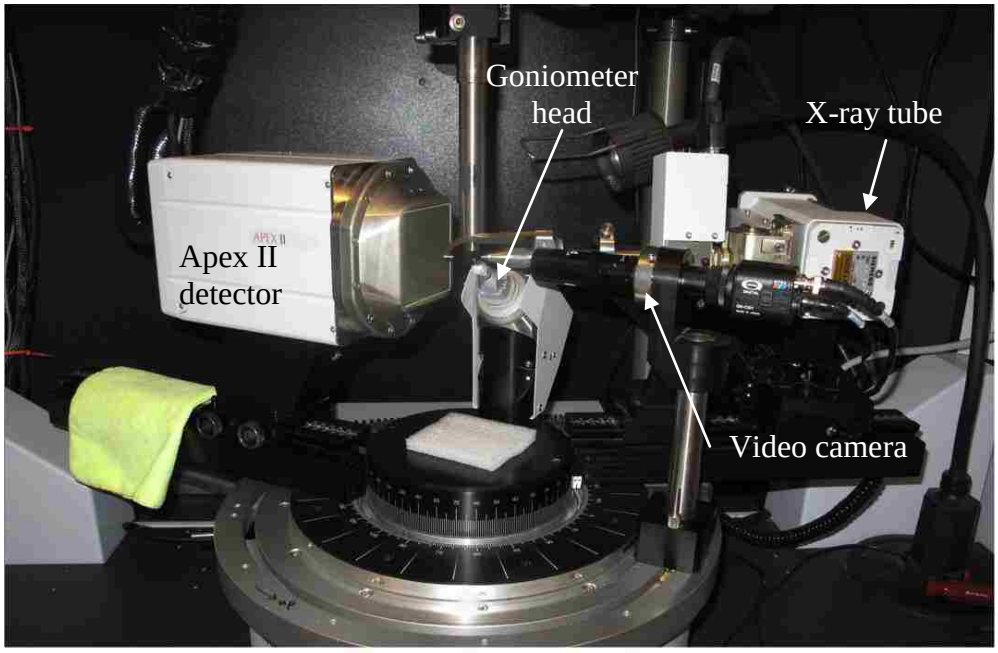

Figure 20 Bruker single crystal X-ray diffractometer with Apex II detector.

Sample Preparation and Measurement

A needle crystal of 0.05 × 0.05 × 0.40 mm^3 was selected for geometry and intensity data collection with a Bruker SMART APEXII CCD area detector on a D8 goniometer. The temperature during the data collection was controlled with an Oxford cooler. Preliminary lattice parameters and orientation matrices were obtained from three sets of frames.

Data Analysis

The unit cell parameters were determined using the Bruker software SMART and the data was integrated using SAINT [119]. Data integration was performed using an APEX II CCD detector in combination with the Bruker APEX II suite of software for unit cell parameters [120]. Lorentz and polarization corrections were applied to the data

using the Bruker program XPREP [119]. Absorption corrections were performed using XPREP, a semi-empirical modeling program. Structures were solved using the direct method and refined on F^2 with a SHELXTL program [119, 121]. Atomic scattering factors for each atom were taken from International Tables for X-ray Crystallography [118, 122]. The standard uncertainty values of these parameters are very complex and depend on the minimized function, the number of data and parameters, and the diagonal elements of the inverse least squares matrix. Low uncertainty values for data are achieved by obtaining good agreement between experimental and calculated values as well as a utilizing a large volume for reproducibility [115].

4.3 Principles of Ultraviolet-Visible Spectrometry

UV-Visible spectroscopy was employed for experiments related to the oxidation of Am. The following section will provide information on the theory behind this spectroscopy method, specification of the instrument used followed by sample preparation, measurement and data analysis.

Theory of Operation

UV-Visible spectroscopy is based on how much light is absorbed by a sample and follows the Beer-Lambert's law in equation 4-7:

$$A = \varepsilon bc \qquad \text{(Eq. 4-7)}$$

where A is the measured absorbance, ε is the wave-length dependent molar absorptivity of the analyte, b is the path length, and c is the concentration of the analyte.

Experimental measurements are usually made in terms of transmittance (T), which is defined in equation 4-8 as:

$$T = I / I_o \qquad \text{(Eq. 4-8)}$$

where I is the light intensity after it passes through the sample and I_o is the initial light intensity. The relation between A and T, shown in equation 4-9, is:

$$A = -\log T = -\log (I / I_o) \qquad \text{(Eq. 4-9)}$$

Modern absorption instruments can usually display the data as transmittance, %-transmittance, or absorbance. An unknown concentration of an analyte can be determined by measuring the amount of light that a sample absorbs and applying Beer's law. If the absorptivity coefficient is not known, the unknown concentration can be determined using a working curve of absorbance versus concentration derived from standards. Using published values of applicable molar absorptivities and samples of fixed path length, one can use Beer's Law (Eq. 4-7) to determine an unknown concentration of a given species. Conversely, an unknown samples concentration can be determined by creating a calibration curve of A verses *c* for a given wavelength thereby using the slope to determine ε for the unknown sample [123].

Ultraviolet visible absorption spectrometry is useful for the identification and characterization of many absorbing species. All organic compounds have valence electrons that can be excited by radiation absorption. The excitation produces broad

spectra bands that generally due to the superposition of multiple overlapping transitions. These bands have the potential to yield information about the functional groups in the compound. Many inorganic anions, including nitrate, absorb at UV wavelengths due to the excitation of non-binding electrons. Cations and complexes of transition metals which are active in the UV-Visible region have broad absorption bands in at least one oxidation state and are therefore colored. Because these broad absorption bands are readily affected by ligand bonding with outer electrons on the metal ion, they are very sensitive to speciation behavior. In contrast, lanthanides and actinides exhibit narrower bands due to light absorption in the 4*f* and 5*f* electron shells that effectively shields the outer electrons from the effects of ligand bonding [124].

System Specification

To make spectroscopy measurements related to verification of Am oxidation states and sodium bismuthate presence, UV-Visible was used and this instrument is shown in Figure 21. The UV-Visible Cary 6000i spectrometer was used which employees two lamps (deuterium and tungsten halogen) to cover an operating range from 175 to 1,800 nm. The light produced, by either light source, passes through a double out-of-plane Littrow monochromator and through a split into a chopper system [125]. The chopper divides the light beam into three beams: one to the sample, one to the reference sample and one is blocked completely. After the beam is divided, it is sent through the sample and reference cells into the R928 PMT located in the detector [125]. The sample compartment allows for different sample holders such as a fiber optic module for connection with a waveguide or individual sample holder to be used with standard cuvettes with or without a reference.

Figure 21 Cary 6000i UV-Visible with Ocean Optics 100cm liquid waveguide.

The Ocean Optics 100 cm liquid waveguide was used in a radioactive contamination hood for UV-Visible determination of Am oxidation states. This procedure was used to keep the high levels of alpha contamination associated with ^{243}Am contained in a closed system keeping the Cary 6000i instrument clean. For sodium bismuthate measurements, the cuvette sample holder module was used in order to directly measure both filtered liquids and liquids with solid components. Complete system specifications for the Cary 6000i can be found in the literature [126].

Sample Preparation and Measurement

For the Ocean Optics liquid waveguide, sample solutions were placed in 5 mL volume syringe at a sample volume of 1 mL which is sufficient sample size for this waveguide. The radioactive and non-radioactive samples were prepared at specific concentrations to allow for absorbance measurements in the range of 0-1 (corresponding to 0-90% absorbance of light). However, the Cary 6000i spectrometer can accurately

measure absorbance up to 5 (99.999 % of light absorbed by the sample) [126]. Apertured cells, for reduced volume, were also used for measurement of both radioactive and non-radioactive samples. The samples were prepared and the absorbance measured at the same parameters as for the waveguide. Prior to the measurements, two parallel sides of the cuvettes were cleaned with a Kimwipe to remove any oil on the external surface. The cuvette was placed into the sample compartment with the clean sides facing the incoming beam and the detector. Each cuvette was cleaned with HPLC grade water and dried with Kimwipes before loading a new sample. The waveguide was cleaned by injecting HPLC grade water through the system followed by dilute HNO_3 and a final rinse of HPLC grade water prior to injecting a new sample.

A matrix blank was measured first, followed by the samples of interest which were measured relative to the blank for the waveguide and the reference beam for low volume cuvettes. A matrix blank was injected into the waveguide prior to the sample for use as a background correction and was measured by the spectrometer in the same manner as the sample containing the analyte. For samples using cuvettes, matrix blanks and samples containing an analyte(s) were measured by the spectrometer with respect to a reference beam. All measurements were performed for the range of 400-1050 nm with other operating parameters summarized in Table 4.

Table 4 General operating parameters for sample measurement with the Cary 6000i spectrometer [126].

Parameter	Setting
Y Mode	Absorbance
X Mode	nm
Scan rate	600.00 nm/min
Data interval	1.000 nm
Source changeover	350.00 nm
Detector changeover	800.00 nm
Grating changeover	800.00 nm

The absorbance data as a function of wavelength was collected with the Cary WinUV software and stored as comma-separated values (CSV) files for analysis. In addition to the automatic internal calibration checks ran by the instrument during each startup (deuterium emission lines at 2624.4 nm, 1312.2 nm, 656.1 nm, 486.0 nm and 0 % transmittance), a complete instrument performance test was performed prior to the first measurement to check for wavelength reproducibility, wavelength accuracy, baseline flatness, maximum resolution and photometric noise.

Data Analysis

All data analysis was performed offline with the raw spectra converted to CSV files analyzed in excel. For UV-Visible data, absorbance values corresponding to the peaks of interest were identified and isolated as necessary for quantitative analysis, Eq. 4-7. To obtain complete absorbance spectra of specific samples for comparison, absorbance was plotted as a function of wavelength.

4.4 Principles of Scanning Electron Microscope

The scanning electron microscope (SEM) uses a focused beam of high-energy electrons to generate a variety of signals at the surface of solid specimens. The signal response is an indication of the interaction between the electrons and the sample producing information on the composition of the sample. This information includes chemical composition, crystalline structure, and complex orientation of component matrix within the sample [127]. In most applications, data is collected over a selected area of the surface of the sample, and a 2-dimensional image is generated that displays spatial variations. Areas ranging from approximately 1 cm to 5 microns in width can be imaged in a scanning mode using conventional SEM techniques with magnification ranging from 20X to approximately 30,000X, with spatial resolution of 50 to 100 nm. The SEM is also capable of performing analyses of selected point locations on the sample. This feature is useful for qualitatively or semi-quantitatively determining chemical compositions (using energy-dispersive X-ray spectroscopy**,** EDS), crystalline structure, and crystal orientations (using electron backscattered diffraction, EBSD). The SEM is similar to an electron probe micro-analyzer (EPMA) as far as design and both instruments can perform many of the same functions [128, 129].

Theory of Operation

Accelerated electrons in an SEM carry significant amounts of kinetic energy. This energy is dissipated as electron-sample interactions that produce signals when the incident electrons are decelerated in the solid sample. These signal include:

- Secondary electrons for the production of SEM images.
- Backscattered electrons (BSE).
- Diffracted backscattered electrons (EBSD), for determination of structure.

- Photons, for elemental X-ray analysis.
- Visible light (cathodoluminescence).
- Heat.

Secondary electrons are used in imaging and are valuable for showing morphology (surface texture) and topography on samples. Backscattered electrons prove important for illustrating contrasts in composition in multiphase samples [126]. X-ray generation is produced by inelastic collisions of the incident electrons with electrons in discrete orbital's (shells) of atoms in the sample. As the excited electrons return to lower energy states, they produce X-rays with specific wavelengths indicative of the difference in energy levels associated with electrons in given shells of an element. In this way, characteristic X-rays are produced for each element in a mineral that is "excited" by the electron beam. SEM analysis is considered to be "non-destructive" since the X-rays generated by electron interactions do not lead to sample loss so the same sample may be analyzed repeatedly [129].

System Specification

Initial analysis of crystal compounds was necessary for verification of component integration was performed using an SEM shown in Figure 22. The JEOL Inc. JSM 6610 SEM with Energy-dispersive X-ray spectroscopy (EDS), Electron backscatter diffraction (EBSD), Cathodoluminescence (CL), and Focused Ion Beam (FIB) utilizes an electron beam whose wavelength is shorter than that of light and therefore observing a structure down to several nm in scale becomes possible.

Figure 22 JSM 6610 SEM.

The SEM column is equipped with a Schottky thermal field emission gun that provides a resolution < 2.5 nm for accelerating voltages between 0.2 to 30 keV. Up to 30 keV ion column with a gallium metal ion source provides currents ranging from 1 pA to 40 nA. Ion beam imaging uses secondary electrons to produce fine resolution on the order of 7 nm at 1 pA beam current and the tandem use of both ion and electron microscopes has a synergistic effect that expands the capabilities of these instruments. [130]. Figure 23 shows a schematic of the structure of the SEM which consists of an optical system for generating the electron probe, a sample platform, a detector for secondary electrons, an image display screen, and electronic instrumentation for operation and analysis. Figure 24 shows an internal camera view of the SEM chamber where the specimen stage and objective lens can be seen.

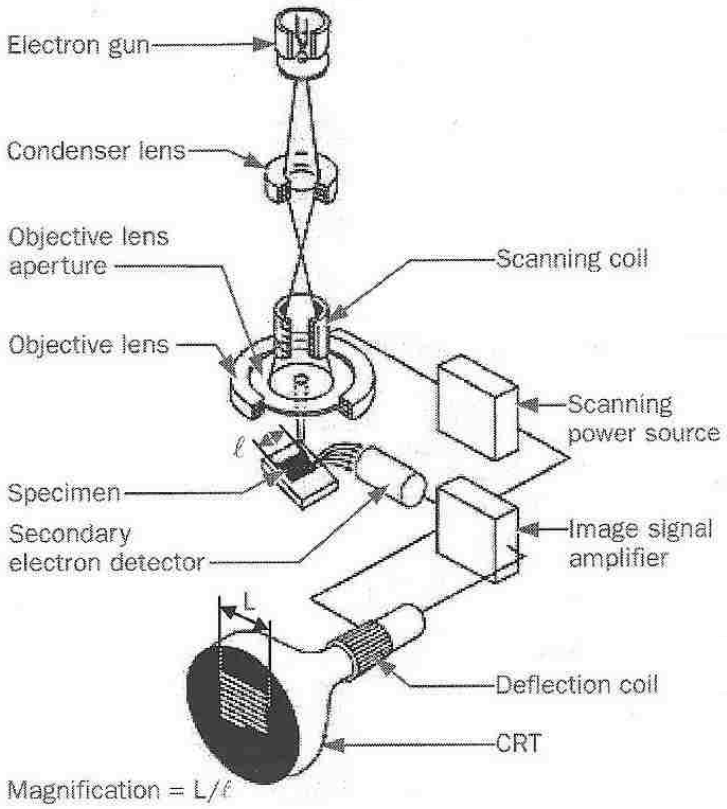

Figure 23 Schematic of JMS 7600 SEM [130].

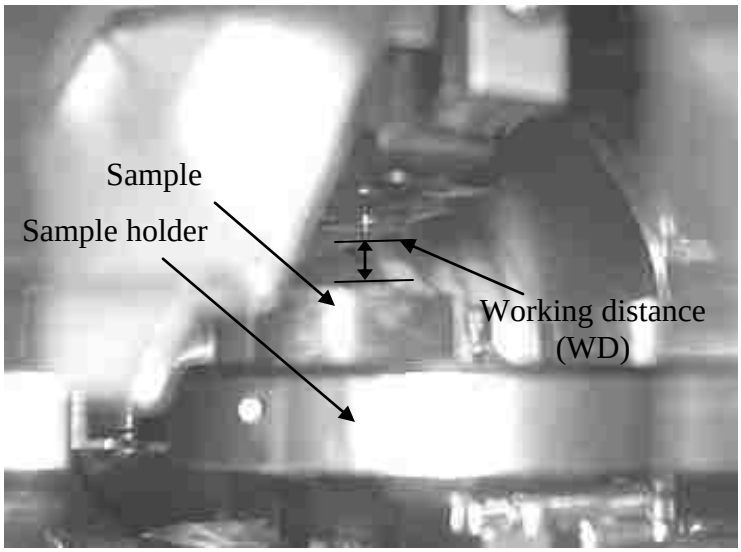

Figure 24 Internal camera image of the JMS 7600 chamber showing the sample holder, sample and working distance (WD). WD is the distance between the sample surface and the objective lens.

Sample Preparation and Measurement

When preparing a suitable sample for SEM analysis, multiple parameters must be considered such as, size, shape, and potential air oxidation of the sample [131]. The SEM chamber allows for a sample size of 5-10 cm in diameter and the crystal samples prepared for analysis in this work were, on average, 1.5 mm on edge. The non-metalic samples chosen for SEM analysis had to be made electrically conductive, at least at the surface, and electrically grounded to prevent the accumulation of electrostatic charge at the surface. Nonconductive specimens tend to charge when scanned by the electron beam, and especially in secondary electron imaging mode, this causes scanning faults and other image artifacts. For this reason the crystal samples were coated with an ultrathin coating of electrically conducting platinum deposited on the sample by low-vacuum sputter coating in an inert argon atmosphere. The sputter coater is a Hummer 6.2 from Anatech USA shown in Figure 25 [132].

Figure 25 Anatech USA, Hummer 6.2 sputter coater.

Data Analysis

The SEM operating system for image analysis was the JEOL PC SEM version 1,0,3 and the energy dispersive analyzer of X- rays INCA version 4.15 (Oxford Instrument) [130]. The detectors used in this work were the low electron image (LEI) secondary electron detector and the low angle backscatter electron detector (LABe). The LABe detector collects both high and low angle backscattered electrons at low kV and high spatial resolution and provides more surface detail & compositional contrast. The LEI detector provides good topographical contrast, but the image is coarser and for this reason the LABe detector was typically used in this work.

4.5 Principles of Gamma Spectrometry

High Purity Germanium (HPGe) detectors provide the best energy resolution so that simple peak-fitting techniques may be used. Gamma ray detectors are of two types, high resolution, based exclusively on cryogenically cooled germanium (HPGe) detectors or medium to low energy resolution based on scintillators or room temperature semiconductors. For this work, an HPGe detector was used in coordination with a sample changer robot.

Theory of Operation

Gamma-rays are a form of electromagnetic radiation, which are emitted at discrete energies that can identify the nuclide of interest. They primarily interact with atomic electrons in ways that allow them to be detected. Gamma-rays interact in three possible ways; photoelectric effect, Compton scattering, and pair production with each mode acting upon the atomic electrons differently [133].

In a photoelectric event, the entire photon energy is absorbed by a bound atomic electron which is ejected with a kinetic energy equal to the photon energy less the binding energy of the electron. During this process, an increase in the cross section coincides with increasing atomic number from approximately Z^4 to Z^5, while a rapid decrease in the cross section with increasing photon energy ($\sim E^{-3}$) is also seen [130]. The residual ion may emit an X-ray or Auger electron and the low energy X-rays are generally absorbed in a second photoelectric event prior to escaping the crystal structure. As a result, the total photon energy appears as electron kinetic energy. Thus, a monoenergetic gamma ray gives rise to a monoenergetic peak in the charge distribution corresponding to the incident photon energy. The kinetic energy imparted to the electron is between zero and an upper value related to the energy of the photon. Between these limits, the scattering results in a continuous electron energy distribution known as the

Compton Continuum. The cross-section for this process is proportional to the atomic number of the scattering material and somewhat less energy-dependent than the photoelectric effect.

The maximum energy in the Compton continuum is called the Compton Edge (*CE*). It is the maximum energy imparted to the scattered electron and occurs when the scattering angle is 180°. Events that exceed the CE energy are generally photoelectric in nature. Figure 26 shows the Compton Effect and equation.

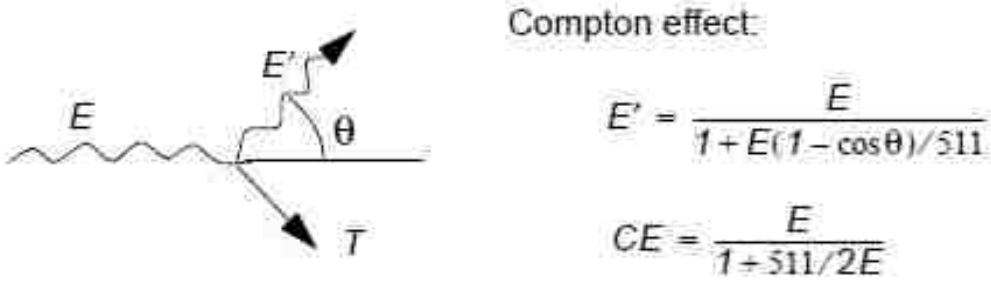

Figure 26 Compton effect. E = energy of incident photon (keV); E'= energy of scattered photon (keV); T = kinetic energy of the scattered electron; θ = scattering angle; CE = Compton edge, T when θ = 180°

Pair production differs from the photoelectric effect and Compton scattering, which are possible at all energies, because it has an energy threshold equal to the combined positron-electron rest mass of 1.02 MeV. In pair production the interacting gamma-ray passes near an atomic nucleus and converts into an electron/positron pair if the incoming gamma energy is greater than 1.02 MeV. The positron produced by the pair-production process undergoes annihilation with an electron and gives off gamma-

rays with energies of 511 KeV each. The photoelectric effect, Compton scattering, and pair production each play a specific role in how the final spectrum appears. The photoelectric effect produces peaks that are characteristic of the sample in the spectrum while Compton scattering produces a continuum between the peaks. Pair production produces peaks at 511 KeV and 1.02 MeV which are indicative of an electron and positron escape peak, respectively. The Photopeak and Compton Continuum are illustrated in Figure 27.

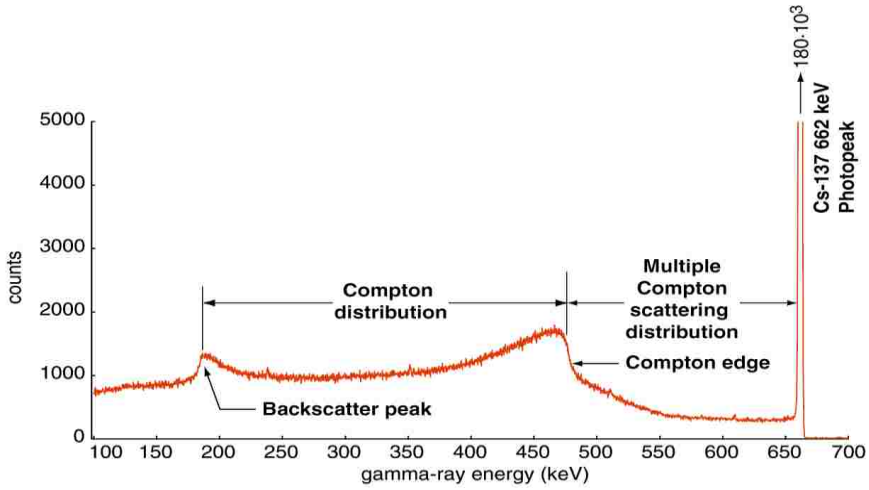

Figure 27 Photopeak and Compton Continuum [133].

This annihilation translates into an escape peak and is related to the size of the detector. For the detector used in this work, the signal for ^{137}Cs was quantified at 661 KeV and ^{85}Sr at 514 KeV for calibration. A planar detector, the simplest of the germanium detectors, can be used to explain how gamma-ray energies are detected. Electrodes, one positive and one negative, are attached to opposite sides of the crystal and high voltage is applied. This sweeps the electrons produced by gamma-ray ionization of the germanium into the

conduction band where they are collected and measured. The number of electrons measured is related to the photon energy. The entire photon energy (E) is converted to the kinetic energy of the positron-electron pair (i.e., E - 1.022 MeV) including the rest mass of the pair. The positron is annihilated by an atomic electron, producing two 0.511 MeV photons emitted at 180° to each other, of which none, one, or both may escape. The spectral distribution, then, includes a full energy peak (FEP), a single escape peak (SEP), and a double escape peak (DEP) [133]. Single and double escape peaks are produced during pair production events when the incident gamma energy is above 1.022 MeV. These events can produce two 511 keV annihilation gamma-rays which can escape the detector and produce peaks in the spectrum. If only one gamma-ray of the pair escapes and the other is absorbed in the detector, 511 keV will be subtracted from the characteristic gamma peak resulting in a single escape peak shown in Figure 28. If both of the annihillation gamma-rays escape, a double escape peak at 1002 keV below the characteristic gamma peak is seen [134].

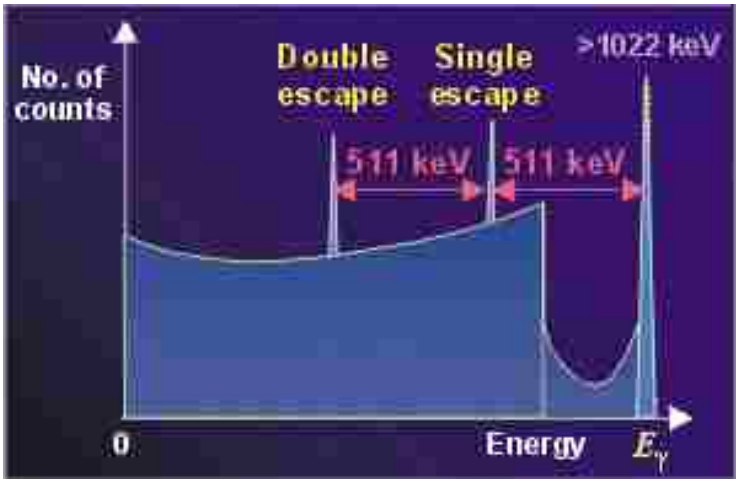

Figure 28 Single and double escape peaks produced by pair production [135].

System Specification

All HPGe radiation detectors are large, reverse-biased diodes. A p-type ORTEC® GEM50P4-83 HPGe detector was used in this work shown in Figure 29. The p-type (as

Figure 29 ORTEC® GEM50P4-83 HPGe gamma ray detector with robotic sample changer.

well as other types) depends on the concentration of donor or acceptor atoms in the crystal. In order to amplify the signal, the diode is connected to electrical circuits attached to the crystal. Figure 30 shows a schematic of the thin, ion-implanted electrical contacts on the crystal for the P+ contact on the GEM50P4-83 HPGe detector.

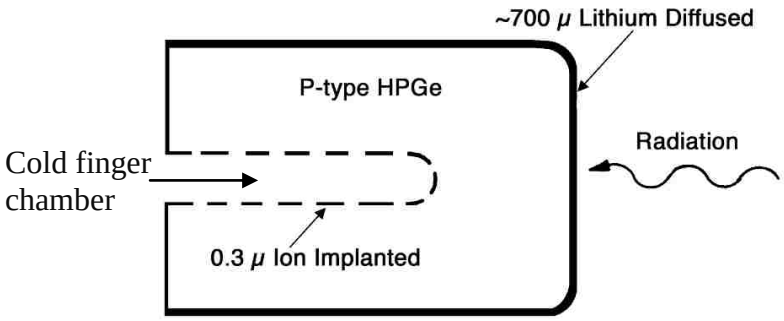

Figure 30 P-type HPGe crystal schematic.

The detector is cooled by a LN_2 cryogenic tank and a cold finger shown in Figure 30. The HPGe detector was used to establish isotopic concentrations for the Am samples. The ORTEC® GEM50P4-83 (relative efficiency 50%, resolution 1.90 keV FWHM at 1332 keV), a digital signal processor ORTEC® DSPEC jr 2.0, and a personal computer running the software for data acquisition and processing ORTEC® Gamma Vision 6.0 [136]. The energy, resolution and efficiency calibrations were carried out by a standard multi-gamma source in two counting positions, in contact with (position 0) and 8 cm far (position 8) from the head of the detector.

Sample Preparation and Measurement

All samples were prepared in 0.5 - 1 M HNO_3. The robot autosampler was used for all measurements and the sample vials were standard scintillation vials with a sample volume of 0.5 mL. Operating parameters, which were controlled through the GammaVision-32 software, were standardized for all measurements.

Data Analysis

ORTEC® GammaVision-32 Gamma Spectrum Analysis Software was used for the analysis of gamma-ray spectra acquired with HPGe detector. A general purpose

analysis method called WAN32 was used for all nuclide samples [136]. The WAN32 analysis method uses a library of nuclides to direct the determination of peak areas in the spectrum. A secondary peak search is used to provide possible candidates peaks which might interfere with other peaks listed in the library as well as providing a list of unknown peaks and suspect peaks in the spectrum. Minimum detectable activities may be reported if required on both identified and unidentified library nuclides. Reports were generated based on the summary of nuclides in the sample and included: peak channel, net area counts, activity in Bq based on count time, corrected activity in Bq, and uncertainty. The ^{243}Am samples were analyzed at the 74 KeV energy line in order to establish activity levels for samples used in the oxidation experiments. Exact activities were necessary for sample preparation in XAFS, UV-Visible, and crystal synthesis experiments.

CHAPTER 5

CHARACTERIZATION OF AMERICIUM (V/VI) WITH XAFS

In support of characterizing Am speciation in higher oxidation states, a series of experiments were performed to further investigate the role of sodium bismuthate in the oxidation of Am(III) to Am(V) and Am(VI) in acidic solution. X-ray Absorption Fine Structure spectroscopy was utilized as a tool to obtain information on the speciation of Am(V) and Am(VI) in HNO_3. Results of all these studies are presented in this chapter. Initial studies of Am(III) using XAFS provided the basis for expanding this characterization method to higher oxidation states of Am. Many studies have characterized Am(III) in both liquid and solid states using XAFS, however, there are few published studies on Am(V) and Am(VI) using XAFS [137-140].

5.1 Experimental

Reagents and Radioisotope Solutions

Initially, all chemicals were purchased from Sigma-Aldrich and used as received. The sodium bismuthate from Sigma-Aldrich was found to contain peroxide contaminants and was ultimately replaced with "peroxide free" sodium bismuthate (ACS grade, 93%) from Chemsavers. Peroxides have the effect on oxidized species of reducing them to their lowest stable oxidation state which in the case of Am would be Am(III). The HNO_3 solutions were prepared by volumetric dilution of concentrated HNO_3, trace metal grade, with an assay of 70%. All working solutions were prepared with HPLC grade nano-pure

DI-water in a volumetric flask. Further details on the composition of radioactive and non-radioactive solutions are provided in Table 5.

Table 5 List of working solutions for radioactive and non-radioactive samples.

Sample Component	Concentration range (M)	Sample size (mL)
^{243}Am	0.001 − 0.015	0.1 – 1.0
sodium bismuthate	0.1 – 0.2	0.1 – 1.0
HNO_3	0.1 − 9.0	0.1 – 1.0

Americium stock solutions

The radionuclide used in this study was ^{243}Am ($t_{½}$=7.37x10^3 years) provided by Idaho National Laboratory. The ^{243}Am stock solution used in the XAFS samples was prepared by dissolving between 10 to 28 mg of ^{243}Am dioxide (AmO_2) solid in 0.5 to 1.0 M HNO_3. The resulting ^{243}Am concentration ranged from 1x10^{-3} to 1.5x10^{-2} M in solution for the ANL/APS and SSRL samples, respectively. Americium samples for UV-Visible analysis had a concentration of 3x10^{-5} M for the 100 cm pathlength waveguide and between 1x10^{-3} and 1.5x10^{-2} M for the 1 cm pathlength cuvettes.

UV-Visible studies

Prior to preparation of samples for XAFS measurements, solutions of the metal ion, acid, and oxidizing agent concentrations were prepared in order to confirm the Am oxidation states. UV-Visible was also used to establish optimal HNO_3 concentrations for use with the sodium bismuthate and to establish which concentration of acid versus oxidizing agent would give the most stable Am oxidation [10, 12, 59]. Ultimately, ~60

mg/mL of sodium bismuthate in 1 M HNO_3 and 0.5 M HNO_3 were chosen as optimal concentrations for the oxidation of Am(VI) and Am(V), respectively [45]. The sodium bismuthate in either 0.5 M or 1 M HNO_3 was contacted with ^{243}Am for a period of time ranging from 2 hours to 28 days, depending on the application, followed by centrifuging to separate the solid sodium bismuthate from the liquid. Initially, the sample preparation required lower concentrations of ^{243}Am for use in the Ocean Optics waveguide to establish the oxidation of the Am. The Am(VI)/sodium bismuthate in solution was contacted for 2 hours on a shaker table, centrifuged for 5 minutes, and the liquid was separated from the solid sodium bismuthate and filtered with a 0.22 μm Teflon filter prior to injection into the waveguide. For higher concentrations of ^{243}Am solutions oxidized to Am(VI), the same procedure was used as for the waveguide with the exception of the filtering step. The Am(VI) solution was delivered to an aperture, low volume cuvette along with a small amount of the solid sodium bismuthate in the bottom of the cuvette in order to keep the Am(VI) continuously oxidized. The solid in the bottom of the cuvette is allowed to settle and separate from the liquid phase prior to taking spectra in order to keep the distributed sodium bismuthate particles from interfering with the beam.

The Am(V) solutions were prepared in similar fashion to the Am(VI) samples with the following differences. The Am(V) solutions were prepared in 0.5 M HNO_3, contact time was 24 hours to 28 days with minimal, periodic shaking by hand. When using a cuvette, no solid sodium bismuthate was present in the sample. For both Am(V) and Am(VI) samples, HNO_3 concentrations from 0.1 M to 4 M were studied in order to evaluate the oxidation yield and stability.

Acid solubility studies were also performed on sodium bismuthate in order to establish an optimized solubility level in HNO_3. The sodium bismuthate was kept at a constant concentration of 60 mg/mL in an acid concentration range from 0.5 to 9 M HNO_3. The sodium bismuthate solutions were shaken over a 2 hour period on a rotating mixer, centrifuged for 5 minutes, the liquid separated and filtered with a 0.22 μm Teflon filter, and injected into the Ocean Optics waveguide. Prior to each sodium bismuthate sample run, a baseline subtraction was collected using the appropriate HNO_3 concentration in the waveguide. Sodium bismuthate samples that were not filtered after centrifuging were also prepared, only separated from the solid, and analyzed using a quartz cuvette.

X-ray Absorption Fine Structure sample preparation and measurement for ANL/APS

The final solutions were transferred into XAFS holders, sealed and shipped to ANL for XAFS measurements. All work related to sample preparation was performed in a radiological hood at the INL and shipped to UNLV for loading. The two XAFS samples contained ~6 μCi or ~0.03 mg of ^{243}Am with total volume of 100 μL (~1 mM ^{243}Am). Of the two samples, one contained ^{243}Am oxidized with sodium bismuthate, shown in Figure 31, and the other contained unoxidized Am(III), which was used as a baseline measurement.

Figure 31 Oxidized ^{243}Am in 1 M HNO_3 solution with sodium bismuthate before and after centrifuging.

Figure 32 Oxidized Am(VI) sample (0.001 M ^{243}Am in 1 M HNO_3 with ~2 mg $NaBiO_3$ excess solid on the bottom) prior to loading into the ANL/APS sample holder.

The oxidized Am sample contained a small amount of solid sodium bismuthate in the bottom of the sample, Figure 32. This was necessary in order to keep the Am(VI) in an oxidized state throughout transport to ANL and during the XAFS measurement, an elapsed time of approximately 5 days. Since sodium bismuthate has a low solubility,

~10% in 1 M HNO_3, it was supersaturated in the HNO_3 Am sample with a small amount of visible solid in the bottom of sample [10]. Detailed information on the composition of these working solutions is provided in Table 6. More general information on sample preparation and details regarding measurements and data analysis are provided in Chapter 4.

Table 6 ANL/APS sample preparation for XAFS measurement.

Sample #	Sample Components	^{243}Am (mM)	Sodium bismuthate (M)	HNO_3 (M)	Sample size (mL)
1	Am(III)	1.00	0	1.00	0.1
2	Am(VI) + sodium bismuthate solid	1.00	0.2*	1.00	0.1

*supersaturated sodium bismuthate solution with excess solid in the bottom of the sample vial.

X-ray Absorption Fine Structure sample preparation and measurement for SSRL

The sample preparation for SSRL differs slightly from the ANL/APS sample preparation and is described further in this section. The final solutions for this experiment were placed in holders and shipped to SSRL. All work related to sample preparation and sample holder loading was performed in a radiological hood at the INL. Six XAFS samples were prepared, however, only four samples were ultimately sent to SSRL due to holder failure and decontamination issues. The four samples contained ~0.74 mCi or ~4.2 mg/mL of^{243}Am with a total volume of 500 μL (~15 mM ^{243}Am). Of the four samples, two contained ^{243}Am oxidized to Am(V) and separated from the solid sodium bismuthate. One sample contained ^{243}Am oxidized to Am(VI) and in continuous

contact with the solid sodium bismuthate. The fourth and final sample contained unoxidized Am(III), which was used as a baseline measurement. The oxidized Am(VI) sample contained a small amount of solid sodium bismuthate in the bottom of the sample in order to keep the Am oxidized while in transport to SSRL and during the XAFS measurement. Detailed information on the composition of these working solutions is provided in Table 7. More general information on sample preparation, sample holders, details regarding the measurements and data analysis are provided in Chapter 4.1.

Table 7 Stanford Synchrotron Radiation Lightsource samples preparation for XAFS measurements.

Sample #	Sample Components	Sodium bismuthate (mg/mL)	HNO_3 (M)	Sample size (mL)
1	Am(III)	0	1.0	0.5
2	Am(VI) + sodium bismuthate solid	60[a]	1.0	0.5
3	Am(V)	60[b]	0.5	0.5
4	Am(V)	60[b]	0.5	0.5

[a] supersaturated sodium bismuthate solution with excess solid in the bottom of the sample vial.
[b] supersaturated sodium bismuthate solution with all solids removed.

5.2 Results and Discussion

Americium oxidation

Initial oxidation work using sodium bismuthate to oxidize Am proved to be difficult to reproduce. Solutions with the same concentration of Am and nitric acid would give random UV-Visible results. In some samples, the Am would oxidize, as expected from literature, to Am(VI) and ultimately reduce to Am(V) and Am(III).

However, in other cases only Am(V) would be seen in the spectra even in the presence of excess solid sodium bismuthate, and in other samples there would be no oxidation at all with only Am(III) present. The lack of reproducibility was traced to the sodium bismuthate oxidizing agent and is attributed to the manner in which the bismuthate is produced. Sodium bismuthate is synthesized using bismuth nitrate, sodium hydroxide and sodium peroxide that is fused, cooled, crushed and filtered with water. The route by which sodium peroxide is introduced is shown in the following reaction:

$$Bi + 6HNO_3 \text{ --> } Bi(NO_3)_3 + 3NO_2 + 3H_2O$$

$$2Bi(NO_3)_3 + 6NaOH \rightarrow Bi_2O_3 + 6NaNO_3 + 3H_2O$$

$$Na_2O + O_2 + Bi_2O_3 \rightarrow 2NaBiO_3$$

The reason for the intermittent oxidation, or non-oxidation, of Am was identified during this work, and previous unpublished work at INL, as a hydrogen peroxide contaminant. The redox behavior of hydrogen peroxide depends on the compound it is reacting with and the pH, so it can act as a reducing agent in the presence of oxidizing agents. Although the contamination with hydrogen peroxide was small, it was sufficient to affect the oxidation behavior of the low concentrations of Am in solution. The peroxide reduces the higher oxidation states of Am so the results showed either complete oxidation, partial oxidation, or non-oxidation of Am in any given experiment depending on the variable amounts of peroxide in each batch of bismuthate and the relative molar ratios of Am, peroxide, and bismuthate. This problem was resolved by using chemically purified sodium bismuthate from which the peroxide contaminant has been completely

removed by repeated washing of the sodium bismuthate with water. Sodium bismuthate is washed during the end of its production; however, it is only washed between 4-5 times with water which is not enough to remove all the peroxide. Using the new peroxide free sodium bismuthate, the UV-Visible results showed consistency in Am redox behavior. Extinction coefficients were determined (Figure 33) and the result for Am(III) at 503 nm was 386.7 ±19.3 L/mol·cm, for Am(V) at 513 nm 72.5 ±3.6 L/mol·cm, and for Am(VI) at 666 nm 27.9 ±1.4 L/mol·cm [10]. The extinction coefficients were obtained by measuring the peak heights for known concentrations determined by γ-ray spectroscopy and compared well with previous literature.

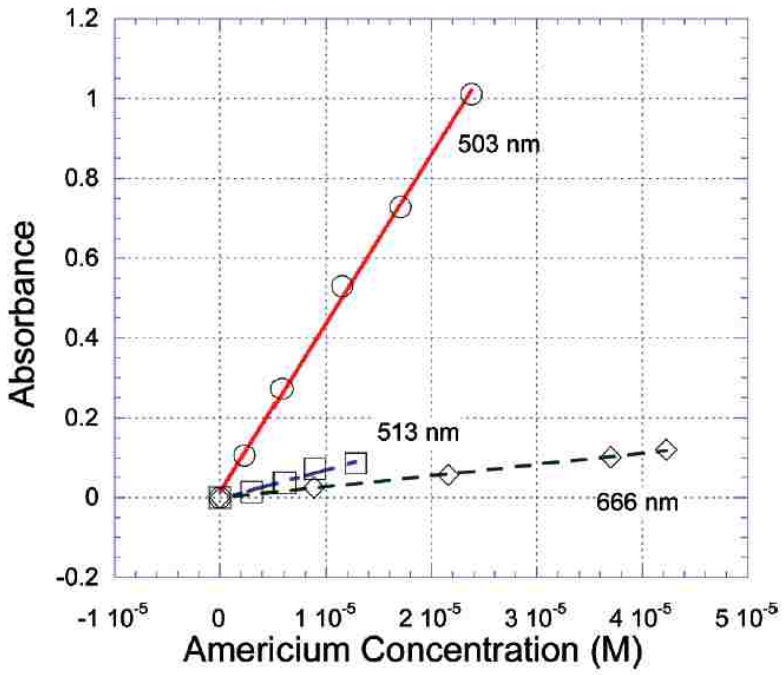

Figure 33 Extinction coefficients for Am(III) at 503 nm (386.7 L/mol·cm), Am(V) at 513 nm (72.5 L/mol·cm), Am(VI) at 666 nm (27.9 L/mol·cm) in 0. 1 M HNO_3 [10].

UV-Visible data used to establish preparation and sample parameters for the XAFS experiments revealed information that differed from previous literature [10-12, 59]. The results showed that the Am(VI) oxidation state was more stable than originally reported, so long as there was solid sodium bismuthate present during the data collection. The Am(VI) in 1 M HNO_3 was persistent over 8 days with no in-growth of Am(V) or Am(III) as long as there was excess sodium bismuthate present. Likewise, the Am(V) oxidation state was stable over a long period of time in the absence of an excess of sodium bismuthate. The Am(V) in 0.5 M HNO_3 was persistent over a 5 day period after separation from the excess solid sodium bismuthate and ultimately was persistent over much longer periods of time. As soon as the excess solid sodium bismuthate was removed, the Am(VI) completely reduced to Am(V) over a 10 hour period and <1% of Am(III) was present. There was no signification reduction of Am(V) to Am(III) in either short or long term contact tests using excess solid sodium bismuthate.

The UV-Visible results of Am(V) and Am(VI), oxidized with sodium bismuthate, are shown in Figures 34-37. All Am measurements were made from aqueous solutions of 0.5 M and 1 M HNO_3 and an initial concentration of saturated sodium bismuthate.

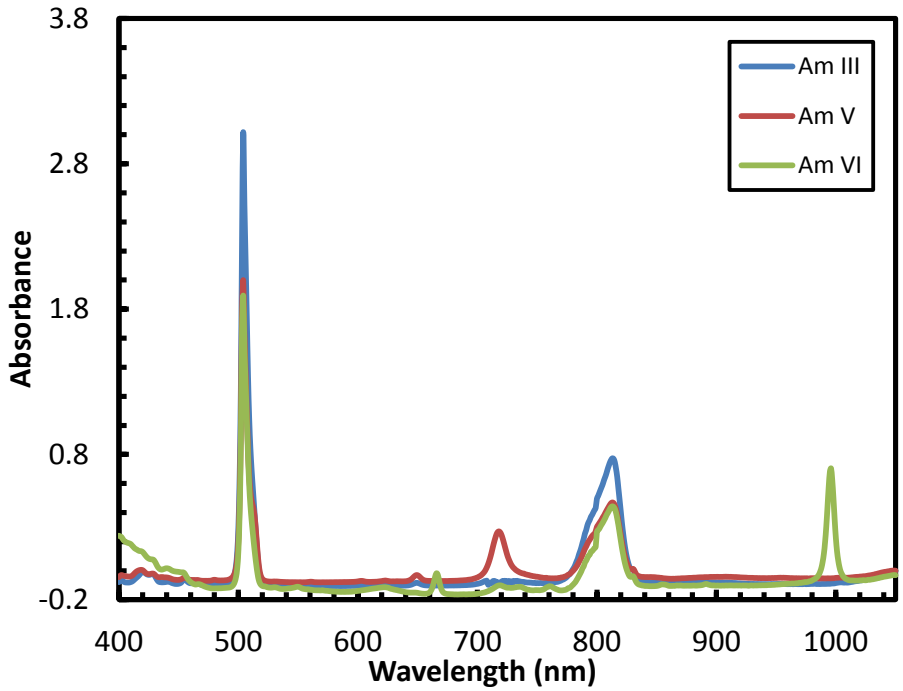

Figure 34 UV-Visible of Am(VI) after 8 days of contact with excess solid sodium bismuthate. Am(V) spectra was taken after the 8 day contact followed by separation from the excess solid sodium bismuthate and 5 days without bismuthate contact.

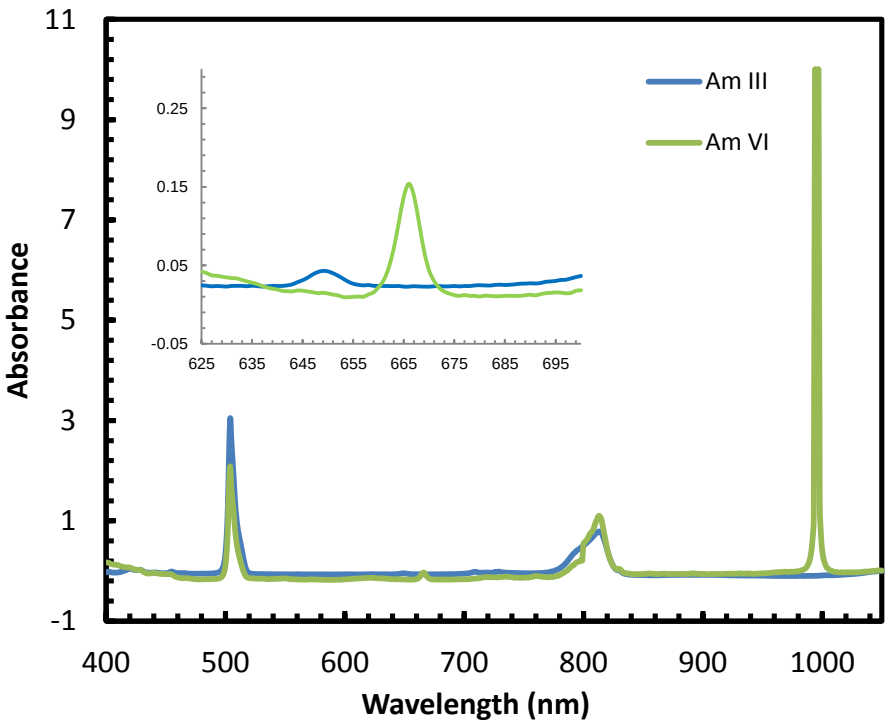

Figure 35 UV-Visible of Am(VI) in 1 M HNO_3 and in the presence of excess sodium bismuthate. A large peak at 996nm and small peak at 666 nm (enlarged in the inset) are indicative of the Am(VI) oxidation state.

The Am(VI) is produced in the presence of sodium bismuthate and is persistent, as shown in Figure 35, so long as there is solid bismuthate present in the nitric acid solution. In the absence of excess solid sodium bismuthate in solution, the Am(VI) rapidly reduces to Am(V). The Am(V) is very stable over time in the presence of sodium bismuthate, Figure 36, and this stability was shown over a 28 day contact period in which no Am(VI) was present in a 0.5 M HNO_3 solution and <1% of Am(III) had grown in. The Am(V) was also very stable for a period of days in the absence of excess solid sodium bismuthate, Figure 37, before complete reduction to Am(III) occurs.

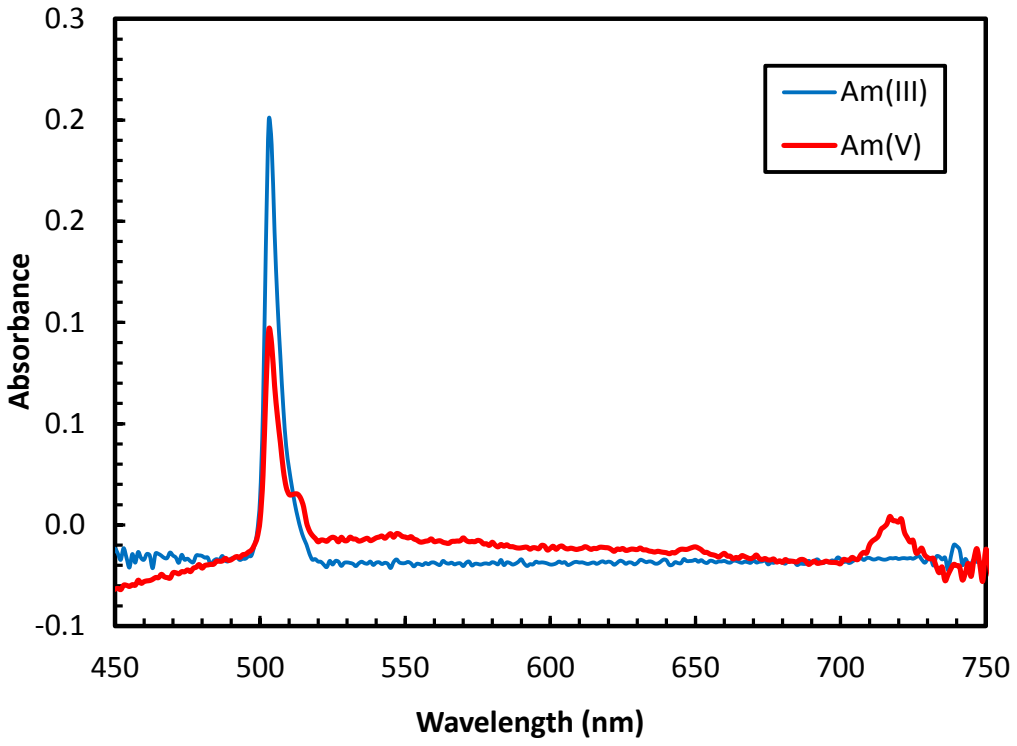

Figure 36 UV-Visible of Am(V) in 0.5 M HNO_3 in contact with excess solid sodium bismuthate for 28 days and separated from the solid prior to collecting spectra. The Am(III) baseline was from the same batch and aged alongside the oxidized sample.

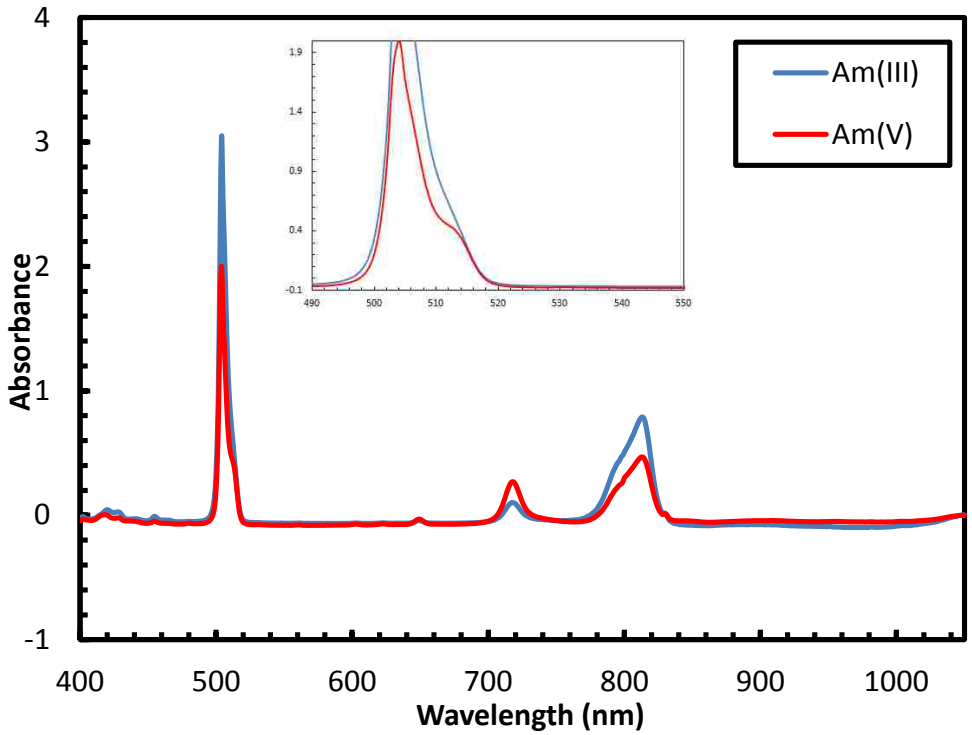

Figure 37 UV-Visible of Am(V) in 0.5 M HNO_3 in the absence of sodium bismuthate for 5 days. Am(V) peaks at 718 nm, 651 nm, and 513 nm are present and the 513 nm peak appears as a shoulder off the 503 nm Am(III) peak (shown enlarged in the inset).

Variations in acid concentration with respect to the dissolution of sodium bismuthate yielded interesting results. At higher nitric acid concentrations, more sodium bismuthate was dissolved and a higher yield of Am(VI) was found. However, in the case of Am(V), lower concentrations of nitric acid improved the stability with the likely cause being the lower concentration of acidity produced less bismuthate in solution making Am(VI) less stable than Am(V). The nitrate concentration did not seem to play a role in the stability of the oxidation states. Figure 38 shows UV-Visible spectra of the effects of acid concentration on sodium bismuthate absorption. The dissolution of sodium bismuthate yields Bi(V) in solution. There is the potential for Bi(V) reduction due to

peroxide production from water oxidation. The peroxide produced by water oxidation is a fast reducing agent for Am(VI), but the reduction process is greatly reduced for Am(V) [141]. It is possible the oxidation that is achieved is a balance between how much Bi(V) oxidizes Am, how much scavenges other reducing agents, and how much produces peroxide.

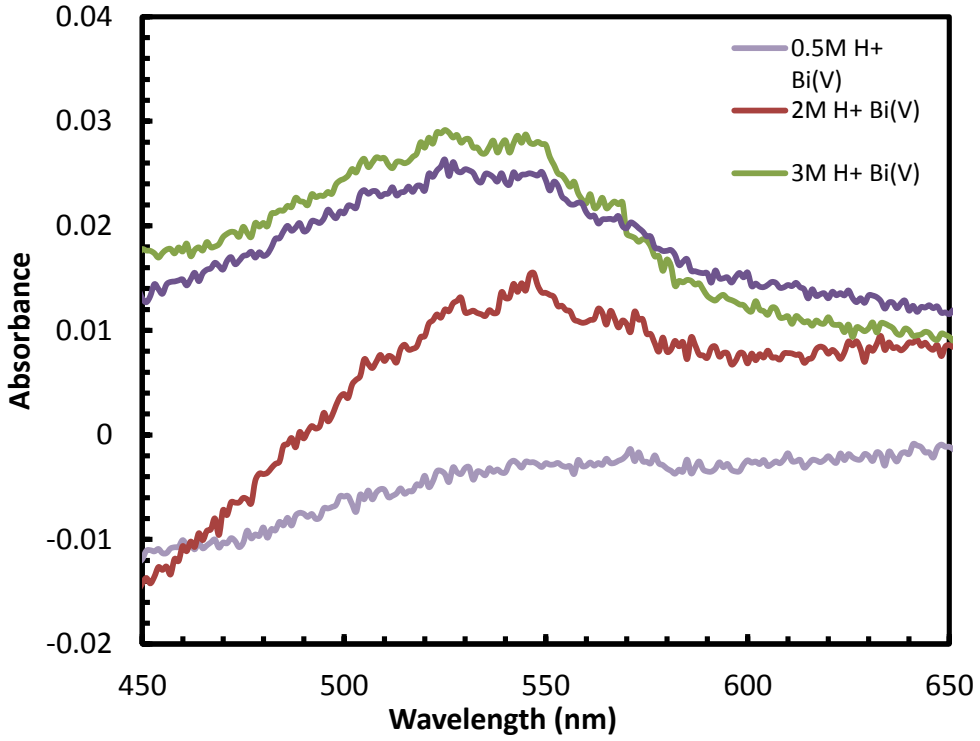

Figure 38 UV-Visible data of sodium bismuthate (Bi(V)) in varied HNO_3 concentrations. The same nitric acid concentration used in each sample was also used as a baseline subtraction prior to running the sample. Bi(V) absorbance can be seen from 450 – 600 nm with a peak around 550 nm.

Even though the higher concentrations of nitric acid produced higher concentrations of Bi(V) in solution, increase acidity has a negative effect on the oxidation stability of Am(V) and Am(VI). The choice of 0.5 M HNO_3 and 1 M HNO_3 for the

oxidation of Am(V) and Am(VI), respectively, for use in the XAFS samples is based on UV-Visible results for both short term and long term oxidation. Table 8 shows the relationship between HNO_3 concentration and Bi(V) solubility using sodium bismuthate, which is the basis for choosing 0.5 M and 1.0 M HNO_3 concentrations for oxidation of Am(III) to Am(V) and Am(VI) [11]. The Am sample solution was measured by gamma ray spectroscopy to verify the 0.015 M ^{243}Am sample concentration prior to oxidation and shipment to ANL/APS and SSRL.

Table 8 Concentration of Bi(V) in varied HNO_3 solution containing $NaBiO_3$ [11].

$[HNO_3]$ M	$[Bi(V)]$ 10^{-3} M	
	0 °C	30 °C
0.25	0.04 ± 0.01	0.03 ± 0.01
0.5	0.05 ± 0.01	0.05 ± 0.02
1.0	0.13 ± 0.01	0.16 ± 0.01
2.0	0.17 ± 0.04	0.26 ± 0.03
4.0	0.47 ± 0.05	0.74 ± 0.04

X-ray Absorption Fine Structure at ANL/APS and SSRL

The initial work on examining Am oxidation using XAFS was performed at ANL/APS and showed a difference in edge energy from Am(III), indicative of an increase in oxidation state. The energy of the L_3 edge of Am varies between 18.518 and 18.530 KeV, depending on the oxidation state of the Am ion. The XAFS results shown in Figure 39, reflect a sample that was initially Am(VI) with an excess of solid sodium bismuthate in the bottom of the sample holder. The edge energies for Am(III) and Am(VI) samples were 18.518 KeV and 18.523 KeV, respectively. The Am(III) energy agrees well with similar work found in literature [137, 139].

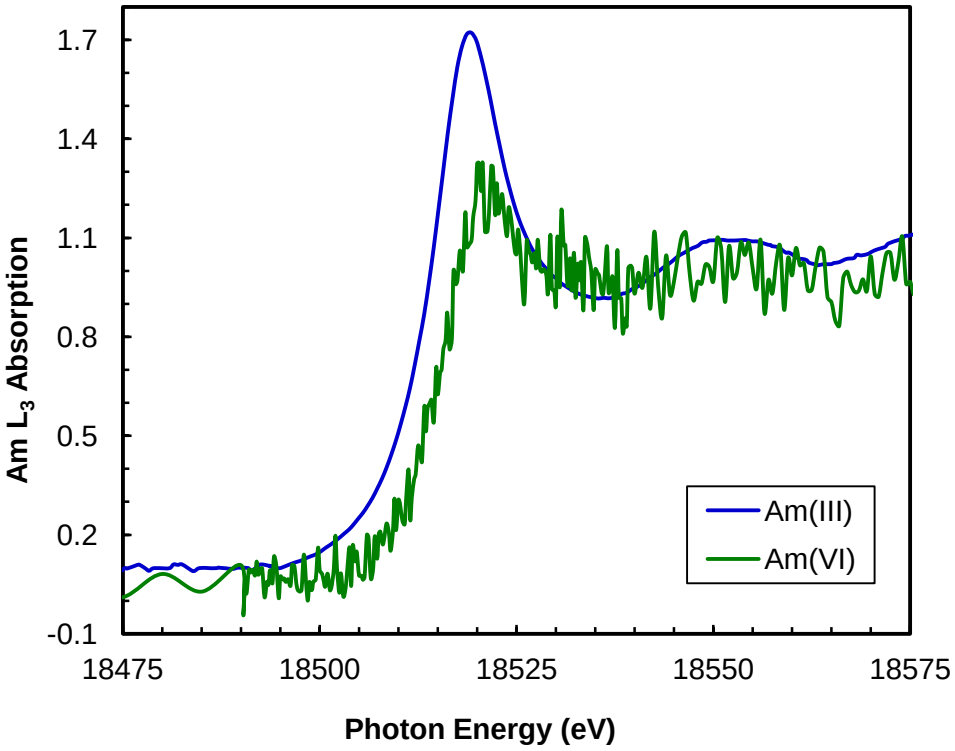

Figure 39 XAFS measurement of Am(III) plotted alongside the Am(VI) with excess sodium bismuthate.

Although the results were not conclusive as to whether the energy shift was Am(V) or Am(VI), the data provides evidence that the solution chemistry using excess sodium bismuthate produces Am higher oxidation states stable enough to be measured. Due to noise in the spectra, no EXAFS results could be obtained, and although an energy shift in the XANES region was seen, it is possible that both Am(V) and Am(VI) oxidation states are present. The background noise in the spectra is attributed to the low concentration of ^{243}Am (0.00 1 M) in the solution. The Am(III) spectral line (Figure 39) shows no background noise and was measured at a substantially higher concentration of ^{243}Am (~0.01 5 M). Refined experiments, based on the XAFS results obtained at

ANL/APS, were designed to minimize the background noise by substantially increasing the ^{243}Am concentration. Another change included an in depth analysis of how acid concentration, sodium bismuthate concentration, and kinetics affect the stability of Am oxidation which was discussed in the UV-Visible results. The results of the XAFS measurements on Am(V) and Am(VI) at SSRL are shown in Figures 40-41. Analysis of an absorption spectrum begins with determination of the absorption edge energy followed by fitting a spline- to approximate the background of the EXAFS region. The oscillation peaks are then extracted and converted to a wave number (Figure 42). A Fourier transform (FT) is then performed to obtain real space data (Figure 41). The real-space data are then analyzed for local structure information, specifically bond distances. The spectral data shows a distinct energy shift of 0.005 KeV from Am(III) at 18.518 KeV to 18.523 KeV for the oxidized Am(VI) sample with excess sodium bismuthate. This difference is significant since a linear correlation between edge energy and formal Am oxidation state was observed in previous work. There was an average increase of about 0.0015 KeV per formal oxidation state when a similar inner coordination environment (O atoms in the first shell) around the absorbing Am atom was maintained [137]. A comparison between the ANL/APS and SSRL experiments showed the substantial increased from 0.001 M to 0.015 M ^{243}Am resolved the noise problem previously experience during the ANL/APS XAFS measurements. The three oxidized sample solutions for measurement included: two Am(V) solutions with no solid sodium bismuthate and Am(VI) with excess solid sodium bismuthate present. Both of the Am(V) samples immediately reduced to Am(III) in the presence of the beam and no spectra of oxidized species was collected.

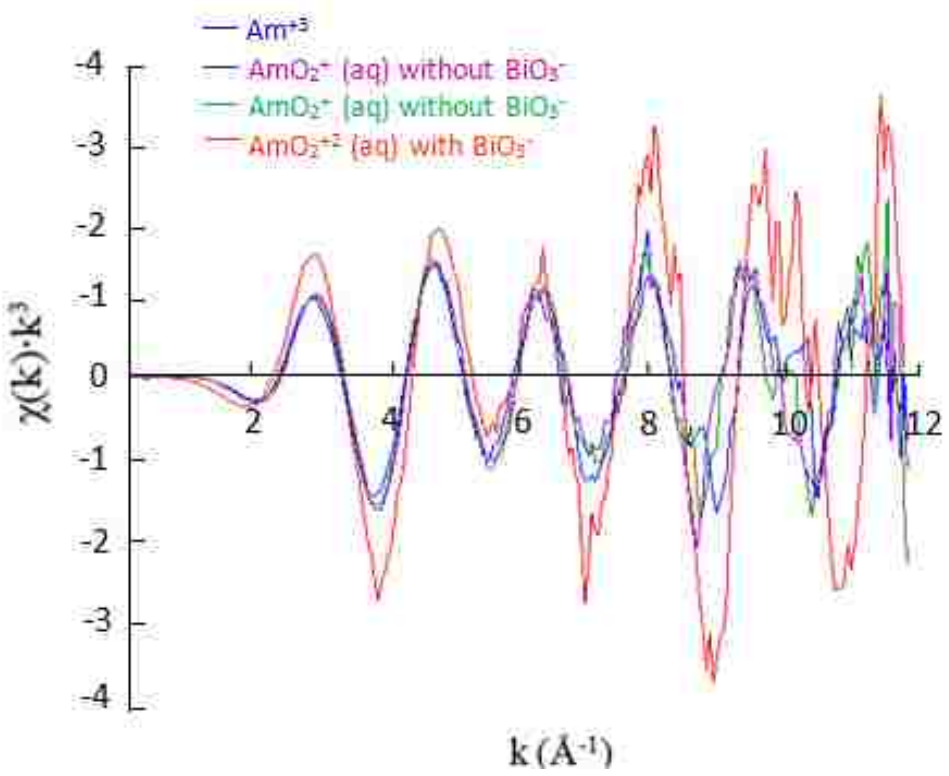

Figure 40 Am(III), Am(V), and Am(VI) EXAFS k space spectra two different solution matrixes with k^3-weighted adjustments.

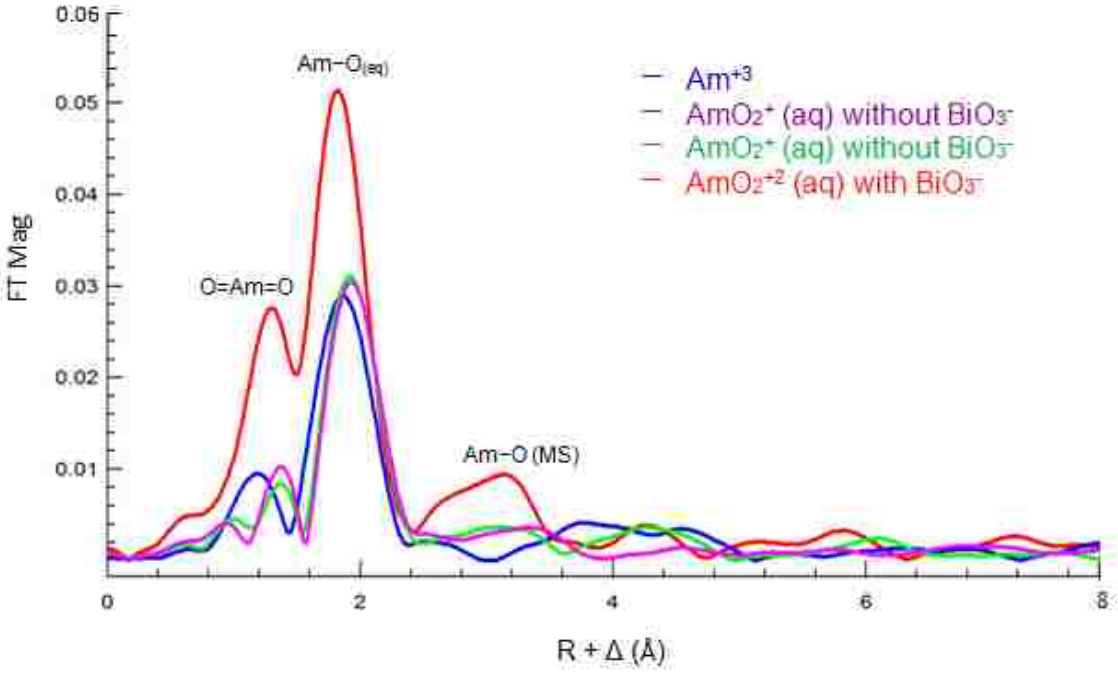

Figure 41 FT of the EXAFS spectra for Am(III), Am(V), and Am(VI) in two different solution matrixes.

However, the Am(VI) sample containing excess sodium bismuthate did not reduce to Am(III) during beam contact and showed a shift to a higher energy indicative of Am oxidation shown in Figure 42. The energy shift between Am(III) and Am(V) or Am(VI) is only a few eV for the SSRL measurement and as much as 5 eV for the ANL/APS measurement. A possible explanation for this measured difference could be the amount of excess sodium bismuthate in each of the different sample solutions. The sample holder for ANL/APS has a lower volume of 0.1 mL than the SSRL, 0.6 mL volume holder, and it is more difficult to judge the amount of excess solid sodium bismuthate that is added to the smaller sample holder versus the larger. The ANL/APS sample holder could have contained a higher level of solid sodium bismuthate present,

which could have also contributed to the large noise level in the spectra, which would have favored the Am(VI) and guarded against reduction to Am(V).

Because the SSRL holders had a larger volume and were easier to view, a more accurate liquid to sodium bismuthate ratio was achieved. This higher accuracy for delivery of the solid sodium bismuthate actually turned out to be a detriment. The SSRL Am(VI) sample was an inseparable mixture of Am(V) and Am(VI) potentially due to a lower concentration of sodium bismuthate. The concentration of sodium bismuthate in the 1 M HNO_3 solution was high enough that the intensity of the beam reduced the Am(VI) to Am(V) and then it was instantaneously re-oxidized to Am(VI). The rate at which this redox behavior occurred did not allow for complete reduction and no Am(III) was present in the spectral data. Unfortunately, the rapid redox behavior of the solution made it impossible to separate the Am(V) from the Am(VI). The XANES edge energy for the SSRL Am(III) and Am(VI) samples were 18518 eV and 18520 eV, respectively (Figure 42). The Am(V/VI) mixture showed an energy shift of 0.002 eV which is lower than the 0.005 eV shift seen for the ANL/APS Am(VI) sample. From literature, the average energy shift between oxidation states is 0.0015 eV which would put Am(V) at approximately 18521 eV and Am(VI) at approximately 18522.5 eV [137]. The XANES data for SSRL shows an energy shift closer to that of Am(V). However, since this is a mixed system of Am(V) and Am(VI) it is difficult to predict whether the mixture of oxidation states is responsible for the reduced energy shift when compared to the ANL/APS sample.

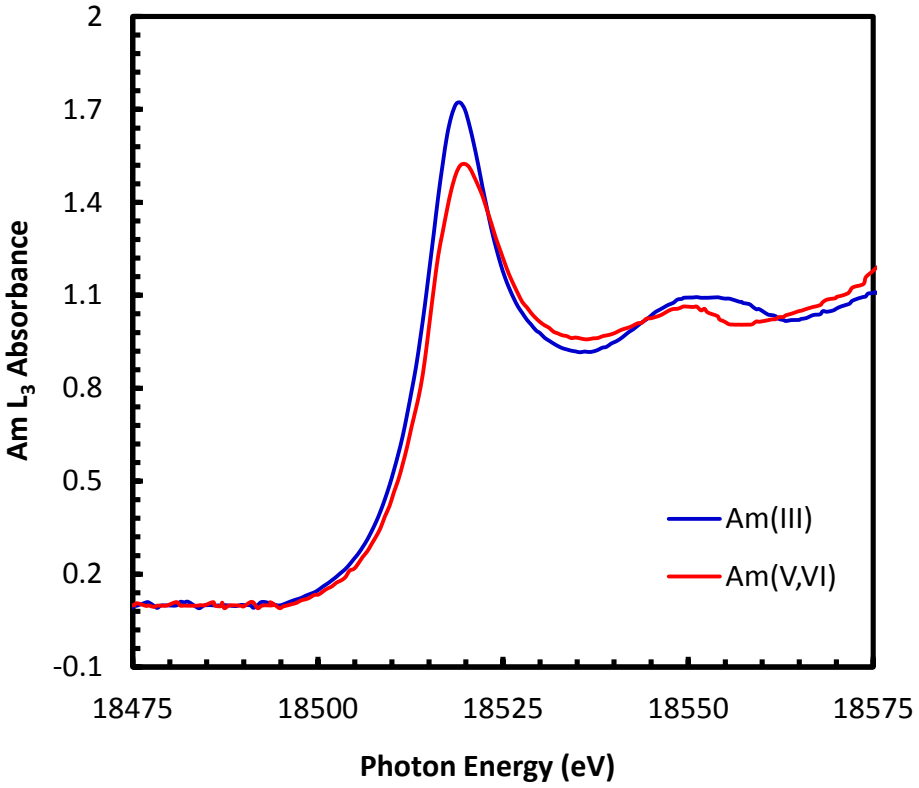

Figure 42 EXAFS and XANES spectra for Am(III) and the inseparable Am(V) and Am(VI) oxidation states from the sample containing excess solid sodium bismuthate.

The Am(V) and Am(VI) form oxo species in solution with a general formula of $AmO_2(H_2O)_n^+$ and $AmO_2(H_2O)_n^{2+}$. The FT of the EXAFS for both AmO_2^+(aq) samples show peaks similar to those of unoxidized Am_2O_3 and are indicative of the reduction that occurred in the beam during the XAFS data collection. However, the AmO_2^{2+}(aq) sample that included the excess solid sodium bismuthate shows two larger peaks indicating two coordination shells. The first peak corresponds to the two axial oxygen atoms, which are located at 1.81 Å from the central Am ion. The second peak corresponds to the equatorial oxygen atoms from the water ligands associated with the low concentration of HNO_3, which are located approximately 2.49 Å from the central Am

ion. Considering the potentially unequal distribution between Am(V) and Am(VI) in the AmO_2^{2+} sample, it is not possible to accurately determine the equatorial coordination of the Am complexes.

The Am species should be analogous to the Pu(V) and Pu(VI) complexes. These show a significantly smaller number of water ligands with longer distances associated with the Pu(V) when compared to the Pu(VI) [142]. For Am(III), the water ligand coordination is between n = 8 or 9 while the AnO_2^{+} tend to have a lower number of water ligands at n = 4 to 5 with longer bond distances, and AnO_2^{2+}, has n = 5 to 6 with shorter bond distances [142]. Figure 43 shows a possible structure for Am(V) or Am(VI) with n = 5 water ligands making it a pentagonal bipyramidal structure. As in the plutonyl, the americyl forms the axis of the bipyramid, and depending on conditions, the geometry may be a tetragonal bipyramid (four ligands in the equatorial plane), a pentagonal bipyramid (five ligands), or a hexagonal bipyramid (six ligands) [142].

The FT also showed a large peak at approximately 3 Å for the AmO_2^{2+} sample which is most likely an artifact of the EXAFS technique and appears when an electron scatters more than once with in a distinct area around the Am [101]. For this reason, multiple scattering (MS) for this sample is included in the data.

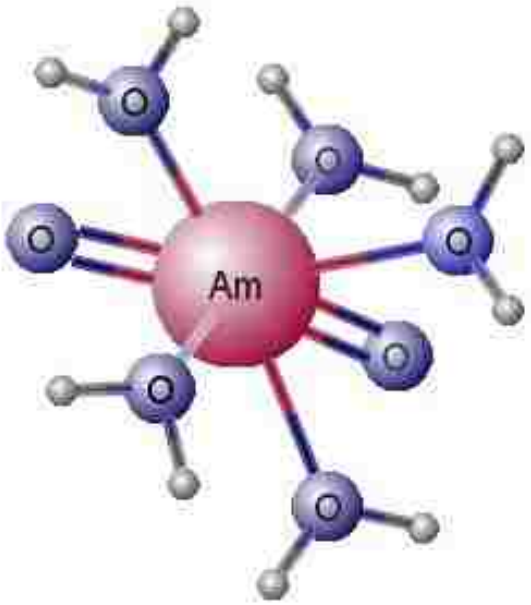

Figure 43 Model of the $AmO_2(H_2O)_n^+$ and $AmO_2(H_2O)_n^{2+}$ in aqueous solution, n =5.

The results with respect to ANL/APS and SSRL are compared in Figure 44. They show the mixture of Am(V) and Am(VI) from the SSRL measurement at a peak energy of 18.518 KeV and a peak energy for the ANL/APS sample 18.523 KeV. It is reasonable to view the ANL/APS spectra as being Am(VI) due to the fact that the known mixture of Am(V) and Am(VI) in the SSRL sample is lower in energy [137]. However, without more accurate EXAFS data it is not possible to verify that the higher energy state is Am(VI) alone. Because there was no EXAFS information available for the ANL/APS experiment, due to low concentration of ^{243}Am in the sample solution, it is not possible to compare bond distances for the Am(VI) with literature which would verify the oxidation state.

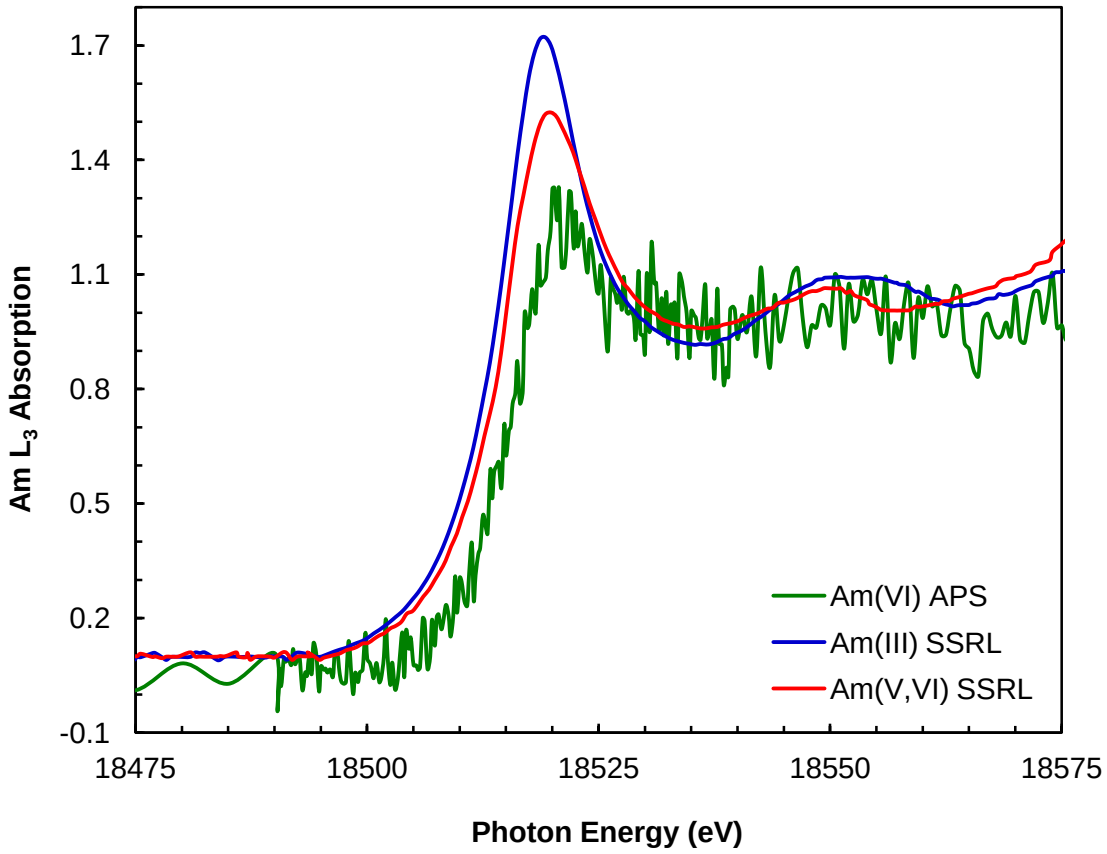

Figure 44 Comparison between Am XAFS spectra for APS and SSRL.

Even though obtaining a clean EXAFS spectrum was not possible there are still interesting conclusions that can be drawn from the results. If sodium bismuthate is to be a viable candidate in oxidation separation systems, it is vital to understand how a mixture of Am(V) and Am(VI) behaves in solution. Considering the redox behavior of Am oxidized with sodium bismuthate, it is reasonable to assume that a mixture of oxidation states will be present as opposed to well defined individual oxidation states in acidic solution. Table 9 shows the parameters extracted from the sample containing ^{243}Am in 1 M HNO_3 with excess solid sodium bismuthate in which a mixture of Am(V/VI) was seen

in the EXAFS measurement. The first peak (R = 1.81 Å) is representative of the R-space distribution attributed to a nearest neighbor shell of the axial oxygen atoms and the second peak (R = 2.49 Å) is due to a shell of the second-nearest equatorial oxygen atoms. The Am–O axial bond distance obtained for Am(V/VI) mixture as well as Am(VI) from literature reported in Table 9, are shorter than the Am(III) oxygen bond distances (R = 2.48 Å). The short axial bond distance is due multiple bond formed between the actinyl oxygens and the metal center for the pentavalent and hexavalent actinides.

Even though the sample solution contains a mixture of Am(V/VI) due to the redox behavior during beam contact, it is probable that there is more Am(V) present since the Am=O axial bonds appear longer than those associated with Am(VI). This theory is justified by comparing the Np = O distance of 1.83 Å observed in EXAFS studies of the NpO_2^+ aquo ion [143]. No bonding data with reference to the sodium bismuthate is predicted since it is a holding agent and does not complex or interact with either the Am or the equatorial oxygen's in solution [12].

Table 9 Parameters extracted from the EXAFS measurements from the SSRL Am sample with excess solid sodium bismuthate.

Shell	Scattering	C.N.	R (Å)	σ^2 (Å^2)	ΔE_0 (eV)
$AmO_2^{+,2+}$	Am– $O_{ax(2)}$	2	1.81	0.0078	8.5
mixture	Am– O_{eq}	5	2.49	0.0091	8.5
	Am– O– $O_{(MS)}$	3.57	3.66	0.0073	8.5
[1]AnO_2^{2+}	An– $O_{ax(2)}$	1.9-2.0	1.74-1.77	0.0010	
	An– O_{eq}	4.4-5.0	2.40-2.42	0.0050	

C.N.: coordination number; R: bond distance; σ^2: Debye-Waller factor squared; ΔE_0: energy shift, ax: axial oxygen, eq: equatorial oxygen; MS= multiple-scattering.

[1] Extended X-ray Absorption Fine Structure literature reported data for $AnO_2(H_2O)_n^{2+}$ (n=5 or 6) in 1 M HNO_3 analogous to Am^{+6} [144, 145].

The culmination of this work centers around the ability to form stable oxidation states for Am(V) and Am(VI), so they can be characterized using methods that were not previously available due to the rapid reduction of these oxidation states in acidic solution. This work has shown that sodium bismuthate forms stable higher Am oxidation states in acidic solution and maintains them even during the rigors of XAFS analysis. The information gained from this work, although not completely conclusive, indicates Am(V) and Am(VI) show similar bonding patterns with the other actinyls and that using sodium bismuthate will produce a higher percentage of Am(VI) over Am(V) in HNO_3 solution.

5.3 Future Work

More extensive research on Am(V) and Am(VI) speciation using sodium bismuthate as the oxidizing agent is necessary. By using higher concentrations of sodium bismuthate in solution there is an increased probability of the Am(VI) stability during XAFS measurements. This can provide further details on whether or not the sodium bismuthate is working as a holding agent or if there is interaction of the metal ion with the sodium bismuthate. Further studies will expand knowledge of these higher oxidation states as it pertains to extraction stability for liquid-liquid extraction systems. Ultimately, a stable Am oxidation system using sodium bismuthate is the goal and in order to support this goal, additional spectroscopy using UV-Visible and XAFS will be needed.

Continuing XAFS measurements to separate Am(V) and Am(VI) oxidation states, whether in solution or solid form, can provide direct information on the speciation of these higher oxidation states giving new insight into their behavior. Lastly, in order to achieve a better separation of these oxidation states, a more optimal oxidation preparation

and analysis method for Am(V) and Am(VI) states must be established. A possible new preparation for XAFS would be to use an Am(V) crystal in place of an Am(V) solution and for Am(VI), use a more concentrated sodium bismuthate solution incorporating $HClO_4$ to increase the sodium bismuthate solubility.

CHAPTER 6

DETERMINATION OF AMERICIUM (V) SINGLE CRYSTAL SYNTHESIS

Binary oxides of the actinides are of particular importance as they provide insight into an element's basic chemical properties including oxidation state stabilities, coordination preferences, and bonding. The 5*f* actinides are known to be very oxophilic and form a wide range of oxide phases. Uranium exhibits the most structural variety in binary oxides, with numerous phases and solid solutions reported having U:O ratios between 1:2 and 1:3 [146]. In an effort to gain further information on Am(V) speciation, a series of crystal synthesis were performed with a variety of compounds designed to use Bi(V) as the oxidizing agent. Uranium was used as a precursor to an Am(V) crystal synthesis with sodium acetate in perchloric acid. Results of all these studies are presented in this chapter. With the information gained through crystallization of an Am(V) species, the role of sodium bismuthate in the oxidation of Am(III) to Am(V) and Am(VI) can be investigated.

6.1 Experimental

Reagents and Radioisotope Solutions

All chemicals were purchased from Sigma-Aldrich and used as received. The sodium bismuthate used was obtained peroxide free from Chemsavers (see Chapter 5). The $HClO_4$ solutions were prepared by volumetric dilution from concentrated acid with an assay of 70%, purified by double distillation. All working solutions were prepared

with HPLC grade nano-pure DI-water in a volumetric flask. Further details on the composition of radioactive and non-radioactive solutions are provided in Table 10.

Table 10 List of working solutions for radioactive and non-radioactive samples. (a) components for the fusion precipitation crystallization of Li_6KBiO_6 and (b) $NaBa_2BiO_6$, (c) components for precipitation crystallization of sodium uranyl and americyl acetate.

Sample Component	Concentration (M)
(a) Li_6KBiO_6	
LiOH	0.42
Bi_2O_3	1.5E-3
KOH	0.18
(b) $NaBa_2BiO_6$	
NaOH	0.25
Ba(OH)	0.030
Bi_2O_3	8E-4
KOH	0.090
$MnCO_3$	0.060
(c) $NaUO_2$[a] and $NaAmO_2$[b] $(OOCCH_3)_3$	
$NaCH_3CO_2$	2.0
^{243}Am[b]	0.005
U[a]	0.020
$NaBiO_3$[b]	0.2
$HClO_4$	0.3

Bi(V) fusion preparation

In an effort to design a crystal structure that would retain Am in the +5 oxidation state, Bi(V) species were investigated. The Li_6KBiO_6 and $NaBa_3BiO_6$, compounds were chosen in the development of an Am(V) crystal [147]. The two compounds were evaluated for use in combination with Am_2O_3 solid in a precipitation from molten

mixtures of alkaline metal hydroxides at 550 ^{o}C. A platinum crucible was used for the alkaline fusion work in a Thermo Scientific muffle furnace (Figure 45).

Figure 45 Thermo Scientific Thermolyne muffle furnace for fusion synthesis of Li_6KBiO_6 and $NaBa_3BiO_6$ crystals.

The Li_6KBiO_6 solid components were combined in proportions, listed in Table 10(a), then mixed slightly and positioned in the center of a platinum crucible. The muffle furnace was preheated to a temperature of 550 ^{o}C and the crucible was inserted. The reagents were heated in the muffle furnace for approximately 24 hours and the furnace was open to ambient atmosphere at all times. For the Li_6KBiO_6, pale yellow-brown, cubic crystals were observed on the sides and bottom of the crucible and any remaining liquid was decanted off after the crucible was removed from the furnace. After the crucible had cooled to room temperature, the crystals were rinsed with methanol to dissolve any remaining hydroxide. The crystals were collected and rinsed again with

methanol and allowed to dry in air for a short period of time before encapsulation in a quartz capillary tube. The procedure for crystallization of $NaBa_3BiO_6$, Table 10(b), was performed in the same fashion as the Li_6KBiO_6. The $NaBa_3BiO_6$ produced emerald green, six sided, needle like crystals.

The next phase following the synthesis of the Bi(V) crystals is to incorporate a surrogate into the Li_6KBiO_6 and/or $NaBa_3BiO_6$ complex. For this phase, manganese(II) in the form of manganese carbonate ($MnCO_3$) was used because it will show an oxidation change to Mn(IV) in the presence of bismuthate. The initial fusion crystal synthesis remained unchanged with the exception of the addition of the $MnCO_3$ to the reagent mixtures (a) and (b). A distinct color change from either the emerald green $NaBa_3BiO_6$ crystal or the pale yellow Li_6KBiO_6 to a transient blue-purple crystal would show surrogate incorporation and oxidation. The $(M)BiO_6 \cdot MnO_2$ crystal, where M= $NaBa_3$ or Li_6K, is a precursor to developing an oxidized Am(V) crystal through this thermal fusion method.

U(VI) acetate crystal preparation

Because of the crystal and chemical similarity between actinide -yl ions, the use of uranyl was chosen as a surrogate for the americyl(V) crystal synthesis. The preparation for a sodium uranyl(VI) acetate as well as the sodium americyl(V) acetate crystals was based on previous work by Asprey, et al. [34]. All work was performed in a radiation hood with HEPA filtration.

The sodium uranyl(VI) acetate ($UO_2(CH_3COO)_2 \cdot 2H_2O$) crystal solution was prepared using concentrations of uranium, U(VI), perchloric acid ($HClO_4$) and sodium

acetate ($NaCH_3CO_2$) as listed in Table 10(c). Sodium acetate is used as a crystal catalyst for the synthesis of uranyl and americyl crystals.

From the uranyl/acetate stock solution, a 0.5 mL aliquot was removed and pipetted into a 10 mL beaker that had been cleaned with HPLC grade D.I. water, rinsed with ethanol and dried in an oven. The beaker containing the sample was placed on an anti-vibration pad to reduce the vibration from the hood motor and fan. The clear solution was allowed to sit undisturbed for 7 days until the solution had reduced in volume to near dryness and crystals of sodium acetate formed. Attached to the clear needles of sodium acetate were bright yellow, tetrahedral crystals. The uranyl crystals were captured in quartz capillary tubes and analyzed under a microscope.

Am(V) acetate crystal preparation

Prior to preparation of the americyl sodium acetate, the ^{243}Am solution had to be converted from 1 M HNO_3 to 0.3 M $HClO_4$. The ^{243}Am (0.009 M) in 1 M HNO_3 was transferred to a TODGA column for processing using the schematic shown in Figure 45. The N,N,N′,N′-tetraoctyldiglycol amide, TODGA, column is used to recover Am(III) from HNO_3 solution. The properties of the TODGA resin allow for the selective separation of Am(III) without breakthrough due to weak retention. The Am(III) is strongly fixed to the TODGA resin in 6 M HNO_3 or HCl and can be eluted from the column with 0.01 M HNO_3 or 0.3 M HCl [148]. The ^{243}Am in 1 M HNO_3 was increased to 6 M HNO_3 for loading onto the TODGA column and was eluted using the procedure shown in Figure 46.

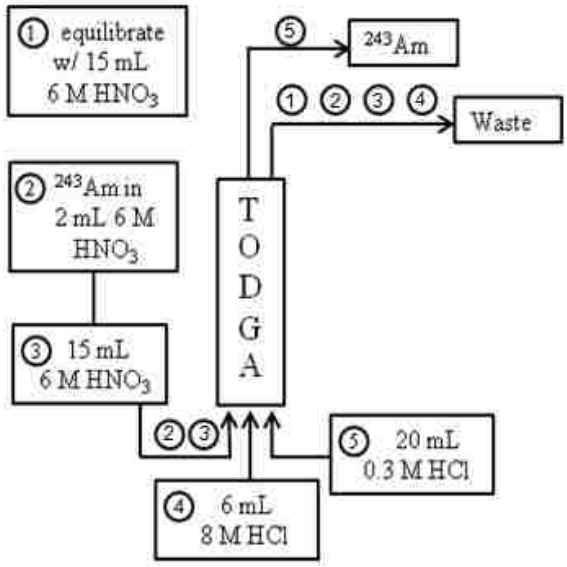

Figure 46 TODGA column schematic for conversion of ^{243}Am in 1 M HNO_3 to 0.3 M $HClO_4$ in preparation of crystal synthesis.

The final product from the TODGA column was ^{243}Am in 0.3 M HCl which was reduced in volume by heating until near dryness. A 10 mL aliquot of HPLC grade D.I. water was added to the ^{243}Am to remove the Cl^- and the volume was reduced again to near dryness. The rinse step was repeated until a near neutral pH was obtained by placing a small drop of solution on litmus paper. The ^{243}Am was brought up to a final volume of 4 mL in HPLC grade D.I. water and acidified to 0.3 M $HClO_4$. Prior to contacting the Am/$HClO_4$ solution with sodium bismuthate UV-Visible spectra was taken to compare the solubility of sodium bismuthate in $HClO_4$ with that of HNO_3 (see Chapter 5). Sodium bismuthate that was contacted for 24 hours with four concentrations of $HClO_4$ and then centrifuged showed the same clear liquid phase, Figure 47, as observed in previous HNO_3 samples. Sodium bismuthate is more soluble in $HClO_4$ than in HNO_3, [10, 11] so the use of $HClO_4$ as the acidic media for the crystal synthesis will increase the

amount of bismuthate in solution and better stabilize the Am in higher oxidation states as it crystallizes.

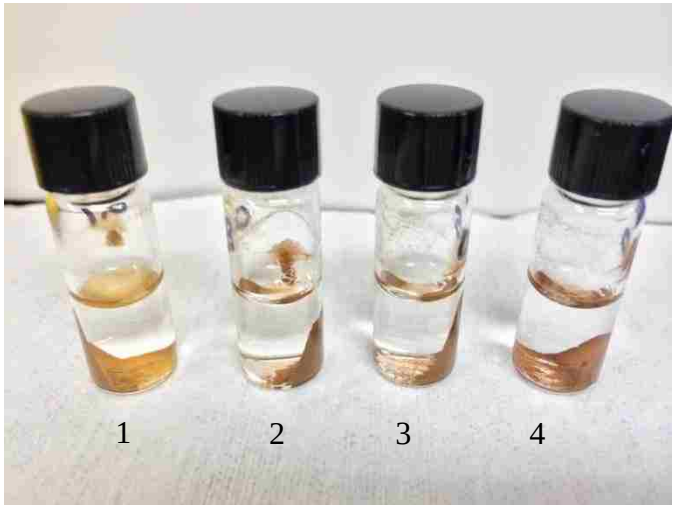

Figure 47 Excess sodium bismuthate in $HClO_4$ concentrations of: (1) 0.1 M, (2) 0.3 M, (3) 0.5 M, (4) 1.0 M. The liquid phase shows no coloration from the sodium bismuthate, however, the solid sodium bismuthate in concentrations above the 0.1 M $HClO_4$ has taken on a darker shade.

The initial crystal stock solution was prepared from the Am in 0.3 M $HClO_4$ solution by removing 1 mL and diluting the Am concentration from 0.009 M to 0.005 M. Perchloric acid was added to increase the acidity back to 0.3 M and 60 mg of sodium bismuthate was added (Table 10(c)). The Am/acetate/bismuthate solution was shaken for 2 hours and the liquid/solid phases were allowed to separate. The Am(III) in solution had been oxidized to Am(VI) via the excess sodium bismuthate. The solid and liquid phases were left in contact, without further shaking, for 24 hours. The sample was centrifuged and the liquid phase separated from the solid bismuthate phase.

The Am(VI) in solution had completely reduced to Am(V) and the sodium americyl(V) acetate solution exhibited a pale yellow color indicative of the Am(V) oxidation state. A 0.5 mL aliquot of this solution was pipetted into a 10 mL beaker and the same procedure used for the production of the sodium uranyl(VI) acetate crystals was applied. A secondary containment enclosure, constructed inside the rad hood and shown in Figure 48, was used for the Am crystallization due to the high levels of alpha emitters involved. Clear crystals of sodium acetate formed as they had for the uranyl acetate and were followed by pale yellow tetrahedral crystal formations attached to the acetate crystals.

Figure 48 Secondary containment disposable glove box for sodium americyl(V) acetate crystal synthesis set inside a radiation hood.

6.2 Results and Discussion

Bismuth(V) fusion crystallization

Initial results for both Li_3KBiO_6 (Figure 49) and $NaBa_3BiO_6$ (Figure 50) showed promise as both reproducible and stable crystals were synthesized in large yields. The main advantage of these two crystal types is the retention of the Bi(V) oxidation state during the fusion process and as the product. By incorporating Am_2O_3 into the fusion reagent mixture it is theorized that the Am(III) would be oxidized to Am(VI) by the Bi(V) and ultimately reduce to the stable Am(V) during the 24 hour period of crystal formation. Without excess bismuthate present Am(VI) will reduce to Am(V), as discussed in Chapter 5, and this would allow the Am(V) to be retained in the crystal structures.

Figure 49 Pale yellow, cubic crystals of Li_3KBiO_6 which retain the Bi(V) oxidation state.

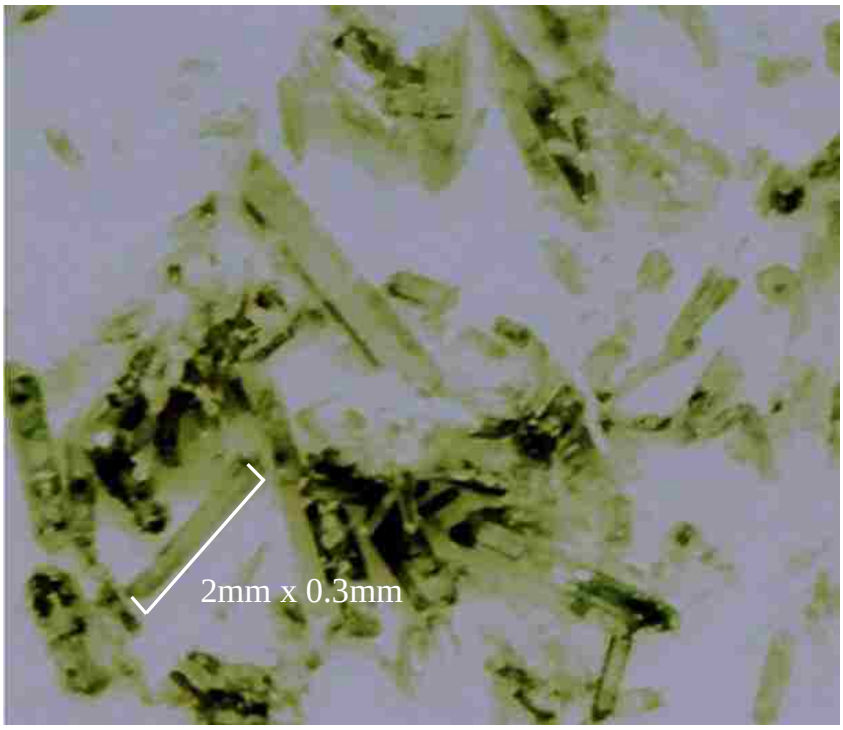

Figure 50 Emerald green, six sided needles of $NaBa_3BiO_6$. Like the crystal in Figure 49, this crystal also retains bismuth in the Bi(V) oxidation state.

Both crystal compounds, Li_3KBiO_6 and $NaBa_3BiO_6$, had a high probability of success owing to not only the Bi(V) present in both compounds, but also the Li and Ba components, respectively. All Am(VI) compounds are complex salts containing oxygen such as Li_6AmO_6, $NaAmO_2Ac_3$ (Ac is acetate ion), AmO_2F_2 and Ba_3AmO_6 [53]. All pentavalent Am compounds are complex salts such as $KAmO_2CO_3$, $KAmO_2F_2$ and Li_3AmO_4 [74, 149]. Of these compounds, the single crystal produced by the $NaAmO_2Ac_3$ is the only characterized complex of the americyl(VI). The americyl(V) crystal has not been produced or characterized [74].

Initial studies using Li_3KBiO_6 yielded no crystals when the MnO surrogate was introduced into the reagent system. The resulting liquid retrieved after 21 hours was dark

brown in color and no crystals had been produced in the crucible. Several variables were altered including concentration of reagents, temperature, and duration in the furnace, however, the results remained unchanged. The $NaBa_3BiO_6$ matrix showed promise with the incorporation of the MnO surrogate, Figure 51, in concentrations ranges shown in Table 10(b). The crystals produced were no longer emerald green and under the microscope the distribution of the blue-purple color was homogeneous throughout the crystal. The $NaBi_3BiO_6 \cdot MnO_2$ crystal retained the hexagonal needle appearance of the parent crystal and the color change was indicative of not only the inclusion of the Mn surrogate, but also an oxidation change from Mn(II) to Mn(IV). The SEM analysis was performed on the $NaBi_3BiO_6 \cdot MnO_2$ single crystal and the results are shown in Figures 52-58.

Figure 51 The $NaBa_3BiO_6 \cdot MnO$ fusion produced blue-purple hexagonal needles with dimensions of ~0.5 – 1.0 mm on edge.

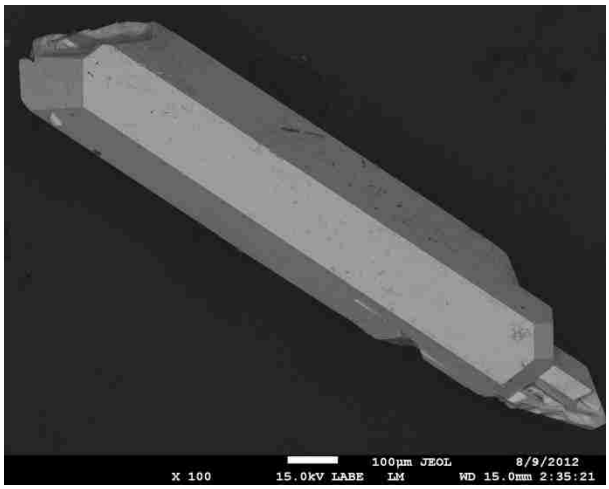

Figure 52 Baseline SEM of a $NaBa_3BiO_6$ crystal with Bi in the +5 oxidation state.

The $NaBa_3BiO_6$ crystal was analyzed by SEM forming a baseline for comparison analysis with surrogate incorporated crystals of the same base compound. The analysis of the $NaBi_3BiO_6 \cdot MnO_2$ crystal using SEM spectroscopy showed the Mn surrogate was attached only to the surface of the $NaBi_3BiO_6$ and was not incorporated into the crystal structure itself, Figure 53. The line spectrum from the SEM and single crystal XRD analysis confirmed that Mn was not homogeneously incorporated into the crystal structure, but had fused to the outside layer of the parent crystal. The Mn was wide spread across the surface of the crystal which caused an internal reflection of the blue-purple hue throughout the crystal.

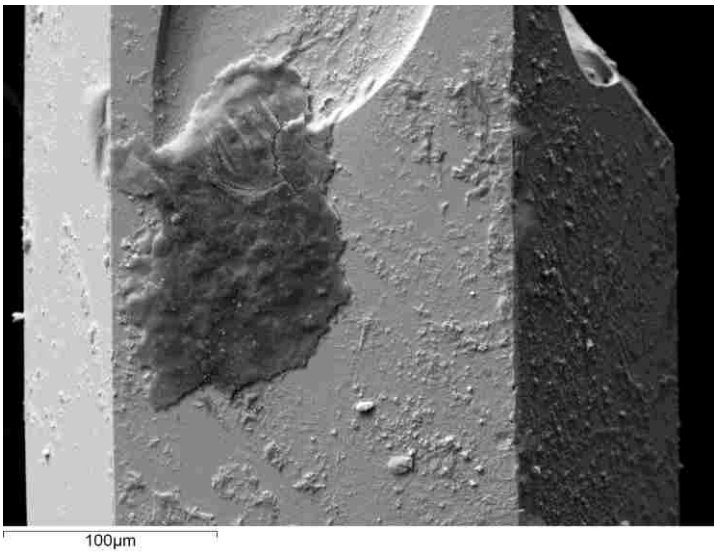

Figure 53 $NaBa_3BiO_6$ parent crystal with the MnO_2 surrogate fused to the surface.

The SEM analysis was also used to verify that the fused substance attached to the $NaBa_3BiO_6$ crystal was the Mn surrogate and not a contaminant, such as residual hydroxides. Results of the SEM analysis are presented in Figures 54 and 55. Line spectrum 1 is a representative area of the crystal surface, pictured in Figure 55, which was analyzed for all elements present in the crystal. The spectrum showed a small amount of residual potassium (K) from KOH in the initial reagent mixture that was not completely removed in the rinse step along with Ba, Bi, and a small amount of the Mn taken from the darkest section of line spectrum 1. The K found in the sample is due to the addition of KOH used to improve the quality of the crystals and was attached to the surface only. In the absence of KOH, the $NaBa_3BiO_6$ crystals had a lower yield, were substantially smaller in size, and not as well formed.

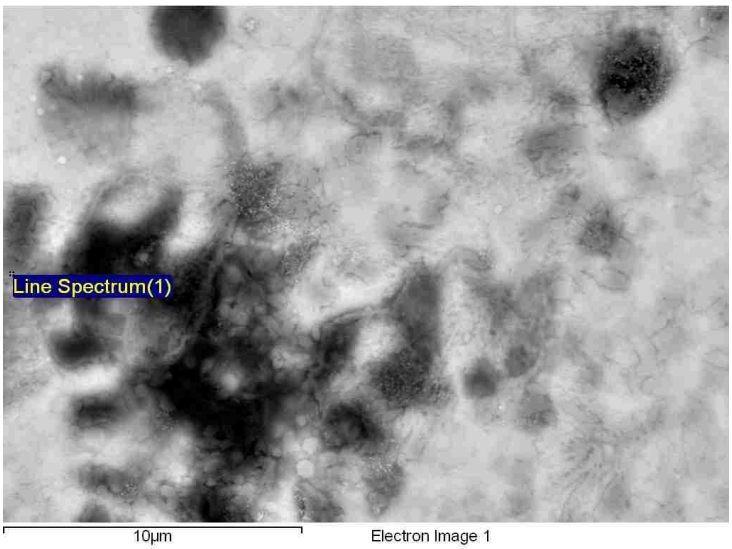

Figure 54 SEM image of a $NaBa_3BiO_6$ crystal and MnO_2 attached to on surface. This is an enhanced section from the dark fused section of Figure 55.

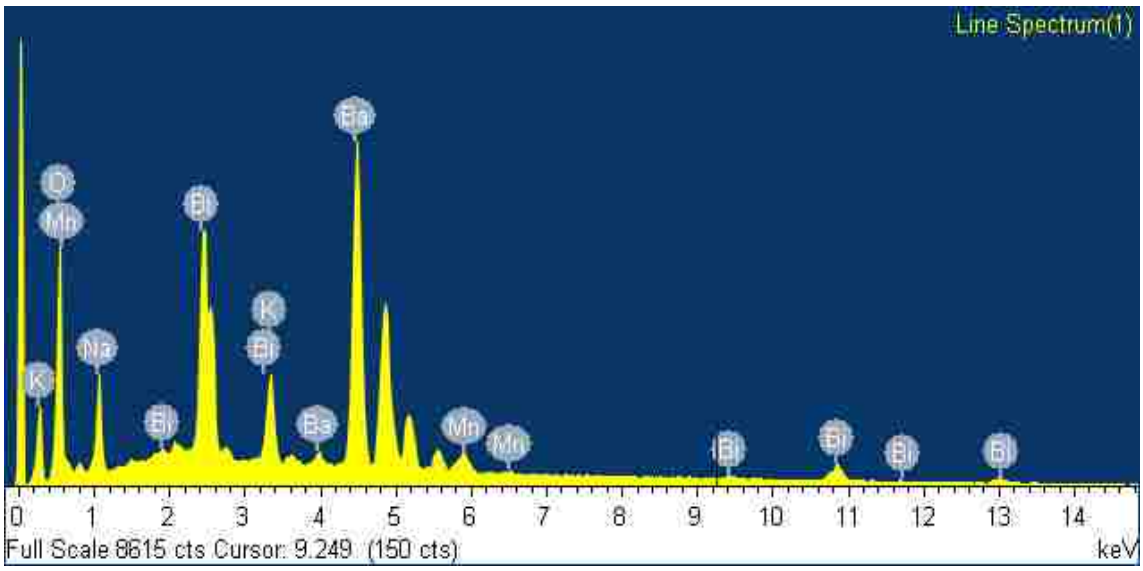

Figure 55 SEM spectrum showing the presence of Mn in the $NaBa_3BiO_6 \cdot MnO_2$ crystal compound. This is an analysis of the Line Spectrum (1) area from Figure 56.

The $NaBa_3BiO_6$ crystals are hygroscopic and thus air sensitive as seen in Figure 56. The crystals had been sputter coated and were kept in an inert argon atmosphere. However, due to equipment maintenance the crystals were removed for 20 minutes from the argon and decomposed before they could be returned to the chamber. The oxide 'coral' grew quickly and is likely due to the residual KOH and other hydroxide compounds associated with the synthesis of these crystals interacting with the moisture in the air.

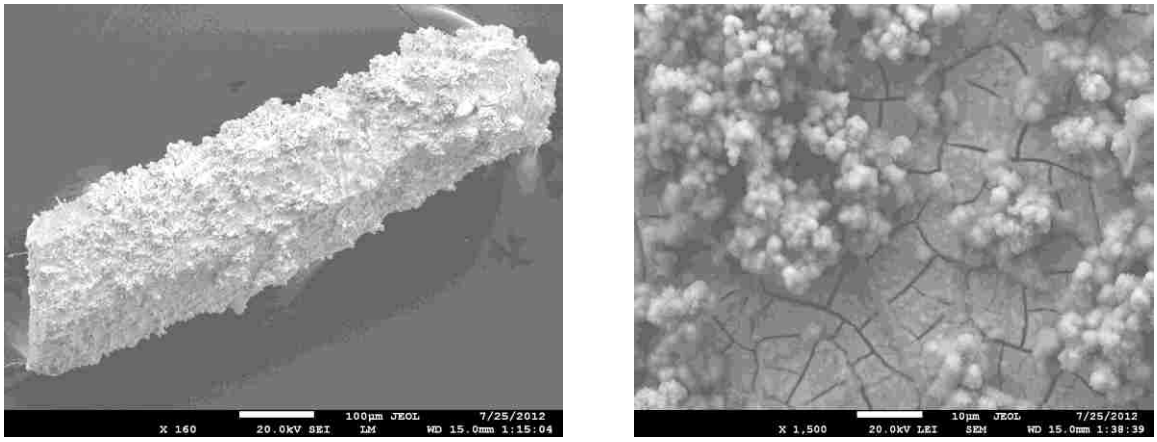

Figure 56 SEM image of air oxidation of $NaBa_3BiO_6 \cdot MnO_2$ crystal (100*u*m, x160 resolution) and the surface of the same crystal at 10*u*m and x1,500 resolution.

The XRD data for the $NaBa_3BiO_6 \cdot MnO_2$ crystal, shown in Figure 57 and Table 11, shows the same results as the SEM as far as the Mn surrogate fusion to the surface of the crystal face. The single crystal XRD analysis verified the crystal structure was composed of the original $NaBa_3BiO_6$ crystal with no sign of the Mn found in the analysis reported in Table 11.

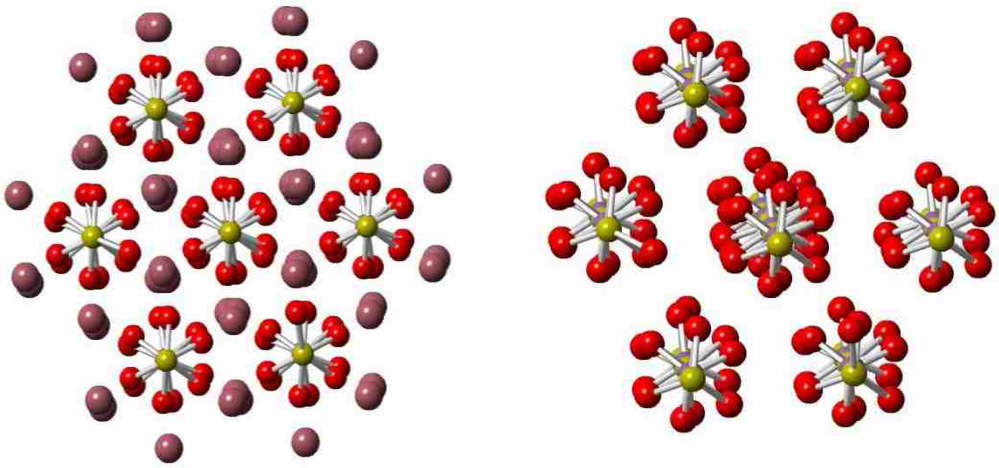

(a) (b)

Figure 57 Packing diagram as viewed down the 111 (3-fold) axis of the rhombohedral cell for the $NaBa_3BiO_6 \cdot MnO_2$ crystal. (a) includes Ba= ● and (b) with Ba excluded, shows the in line structure between Bi= ● and Na= ●. No Mn is present in the crystal structure and only the original $NaBa_3BiO_6$ structure is seen.

Table 11 Atomic coordinates (1×10^4) and equivalent isotropic displacement parameters ($Å^2 \times 10^3$) for APX1629a. U(eq) is defined as one third of the trace of the orthogonalized U^{ij} tensor.

	x	y	z	U(eq)
Bi(1)	0	0	0	0(1)
Ba(1)	3981(1)	1019(1)	7500	2(1)
Na(1)	2500	2500	2500	2(1)
O(1)	821(4)	2785(4)	9475(4)	5(1)

The results of the crystal analysis matched those found in the literature [147]. Figure 58 shows the bonding characteristics of the $NaBiO_6^{6-}$ in the $NaBa_3BiO_6$ crystal as an isolated chain of the crystal structure. The structure can be described in terms of parallel chains

of alternating Bi and Na atoms, with the metal atoms connected to each other by three bridging oxygen atoms. The $NaBiO_6^{6-}$ chains extend along the three-fold axis of the rhombohedral unit cell and are packed in a hexagonal array. The Ba atoms are located between these chains and the bismuth atoms are located at the corners and center of the unit cell. Six oxygen atoms are coordinated in an octahedral array around each bismuth atom at a distance of 2.109(2) Å [147]. Selected bond distances for the $NaBa_3BiO_6$ crystal are shown in Table 12. Ultimately, it was not possible to incorporate any surrogates into the $NaBa_3BiO_6$ crystal matrix and a new route for crystal synthesis was pursued.

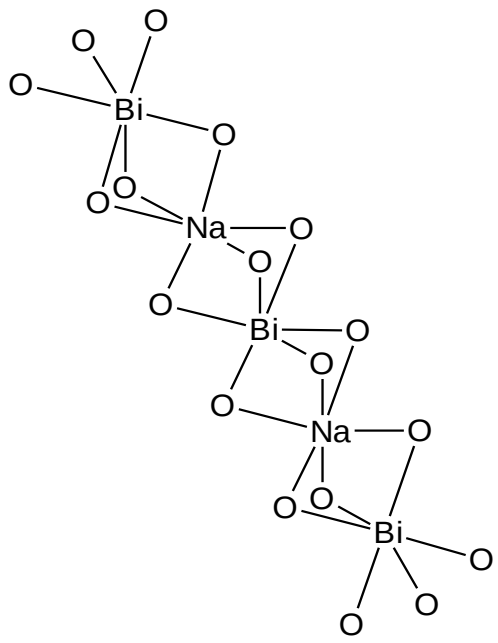

Figure 58 Structure of $NaBiO_6^{6-}$ in the $NaBa_3BiO_6$ chain. For the purpose of this discussion, Ba has been omitted since the focus of this work centers on the Bi(V).

Table 12 Bond distances for $NaBa_3BiO_6$ [147]

Scattering	Bond dist.(Å)	esd
Bi-O(6)	2.109	0.002
Na-O(6)	2.485	0.002
Ba-O(2)	2.658	0.002
Ba-O(2)	2.788	0.002
Ba-O(2)	2.827	0.002
Ba-O(2)	3.026	0.002

esd: experimental standard deviation

U(VI) and Am(V) acetate slow evaporation crystallization

Initial results using sodium acetate as a crystal growth medium were successful, producing several sodium uranyl(VI) acetate crystals. From previous crystallographic results [34], it has been shown that uranyl, neptunyl, plutonyl, and americyl ions are analogous to each other and using sodium acetate it is possible to produce crystals of each. Figure 58 shows sodium acetate crystals that were produced in the absence of a metal.

Figure 59 Sodium acetate crystals needles on which both the uranyl and americyl acetate crystals were grown.

Slow evaporation from a uranium solution dissolve in 0.3 M $HClO_4$ produced multiple crystals. However, what seemed to be a collection of single crystals at first glance turned out to be both single crystals and two or more individual crystals in slight misalignment. Both a multiple-misaligned crystal, right side, and a single crystal, left side, can be seen in Figure 60 attached to an acetate crystal. A well shaped single crystal is also seen in Figure 61 attached to acetate. A small green filiment that landed in the open beaker during the crystalization can be seen in Figure 60 with a multi uranyl acetate crystal entwined. The filiment may or may not have acted upon the uranyl acetate crystal to produce multiple crystals since previous work has shown the production of multiple crystals without impedance from foreign objects [150, 151].

Figure 60 Close up showing the signature tetrahedral structure and yellow color of a cluster of sodium uranyl(VI) acetate crystal attached to sodium acetate crystals.

Figure 61 Sodium uranyl(VI) acetate single crystal growing on a sodium acetate crystal needle.

Each uranyl is complexed with six oxygen atoms from three acetate ions, giving the uranium atom a hexagonal-bipyramidal coordination which is common place for uranyl

salts [150]. This crystal has 4 elemental species distributed over 8 crystallographic positions. Two of the oxygen sites are the U-O double bonded oxygen's with a distance of about 1.71 Å. The remaining oxygen sites are single bonded at a distance of about 2.49 Å. Figure 62 shows a representation of the sodium uranyl(VI) acetate crystal structure and Table 13 lists the accompanying bond distances for the structure.

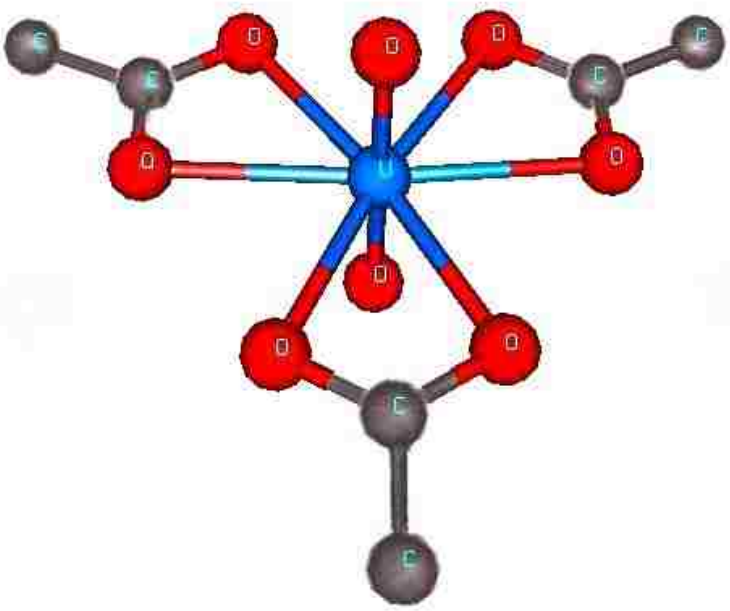

Figure 62 Sodium uranyl(VI) acetate structure. The hydrogen's have been omitted for clarity. The uranyl(VI) is analogous to the americyl(VI) acetate crystal structure.

Table 13 Bond distances and angles for the sodium uranyl(VI) triacetate crystal [150].

Scattering	R(Å)
U–1 O(1)	1.72 ±0.04
U–1 O(2)	1.70 ±0.04
U–3 O(3)	2.47 ±0.02
U–3 O(4)	2.51 ±0.02
C –1 C(2)	1.52 ±0.05
C –1 O(3)	1.26 ±0.05
C –1 C(4)	1.28 ±0.04
Na–3 O(3)	2.39 ±0.04
Na–3 O(4)	2.36 ±0.04
C(2) –1 C(1)	1.52 ±0.04
C(2) –1 H(1)	(0.8)
C(2) –1 H(2)	(1.5)
C(2) –1 H(3)	(1.1)

Scattering	Bond angles (deg.)
O(1)–U–O(2)	180
O(1)–U–O3)	90.12
O(1)–U–O(4)	90.48
O(3)–U–O(4)	52.24
O(3)–C(1)–O(4)	118.9
O(3)–C(1)–C(2)	120.4
O(4)–C(1)–C(2)	120.7
U–C(1)–C(2)	176.8

By studying the sodium uranyl(VI) acetate single crystal synthesis, an accurate experimental process for the synthesis of a sodium americyl(V) acetate crystal was produced. Structural details on compounds of pentavalent Am remain rare and only a few structures are published. Reported structures of inorganic Am(V) compounds exhibit two-dimensional layered arrangements governed by the most prominent structural feature, the linear americyl trans-dioxo $O=Am=O^{+}$ moiety [137]. X-ray diffraction patterns for the Am(VI) revealed a hexagonal bipyramidal structure with a lattice constant a_o = 10.6 Å**,** the same as that of the uranyl, neptunyl and plutonyl analogs [34]. It is expected that the Am(V) crystal structure will fall in between the Am(III), with an a_o = 5.4 Å, and Am(VI) with a theoretical lattice constant of a_o=9.9 Å [141].

The proposed sodium americyl(V) acetate crystal structure is shown in Figure 63 along with the isotropic tetrahedral shape of the structure. The americyl(V) acetate

crystal has the same structural components associated with those of uranyl, neptunyl, and plutonyl with the oxidation state being dependant on the oxidizer used. The sodium americyl(VI) acetate crystal produced by Asprey et al [34] used peroxydisulfate as oxidizing agent, which assured an Am(VI) oxidation state devoid of Am(III) and Am(V). Sodium bismuthate has been shown to produce Am(V) in solution without the presence of Am(III) or Am(VI) over time, as explained in Chapter 5, and would thus produce an Am(V) crystal in the same fashion as reported by Asprey et al [34].

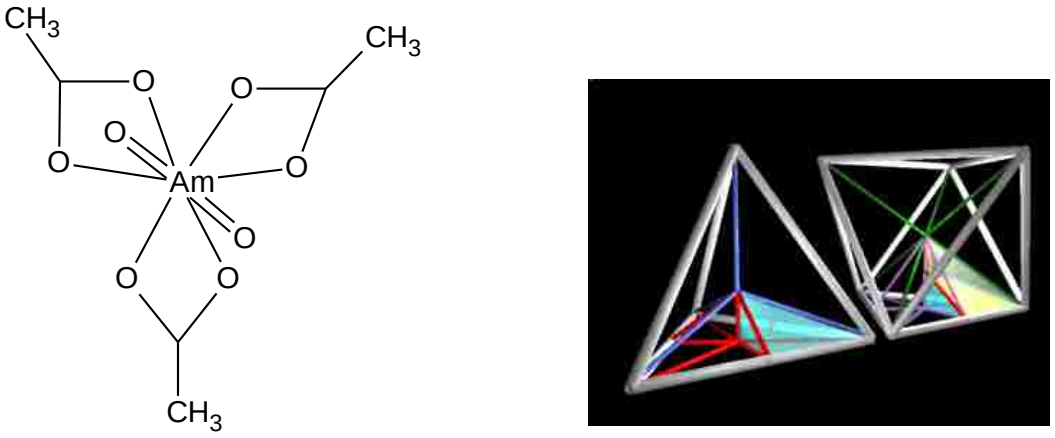

(a) (b)

Figure 63 (a) Sodium americyl(V) acetate crystal structure ($NaAmO_2(OOCCH_3)_3$). (b) Projected isotropic tetrahedral crystal structure of sodium americyl(V) acetate.

The sodium americyl(V) acetate crystals shown in Figure 64 where produced in the same manner as the uranyl(VI) crystals with the exception of contacting the ^{243}Am and sodium acetate/0.3 M $HClO_4$ solution with excess sodium bismuthate. The resulting

sodium americyl(V) acetate crystals were similar in size and shape to the sodium uranyl(VI) acetate crystals and the growth time for the crystals was the same at ~7 days. As with many other actinides, self-damage of the crystal lattice due to alpha-particle irradiation is common to Am. At ambient conditions, Am is present in its most stable alpha (α) form which has a hexagonal crystal symmetry, and a space group $P6_3/mmc$ with lattice parameters a = 346.8 pm and c = 1124 pm, and four atoms per unit cell. The crystal consists of a double-hexagonal close packing with the layer sequence ABAC and so is isotypic with α-lanthanum and several actinides such as α-curium [152].

Figure 64 Sodium americyl(V) acetate crystals (yellow) attached to sodium acetate needle like crystals (clear/white). Crystals appeared shortly after the formation of the clear acetate crystals and as the acetate crystal became more opaque, the americyl(V) acetate crystal began to form.

Due to decomposition of the sodium americyl(V) acetate crystal, Figure 65, no diffractometry was possible. However, the Am(V) acetate crystal should be closely aligned to the Np(V) acetate crystal. The Np(V) acetate crystal has six oxygen atoms belonging to three acetate ions that fill the equatorial region of the neptunyl ion, giving the Np atom a hexagonal- bipyramidal coordination overall. The six equatorial O atoms lie very nearly in a plane; none deviates from the best least-squares plane by more than 0.032 Å and the linear NpO_2^+ portion is perpendicular to this plane within [153]. While the point symmetry at the Np atom in the crystal is actually C_2 the entire $[NpO_2(CH_3CO_2)_3]^{2-}$ bipyramid has nearly D_{3h} symmetry.

There are two independent acetate ions in the asymmetric unit of structure. One has its C atoms on a twofold axis and is thus strictly planar while the other is nearly planar with the methyl C atom a little out of the plane of the carboxyl atoms [153]. It is likely the sodium americyl(V) acetate would have a very similar configuration to the uranyl(VI), neptunyl(V), and plutonyl(VI) acetate crystals.

Figure 65 Sodium americyl(V) acetate crystals decomposed

Although no XRD analysis of the Am(V) crystals was not possible in this instance, the ability to synthesize oxidized americyl crystals using sodium bismuthate was shown. Based on the stability of Am(V) over time in the absence of excess solid sodium bismuthate as well as the visual color change indicative of Am(V) from literature, [74], it is expected the composition of these crystals is sodium americyl(V) acetate. Ultimately what has been established by this work is a procedure by which future crystals of Am(V), as well as Am(VI), can be synthesized using sodium bismuthate for stable Am oxidation states.

6.3 Future Work

Further research and analysis of the bismuthate oxidized sodium americyl(V) acetate crystal structure is necessary. By reproducing the Am(V) acetate crystal an in-depth analysis using single crystal XRD will be possible. This analysis can provide further details on whether or not the sodium americyl(V) acetate crystal has incorporated the sodium bismuthate, or if it continues to act simply as a holding agent without becoming part of the crystal structure. Continued studies with respect to the americyl(V) acetate crystal could ultimately yield a way to study the Am(V) oxidation state using XAFS without the associated problems seen in solution phase. Further investigations on the stability of the americyl(V) acetate crystal are also needed in order to determine the extent of radiolysis on the decomposition of the product. This information will be very important for both XRD analysis as well as analysis using XAFS. An Am(V) crystal will provide information the that could not be gained using oxidized Am in solution for this oxidation state.

CHAPTER 7

CHARACTERIZATION OF AMERICIUM (V) AND (VI) MOLECULAR COMPLEXES WITH COMPUTATIONAL CHEMISTRY

The actinides are characterized by a gradual filling of the 5*f*-electron shell with the degree of localization increasing with the atomic number Z along the last series of the periodic table. The open shell of the 5*f* electrons determines the magnetic and solid-state properties of the actinide elements and compounds. Understanding the quantum mechanics of the 5*f* electrons is an important issue in actinide chemistry. Although there are considerable first-principles results available for U, Pu, and Np molecular complexes and compounds, there is little information published on Am structures with oxidation states higher than trivalent. In previous computational studies of Am-bearing molecular complexes, the outer 17 electrons ($6s^2\ 6p^6\ 5f^6\ 6d^1\ 7s^2$) of Am are generally treated as valence electrons while the remaining 78 electrons are treated as core electrons. There is variety of computational methods the range in sophistication from the second-order Moller-Plesset (MP2) approach all the to density functional theory (DFT) [154]. Representative computational studies of americyl and Am aquo complexes have been performed in previous work [143, 155-158].

In this study, DFT was used to carry out all total-energy calculations. Density Functional Theory is a first-principles approach that focuses conceptually upon the electronic density $\rho(r)$ rather than upon an N-electron wave function. Density Functional Theory is an alternative to *ab initio* methods for computational treatments of chemical systems and processes [159]. In an effort to gain further information on the Am(V/VI)

mixture observed in EXAFS experiments, DFT was used to model the $AmO_2^{+/2+}$ and $AmO_2(H_2O)_5^{+/2+}$ complexes. All-electron scalar relativistic calculations of the total energies, optimized geometries, and molecular properties were performed using spin-polarized DFT. Details of the DFT methodology used and the results for Am(V) and Am(VI) complexes are presented in this chapter.

7.1 Computational Methods

Total-energy, all-electron scalar relativistic calculations were performed to determine the ground-state geometries and properties of the $AmO_2^{+/2+}$ and $AmO_2(H_2O)_5^{+/2+}$ complexes using spin-polarized DFT as implemented in the DMol^3 software [160, 161]. The Dmol^3 is a modeling program that uses DFT to optimize geometries and simulate chemical processes and accurately predict properties of molecules and materials [162]. The Dmol^3 is based on the Kohn-Sham approach, in which the electronic density is written as a sum of one-electron orbitals, equation 7-1. The constrained minimization of total energy from equation 7-1 leads to equations 7-2 and 7-3, where the effective potential is υ_{eff} and ε_i is the Lagrange multiplier, respectively.

$$\rho(\mathbf{r}) = \sum_{i=1}^{N} |\phi_i|^2 \qquad \text{(Eq. 7-1)}$$

$$\left[-\frac{\nabla_i^2}{2} + \nu_{\text{eff}}(\mathbf{r}_i)\right]\phi_i = \varepsilon_i \phi_i \qquad i = 1, 2, \ldots, N \qquad \text{(Eq. 7-2)}$$

$$\nu_{\text{eff}}(\mathbf{r}_i) = -\sum_A \frac{Z_A}{|\mathbf{R}_A - \mathbf{r}_i|} + \int \frac{\rho(\mathbf{r})}{|\mathbf{r} - \mathbf{r}_i|}\, d\mathbf{r} + \varepsilon_{xc}(\rho) + \rho(\mathbf{r})\frac{\delta \varepsilon_{xc}}{\delta \rho} \qquad \text{(Eq. 7-3)}$$

The exchange correlation energy was calculated using the generalized gradient approximations (GGA) [163] with the parameterization of Perdew and Wang (PW91). The local density approximation (LDA) [164] was also tested with the parameterization of Perdew and Wang (PWC). The GGA functionals, such as PW91 or PBE, are generally preferred over hybrid functionals which do not appear to describe bonds as accurately in actinide-bearing molecular systems [165]. Double numerical basis sets including polarization functions on all atoms (DNP) were used in the calculations for this work. The DNP basis set corresponds approximately to a double-ζ quality basis set with a p-type polarization function added to hydrogen and d-type polarization functions added to heavier atoms. The DNP basis set is comparable to 6-31G** Gaussian basis sets but with superior accuracy for a basis set of comparable [35, 166]. In the generation of the numerical basis sets, a global orbital cutoff of 5.9 Å was used.

The energy tolerance in the self-consistent field calculations was set to 10^{-6} Hartree. The molecular geometries of the well-know uranyl complexes were chosen as initial guesses for the present structural relaxation calculations. Optimized geometries were obtained without symmetry constraints using the direct inversion in a subspace method (DIIS) with an energy convergence tolerance of 10^{-5} Hartree and a gradient convergence of 2×10^{-3} Hartree/Å. The charge density was expressed by a nucleus-centered multipole expansion truncated at the octupole level. The spin-orbit coupling was neglected for the Am(V/VI) calculations. This computational approach has shown previously to yield accurate structural results for uranium compounds [154, 167, 168] and uranium-bearing complexes [169, 170].

7.2 Results and Discussion

Density Functional Theory was used to evaluate structural data produced from EXAFS data in an effort to model the solution structures of the Am(V/VI) oxidation states. Since little DFT information on Am(V) and Am(VI) is available, comparisons with other actinyl species are used to evaluate the DFT models created using the Am(V/VI) EAXFS data. The predominant form of the +5 and +6 oxidation states of the actinides at low pH are the penta-aqua species $AnO_2(H_2O)_5^{+}$ and $AnO_2(H_2O)_5^{2+}$, respectively. Higher Am oxidation states are comparable to those of U, Np, and Pu with the solution EXAFS measurements and corresponding DFT results for these actinyls having been published [143]. The closed shell $UO_2(H_2O)_5^{2+}$ is indicative of other molecules in this series and adopts the linear O=U=O group with coordinating water molecules bound in the equatorial plane of the uranyl group as shown in Figure 66.

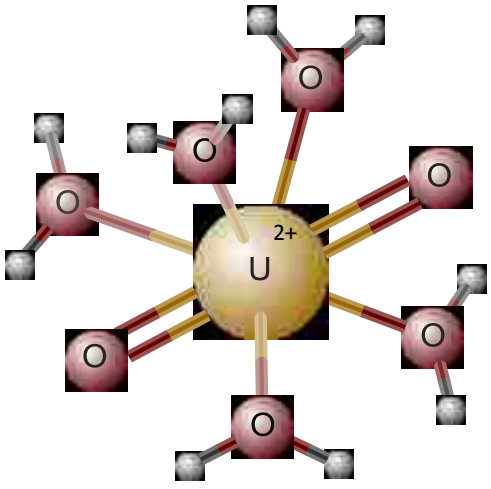

Figure 66 Calculated structure of $UO_2(H_2O)_5^{2+}$ structures in HNO_3 solution [142, 143].

The uranyl ion (UO_2^{2+}) is the main aqueous species and is isostructural with plutonyl and neptunyl species. The bond distances for U, Np, and Pu in the +5 and +6 oxidation states are shown in Table 14, alongside the mixed oxidation state data for Am from EXAFS and the corresponding DFT results from the present study. Both the experimental data and the DFT results for the U, Np, and Pu complexes, appearing in Table 14, are from published work [95, 143].

Table 14 Comparison of calculated properties of actinyl aqua complexes for both An(VI) and An(V) oxidation states. Data for the U, Np and Pu complexes are from references 97 and 138. Calculated bond distances for Am complexes correspond to averaged axial and equatorial distances.

	$UO_2(H_2O)_5^{2+}$		$NpO_2(H_2O)_5^{2+}$		$PuO_2(H_2O)_5^{2+}$		$AmO_2(H_2O)_5^{2+}$	
	Calc.	Exp.	Calc.	Exp.	Calc.	Exp.	Calc.	Exp.*
An– $O_{ax(2)}$	1.756	1.76, 1.78	1.752	1.75	1.742	1.74	1.815	1.81
An– O_{eq}	2.516	2.41	2.50	2.42	2.485	2.41	2.521	2.49
	$UO_2(H_2O)_5^{+}$		$NpO_2(H_2O)_5^{+}$		$PuO_2(H_2O)_5^{+}$		$AmO_2(H_2O)_5^{+}$	
	Calc.	Exp.	Calc.	Exp.	Calc.	Exp.	Calc.	Exp.*
An– $O_{ax(2)}$	1.810		1.81	1.83	1.808	1.81	1.845	1.81
An– O_{eq}	2.616		2.61	2.50	2.61	2.47	2.579	2.49

*Experimental mixture $AmO_2(H_2O)_5^{+\backslash 2+}$

The structures of the $AmO_2(H_2O)_5^{2+}$ and $AmO_2(H_2O)_5^{+}$ complexes optimized with DFT are shown in Figure 67. The $AmO_2(H_2O)_5^{+}$ complex features no particular symmetry (C_1 point group symmetry) due to the orientation of the H_2O ligands, while the $AmO_2(H_2O)_5^{2+}$ complex exhibits an approximate D_{5h} point group symmetry. In the $AmO_2(H_2O)_5^{2+}$ complex, the Am–O_{ax} distances are 1.814 and 1.816 Å (ie. average of

1.815 Å) and the $Am–O_{eq}$ distances are in the range 2.509-2.533 Å (average of 2.521 Å). In the $AmO_2(H_2O)_5^+$ complex, both $Am–O_{ax}$ distances are 1.845 Å and the $Am–O_{eq}$ distances vary between 2.573 and 2.589 Å (average of 2.579 Å). The bond distances calculated for $AmO_2(H_2O)_5^{2+}$ in particular compare well with the EXAFS estimates of 1.81 and 2.49 Å for the $AmO_2(H_2O)_5^{+\backslash 2+}$ mixture. For the sake of comparison, the AmO_2^{2+} and AmO_2^+ ions were also optimized in the gas phase and were found to have $Am–O_{ax}$ distances of 1.873 and 1.834 Å, respectively. The large bond contraction of 0.058 Å of $Am–O_{ax}$ for AmO_2^{2+} upon hydration, compared with the modest 0.011 Å elongation of $Am–O_{ax}$ for the hydrated $AmO_2(H_2O)_5^+$ which tends to suggest a larger degree of stabilization of AmO_2^{2+} as a result of hydration. However, in nitric acid solution, Am(VI) is less stable with respect to Am(V) as observed experimentally. This indicates that in aqueous nitric acid media the effect of solvation and/or the potential redox reactions with species in solution change the energetic landscape in favor of Am(V).

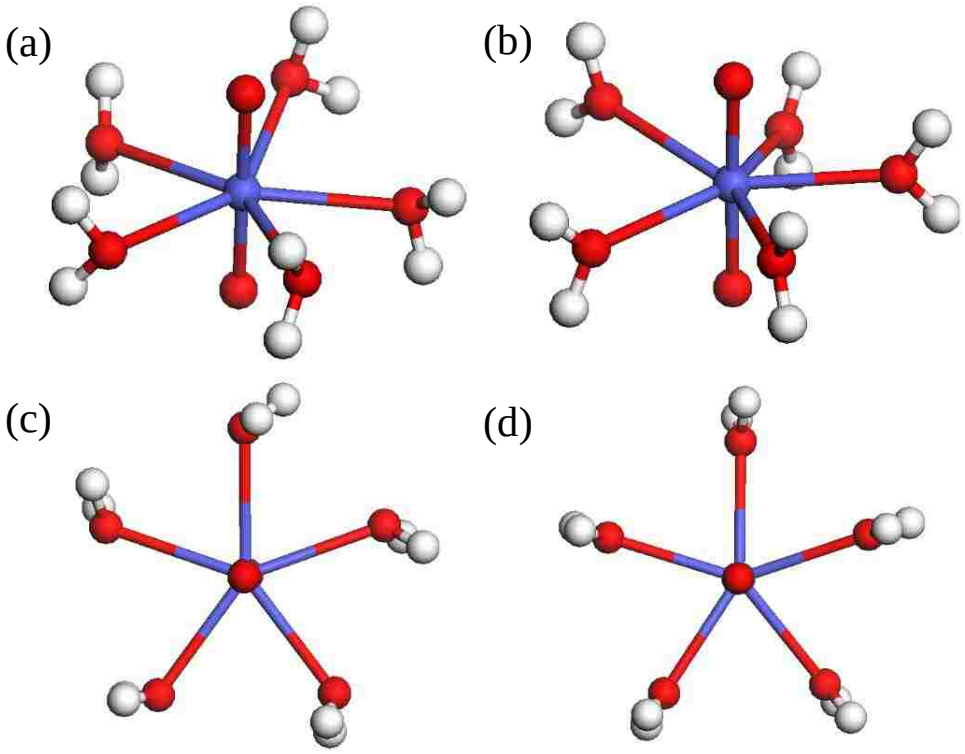

Figure 67 Optimized structures of $AmO_2(H_2O)_5^+$ [(a) and (c)] and $AmO_2(H_2O)_5^{2+}$ [(b) and (d)] calculated with DFT. Am= ● ; O= ● ; H= ○.

A standard indication of kinetic stability and chemical hardness of molecular systems is given by the energy separation between the highest occupied molecular orbital **(**HOMO) and the lowest unoccupied molecular orbital (LUMO), where a large energy gap implies higher stability [171, 172]. The energy gap, calculated at the GGA/PW91 level of theory, for the frontier molecular orbital levels are 1.24 eV for $AmO_2(H_2O)_5^{2+}$ and 0.93 eV for $AmO_2(H_2O)_5^+$ indicating the Am(VI) would have a higher kinetic stability. The calculated HOMO-LUMO gaps for the AmO_2^{2+} and AmO_2^+ ions in the gas phase are 2.14 and 1.59 eV, respectively, again suggesting that the Am(VI) oxidation state is energetically more favorable than Am(V). Interestingly, the energy gaps of

AmO_2^{2+} and AmO_2^{+} are reduced by 0.90 and 0.66 eV, respectively, after addition of solvent molecules, thus pointing to a slight decrease in stability of those complexes upon hydration. The computed frontier orbitals for the $AmO_2(H_2O)_5^{+\backslash 2+}$ and $AmO_2^{+\backslash 2+}$ complexes are depicted in Figure 68.

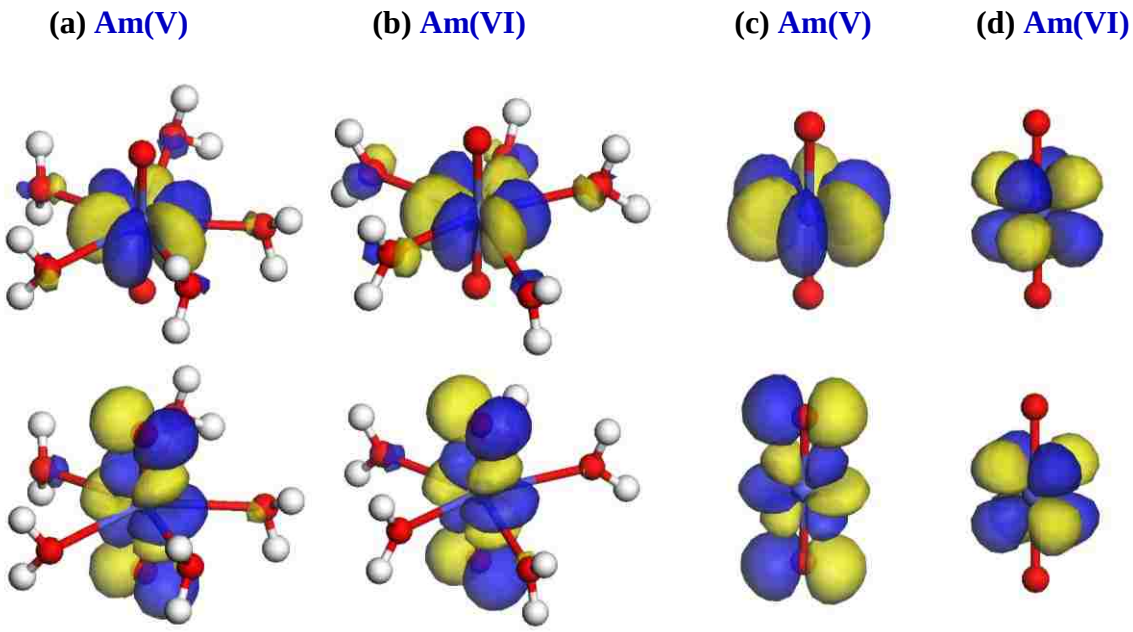

Figure 68 The highest occupied molecular orbital **(**HOMO; top row) and lowest unoccupied molecular orbital (LUMO; bottom row) calculated with DFT for: (a) $AmO_2(H_2O)_5^{+}$, (b) $AmO_2(H_2O)_5^{2+}$, (c) AmO_2^{+} and (d) AmO_2^{2+}. Am= ●; O= ●; H=○. The yellow and blue lobes correspond to positive and negative values of the wave functions.

As shown in Figure 68, a large degree of similarity exists between the frontier orbitals of the various complexes. With the exception of the HOMO and LUMO of AmO_2^{2+}, featuring Am $5f_{xyz}$ orbitals, all the HOMOs of the other complexes are based on the Am $5f_{x(x^2-3y^2)}$ and the LUMOs are made of Am $5f_{xz}^2$. Some contribution of the O_{eq} 2p

orbitals is also seen, however, no noticeable orbital hybridization occurs in those frontier orbitals. There are also significant changes to both HOMO and LUMO for AmO_2^{2+} upon hydration, however, only limited changes are observed for the frontier orbitals of AmO_2^{+} upon hydration once again suggesting higher stability for the AmO_2^{2+}.

Partial charge analysis using the Hirshfeld partitioning of the electron density was also carried out for the americyl complexes. Hirshfeld charges are expected to provide a chemically accurate description of the interplay for charge redistribution and structural changes occurring within the complexes upon modification of their molecular environment [173]. In $AmO_2(H_2O)_5^{2+}$, the charges carried by the different atoms are: +0.82 *e* for Am, -0.16 *e* for O_{ax}, -0.15 *e* for O_{eq}, and +0.22 *e* for H. In $AmO_2(H_2O)_5^{+}$, the calculated charges are: +0.63 *e* for Am, -0.30 *e* for O_{ax}, -0.19 *e* for O_{eq}, and +0.19 *e* for H. When compared, the computed charges for the AmO_2^{2+} and AmO_2^{+} ions are, respectively, +1.79 and +1.31 *e* for Am, and +0.11 and -0.15 *e* for O_{ax}.

Within the actinide complexes of $AnO_2(H_2O)_5^{2+}$ corresponding to An(VI), a very slight contraction in the bond distances is observed from U through Pu, followed by a noticeable increase of the bond distances for Am. For the series $AnO_2(H_2O)_5^{+}$ corresponding to the An(V) oxidation state, the calculated values for the actinyl axial bond lengths are all approximately 1.81 Å [143]. When compared to U, Np, and Pu, the Am(V) and Am(VI) axial bond distances are slightly longer, as anticipated, at 1.845 Å and 1.815 Å, respectively. The calculated equatorial bond lengths for Am(V) and Am(VI) are 2.579 Å and 2.521 Å, respectively, which compare closely to the equatorial bond lengths for U, Pu, and Np of the same oxidation states.

From previous work [143, 168], the $UO_2(H_2O)_5^{2+}$ was found to be the most stable complex for U in solution, however, for Pu the $PuO_2(H_2O)_5^{+}$ appears to be more stable. Considering the computational results obtained for the Am(V) and Am(VI) complexes, the Am(V/VI) mixed sample investigated experimentally appears to coincide with $AmO_2(H_2O)_5^{2+}$ to a greater degree than with the $AmO_2(H_2O)_5^{+}$, and it is thus plausible that there is a higher concentration of Am(VI) in the sample than Am(V). However, considering the stability of Am(V) over Am(VI) in nitric acid solution over time, it is evident that more refined analysis is needed in order to account for salvation effects and potential redox reactions. It is possible that even at concentrations between 0.5 - 1 M HNO_3 that Am(VI) could pull electrons from either the nitrate or the water to produce Am(V) oxidized species. However, in previous work [135], the effects of nitration were seen when concentrations of nitrate in solution were >2 M which increased the potential for anionic nitrato species formation. Further work is needed to establish at what point nitrate, as well as water radiolysis, can achieve this type of formation and redox behavior.

In order to support the characterization of Am(V) and Am(VI), beyond the data collected for EXAFS , DFT was performed with the expectation that both experimental data and the computational data would form a model showing similarities to the other actinyl species. What was ultimately observed was different than expected in that the Am(VI), presumably the main component in the ANL/APS sample, was also found to be predominant in the SSRL sample mixture according to DFT analysis and experimental data comparison. Considering the experimental data observed for Am(VI), with respect to UV-Visible in the presence of excess solid sodium bismuthate, this outcome seems

reasonable, however, there is still a great deal that needs to be examined using computational methods for both Am(V) and Am(VI) in aqueous acidic solution.

7.3 Future Work

This study has added new information in the assessment of scalar relativistic ab initio calculations in modeling Am higher oxidation states. The theoretical analysis of these higher oxidation states sheds light on the unusual electronic structure and stability of this system. Overall, the DFT results provide a good description of the structure and chemical properties of an Am-aquo mixed oxidation state. The results show that systems with mixed Am oxidation states will be predominately Am(VI) using sodium bismuthate as the oxidizing agent in future nuclear fuel reprocessing or recycling systems.

There is a great deal of work that still needs to be accomplished in order to completely characterize Am(V) and Am(VI) oxidation states including further DFT analysis. Even though the DFT computations indicated the hydrated AmO_2^{2+} species was more stable based on the HOMO and LUMO gap than the AmO_2^{+} species, this does not explain why the AmO_2^{+} species appears to be the more stable oxidation state in nitric acid solution. Further evaluation of these redox reaction differences will need to be investigated and the analysis of the individual Am(V) and Am(VI) species will be needed for complete characterization of these species in acidic solution. The relative stabilities of Am(V) and Am(VI) redox potentials could be examined with greater focus placed on the reduction kinetics of the two species. Since the reduction kinetics for Am(V) and Am(VI) presented in this work were limited in nature, there is considerable room for further evaluation and comparison of the reduction potentials. As stated in future work from Chapter 5, a new path is required to in order to Am(V) and Am(VI) in their separate

oxidation states when using sodium bismuthate. This work has established a new direction for further research using DFT calculations and ultimately an avenue through which an Am(V) model can be confirm.

CHAPTER 8

CONCLUSIONS

8.1 Characterization of Am(V/VI) with XAFS

To assist in the characterization of Am(V) and Am(VI) formation from sodium bismuthate, XAFS studies were performed. In this work, sodium bismuthate has shown the ability to produce Am(V) or Am(VI) in acidic solution that will persist long enough to allow experimental analysis using XAFS. The contributions of this work include establishment of long term stability of Am(VI) or Am(V) in lower concentrations of HNO_3, in the presence of excess $NaBiO_3$, measurement of bond distances for a mixture of oxidized Am showing predominance of Am(VI), and confirmation of bonding pattern similarities with the other actinyl species in solution.

In this work, two XAFS experiments were performed to initially establish the Am(VI) oxidation state stability in the beam using excess sodium bismuthate and secondly, to produce XAFS data for both Am(V) and Am(VI) with and without the presence of sodium bismuthate. The isotope ^{243}Am was used in the characterization of the oxidized species and peroxide free sodium bismuthate was used for the oxidation in all experiments. Analysis of Am(V) and Am(VI) prior to the XAFS experiment established by UV-visible spectroscopy and showed complete oxidation of Am(III) to Am(VI) with <1% Am(III) present. Ultraviolet-visible spectroscopy was also used to establish the complete reduction of Am(VI) to Am(V) in the presence and absence of sodium bismuthate over time.

The initial XAFS experiment, oxidized Am(VI) in the presence of sodium bismuthate, produced inconclusive results in the EXAFS region due to low ^{243}Am concentration in the sample. However, the XANES region for the Am(VI) sample showed a marked increase in energy over that of Am(III) indicative of the Am(VI) oxidation state. Subsequent XAFS results produced both EXAFS and XANES data for Am(V) and Am(VI), however, the samples containing no sodium bismuthate reduced immediately to Am(III). The sample containing sodium bismuthate produced a mixture of Am(V/VI) oxidation states with Am(V) being the dominant species as indicated by analysis of the Am-O bond lengths. Results for both XAFS experiments are summarized in Table 15.

Table 15 EXAFS and XANES experimental results for both ANL/APS and SSRL experiments compared to literature results for U(VI) and Pu(V).

	$UO_2(H_2O)_5^{2+}$	$PuO_2(H_2O)_5^{+}$	$AmO_2(H_2O)_5^{+,\2+}$ (SSRL)		
	R(Å)	R(Å)	R(Å)		
An– $O_{ax(2)}$	1.78[a]	1.81[a]	1.81		
An– O_{eq}	2.41[a]	2.47[a]	2.49		
	$UO_2(H_2O)_5^{2+}$	$PuO_2(H_2O)_5^{+}$	$AmO_2(H_2O)_5^{+,\ 2+}$ (SSRL)	(APS)	Am^{3+}
Energy (keV)	17.174[a]	18.061[b]	18.522	18.525	18.518[c]

[a][143], [b][142], [c][174]

The results from both XAFS experiments show an absorption energy edge increase over Am^{3+} of 0.004 and 0.007keV for SSRL and ANL/APS, respectively,

indicating an oxidation shift to a higher energy level. Although the higher of the two energy levels in the XANES region, from ANL/APS data, indicates the presence of Am(VI), the inconclusive data for the bond distances in the EXAFS region makes an absolute conclusion difficult. The SSRL data indicates both a higher energy level than Am^{3+} in the XANES region as well as showing similarities in bond distances to the other actinyls, in particular, $PuO_2(H_2O)_5^+$.

8.2 Determination of Am(V) Single Crystal Synthesis

This work contributed to the establishment of a new crystal synthesis route for the production of americyl(V) crystals from acidic solution using a sodium bismuthate oxidizing agent. The americyl(V) crystals showed visual stability overtime and a successful crystallization route giving future researchers a good experimental base from which to continue this work.

To further characterize Am higher oxidation states, primarily the Am(V) species, a single crystal synthesis of sodium americyl(V) acetate was performed. Structural information on the Am(VI) oxidation state through single crystal synthesis, established by Asprey, Stephanou, and Penneman [34], identified a hexagonal bipryramidal structure with a lattice constant of a_o=10.6 Å, similar to the uranyl, neptunyl, and plutonyl analogs. More recent work on sodium uranyl(VI) acetate crystals has also shown hexagonal bipyramidal structures which are indicative of sodium actinyl acetate crystals including Am [150].

The $Na[Am(VI)O_2(OAc)_3]$ has eight coordination with bidentate acetates, similar to the U, Np, and Pu analogues. From crystal synthesis experiments using U as an analog

for Am(V) crystals, it was possible to develop an experimental procedure in which sodium Am(V) acetate crystals were grown in the same fashion as the U crystals after the Am solution was oxidized from Am(III) to Am(V) in $HClO_4$. The structure of the $Na[Am(V)O_2(OAc)_3]$ would be expected to be in line with those of U, Np, and Pu and is shown in Figure 69.

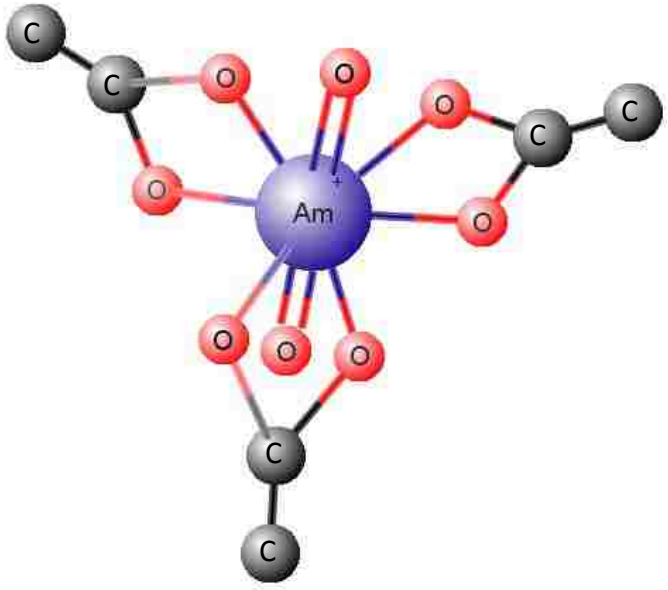

Figure 69 Proposed structure of $Na[Am(V)O_2(OAc)_3]$. The hydrogen atoms have been omitted for clarity.

Although diffractometry was not possible on the $Na[Am(V)O_2(OAc)_3]$ crystals due to radiolysis decomposition, the fact that crystals were produced using sodium bismuthate as the oxidizing agent is an important step for the forthcoming characterization of this actinyl. Future work on the sodium americyl(V) acetate crystal will have a valid experimental starting point for the synthesis of crystals as well as a time

frame in which analysis can be performed before decomposition of these crystals takes place.

8.3 Characterization of Am(V) with Computational Chemistry

Chemistry

The DFT characterization for this work indicated Am(VI) as the dominant species when using sodium bismuthate as the oxidizing agent in acidic solution based on band gap energies. These results compared well with the SSRL EXAFS data of the mixed oxidation state Am(V/VI) species which showed similar bond distances and coordination chemistry for Am(VI). The contribution of DFT results in combination with the EXAFS data from SSRL and XANES results from ANL/APS establish a pattern of Am(VI) dominance in solution only in the presence of excess solid sodium bismuthate.

Density Functional Theory was used in an effort to further characterize the Am(V/VI) mixed oxidation state results obtained from the EXAFS data. By using this computational chemistry approach to the Am mixture it was hoped that a dominant oxidation state species could be found. Ground state geometries and properties were found using the DMol^3 software program along with generalized gradient approximations (GGA) and local density approximation (LDA), which were both tested with the parameterization of Perdew and Wang (PW91). Double numerical basis sets including polarization functions (DNP) for all atoms were used in the calculations of the Am(V/VI) mixture. Using the information supplied by DFT methods, an interesting model of the Am(V/VI) data began to appear.

The DFT analysis showed a structure in keeping with that of the other actinyls, U, Np, and Pu. The DFT structure for $AmO_2(H_2O)_5^{+\backslash 2+}$, shown in Figure 70, bares an exact resemblance to its uranyl, neptunyl, and plutonyl analogs with the difference appearing in the bond distances for axial and equatorial oxygen's. The DFT calculated bond distances

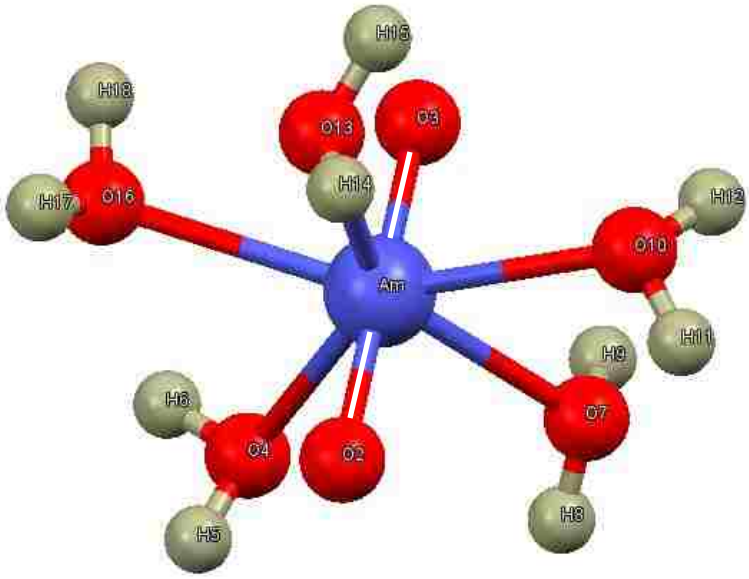

Figure 70 DFT model of $AmO_2(H_2O)_5^{q+}$ structure where q= 1 or 2.

for Am(V) were: Am-O_{ax} and Am-O_{eq}= 1.85 Å and 2.58 Å, respectively. For Am(VI); Am-O_{ax} and Am-O_{eq}= 1.82 Å and 2.52 Å, respectively. The bond distances for the Am(V/VI) mixture revealed an Am(VI) dominance in the sample. However, the bond distances were slightly higher for the Am(VI) oxidation state when compared against the other actinyl analogs. The DFT data showed possible interference from Am(V) that was present in the solution, producing slightly higher than expected bond distances for Am(VI).

Until a method can be developed to keep the Am(V) and Am(VI) oxidation states pure in solution using sodium bismuthate or another holding oxidant, a mixture will continue to be pervasive in EXAFS data. The results of DFT calculations for the Am(V) and Am(VI) complexes help in interpreting the EXAFS data and can guide further experiments. The EXAFS data on the Am(V,VI) mixture in acidic solution in the presence of sodium bismuthate has provided new information that can contribute to the design of separation systems for americium in the future.

APPENDIX

SUPPLEMENTAL DATA

DFT

Atom Properties $AmO_2(H_2O)_5^+$

	Element	Type	Valence	Formal Charge	Partial Charge	X(Å)	Y(Å)	Z(Å)
Atom 1	O	O3	1	0	0.00	-0.1000	1.8620	-0.0010
Atom 2	O	O3	1	0	0.00	0.1410	-1.8100	-0.0080
Atom 3	O	O3	2	0	0.00	-2.3340	0.2240	1.0600
Atom 4	H	HO	1	0	0.00	-2.6340	1.1410	0.9240
Atom 5	H	HO	1	0	0.00	-3.0200	-0.3330	0.6500
Atom 6	0	O3	2	0	0.00	0.2670	-0.2080	2.5550
Atom 7	H	HO	1	0	0.00	-0.3510	0.3360	3.0740
Atom 8	H	HO	1	0	0.00	0.0810	-1.1260	2.8200
Atom 9	O	O3	2	0	0.00	2.5330	0.1660	0.5300
Atom 10	H	HO	1	0	0.00	2.7960	0.9580	1.0320
Atom 11	H	HO	1	0	0.00	2.8750	-0.5890	1.0390
Atom 12	O	O3	2	0	0.00	1.2320	0.2610	-2.2600
Atom 13	H	HO	1	0	0.00	1.6720	1.1250	-2.3550
Atom 14	H	HO	1	0	0.00	1.9180	-0.4020	-2.4520
Atom 15	O	O3	2	0	0.00	-1.7400	-0.3960	-1.8500
Atom 16	H	HO	1	0	0.00	-1.7190	0.1980	-2.6210
Atom 17	H	HO	1	0	0.00	-1.6220	-1.2930	-2.2090
Atom 18	Am	Am	2	0	0.00	0.0180	0.0210	-0.0040

Bond Properties $AmO_2(H_2O)_5^+$

	Type	Start Atom	End Atom	Bond Order	Rotatable	Length (Å)
Bond 1	H-O	H9	O7	1	No	0.973508
Bond 2	H-O	H8	O6	1	No	0.973154
Bond 3	H-O	H7	O6	1	No	0.974228
Bond 4	H-O	H10	O7	1	No	0.973352
Bond 5	O-Am	O2	Am	1	No	1.84511
Bond 6	Am-O	Am	O1	1	No	1.84478
Bond 7	Am-O	Am	O5	1	No	2.57887
Bond 8	O-Am-O	Am	O2	1	No	3.59510
Bond 9	O-H	O5	H5	1	No	0.973877
Bond 10	O-H	O5	H6	1	No	0.972661
Bond 11	H-O	H2	O3	1	No	0.974138
Bond 12	H-O	H1	O3	1	No	0.974364
Bond 13	O-H	O4	H4	1	No	0.973419
Bond 14	O-H	O4	H3	1	No	0.973253

Angle Properties $AmO_2(H_2O)_5^+$

	Type	Start Atom	Vertex	End Atom	Angle (^{o})
Angle 1	HOH	H1	O3	H2	105.2218
Angle 2	HOH	H3	O4	H4	105.1070
Angle 3	HOH	H5	O5	H6	105.4594
Angle 4	HOH	H7	O6	H8	105.4618
Angle 5	HOH	H9	O7	H10	105.5204
Angle 6	OAmO	O1	Am	O2	179.8420

Atom Properties $AmO_2(H_2O)_5^{2+}$

	Element	Type	Valence	Formal Charge	Partial Charge	X(Å)	Y(Å)	Z(Å)
Atom 1	O	O3	1	0	0.00	-0.02500	1.81700	0.04000
Atom 2	O	O3	1	0	0.00	0.12100	-1.80900	-0.02700
Atom 3	O	O3	2	0	0.00	-2.36100	0.41100	0.73600
Atom 4	H	HO	1	0	0.00	-2.70900	1.30700	0.91700
Atom 5	H	HO	1	0	0.00	-3.08600	-0.21800	0.91800
Atom 6	0	O3	2	0	0.00	-0.04000	-0.39300	2.49000
Atom 7	H	HO	1	0	0.00	-0.14700	0.25300	3.21500
Atom 8	H	HO	1	0	0.00	0.11500	-1.26400	2.90500
Atom 9	O	O3	2	0	0.00	2.39400	0.21100	0.80200
Atom 10	H	HO	1	0	0.00	2.87100	1.05500	0.92500
Atom 11	H	HO	1	0	0.00	3.03400	-0.50700	0.97100
Atom 12	O	O3	2	0	0.00	1.42200	0.31300	-2.05900
Atom 13	H	HO	1	0	0.00	1.66700	1.17600	-2.44800
Atom 14	H	HO	1	0	0.00	1.78900	-0.37900	-2.64200
Atom 15	O	O3	2	0	0.00	-1.45700	-0.51100	-1.97800
Atom 16	H	HO	1	0	0.00	-1.93200	0.08700	-2.58700
Atom 17	H	HO	1	0	0.00	-1.66100	-1.42400	-2.25900
Atom 18	Am	Am	2	0	0.00	0.02200	0.00200	0.00600

Bond Properties $AmO_2(H_2O)_5^{2+}$

	Type	Start Atom	End Atom	Bond Order	Rotatable	Length (Å)
Bond 1	O-Am	O1	Am	1	No	1.81593
Bond 2	O-Am	O2	Am	1	No	1.81400
Bond 3	Am-O	Am	O5	1	No	2.52100
Bond 4	O-Am-O	Am	O2	1	No	3.59500
Bond 5	O-H	O3	H1	1	No	0.978101
Bond 6	O-H	O3	H2	1	No	0.976929
Bond 7	O-H	O4	H4	1	No	0.977185
Bond 8	O-H	O4	H3	1	No	0.976929
Bond 9	O-H	O5	H5	1	No	0.977238
Bond 10	O-H	O5	H6	1	No	0.976568
Bond 11	O-H	O6	H8	1	No	0.976444
Bond 12	O-H	O6	H7	1	No	0.977811
Bond 13	O-H	O7	H9	1	No	0.976786
Bond 14	O-H	O7	H10	1	No	0.976804

Angle Properties $AmO_2(H_2O)_5^{2+}$

	Type	Start Atom	Vertex	End Atom	Angle (^{o})
Angle 1	HOH	H1	O3	H2	106.9355
Angle 2	HOH	H3	O4	H4	106.9539
Angle 3	HOH	H5	O5	H6	107.0567
Angle 4	HOH	H7	O6	H8	107.0844
Angle 5	HOH	H9	O7	H10	106.9363
Angle 6	OAmO	O1	Am	O2	178.3543

BIBLIOGRAPHY

1. Nuclear Power in the USA. In: *World Nuclear Association.* United kingdom; 2014.
2. Phillips J: Sustainable Nuclear Power Initiative. In: *Pacific Northwest National Laboratory Focus Area Fact Sheet.* PNNL; August 2008.
3. Staff: New Nuclear Energy Facilities Will Support Growth, Provide Clean Electricity. In: *Nuclear Energy Institute, NEI.* Washington, DC: Nuclear Energy Institute, NEI; 2010: 4.
4. Nuclear Energy Performance Plan. 2009.
5. Forsberg CW: Disposal of Partitioning-Transmutation Wastes with Separate Manaagement of High-Heat radionuclides. In: *6th Information Exchange Mtg on Actinide and Fission Product Partitioning and Transmutation, Session: Nuclear Waste Transmutation.* Madrid, Spain: Organization for Economic Cooperation and Development Nuclear Energy Agency; 2000.
6. Kelly JE: Paving the path for next-generation nuclear energy. In: *Office of Nuclear Energy.* Energy.gov; 2013.
7. Wigeland RA, Bauer TH, Fanning TH, Morris EE: Spent Nuclear Fuel Separations and Transmutation Criteria for Benefit to a Geologic Repository. In: *Waste Management '04: 2004; Tucson, AZ*; 2004.
8. Chemical Separation Technologies and Related Methodes in Nuclear Waste Management: Applications, Problems, and Research Needs, vol. 53. Dubna, Russia: Kluwer Academic Publishers; 1998.
9. Saito A, Choppin GR: Separation of Actinides in Dlfferent Oxidation States from Neutral Solutions by Solvent Extraction. *Analytical Chemistry* 1983, 55:2454-2457.
10. Mincher BJ, Martin LR, Schmitt NC: Tributylphosphate Extraction Behavior of Bismuthate-Oxidized Americium. *Inorg Chem,* 2008, 47(15):6984-6989.
11. Hara M, Suzuki S: Oxidation of Americium(III) with Sodium Bismuthate *J Radioanalytical Chem* 1977, 36:95-104.
12. Martin L, Mincher BJ, Schmitt NC: Understanding the Chemistry of Uncommon Americium Oxidation States for Application to Actinide/Lanthanide Separations. In: *GLOBAL.* Boise, ID; 2007.
13. AREVA, Industries MH, Limited JNF, Services BWT, Technology BE, Division UW: Integrated U.S. Used Fuel Strategy - Analyses Performed by the International Nuclear Recycling Alliance. *International Nuclear Recycling Alliance* 2008, 22.
14. Andrews A: Nuclear Fuel Reprocessing: U.S. Policy Development. *CRS Report for Congress* March 27, 2008.
15. Lagus TP: Reprocessing of Spent Nuclear Fuel: A Policy Analysis. *Journal of Engineering and Public Policy* 2005, 9.
16. Committee NNS: Actinide Separation Chemistry in Nuclear Waste Streams and Materials. In.: Nuclear Energy Agency Organization for Economic Co-Operation and Development; 1997.
17. Carre F, Delbecq JM: Overview on the French Nuclear Fuel Cycle Strategy and Transition Scenario Studies. In: *Global 2009: 6-11 September 2009; Paris, France*; 2009.

18. Nikitin MB, Andrews A, Holt M: Managing the Nuclear Fuel Cycle: Policy Implications of Expanding Global Access to Nuclear Power. 2011, CRS Report to Congress.
19. Klein D: Waste not, want not: The time has come for the U.S. to recycle its spent nuclear fuel. *American Nuclear Society Cafe* 2011.
20. McKay HAC, Miles JH, Swanson JL: The PUREX Process. In: *Science and Technology of Tributylphosphate, Vol 3, Applicaitions of Tributyl Phosphate in Nuclear Fuel Reprocessing.* vol. 3. Raton: CRC Press; 1990: 272.
21. Staff: PUREX Process. In. Brussels: European Nuclear Society; 2013.
22. Staff: Processing of Used Nuclear Fuel. In: *World Nuclear Association.* London, UK; June 2013.
23. Chang GS: Enhancing VVER Annular Proliferation Resistance Fuel With Minor Actinides. In: *13th International Conference on Emerging Nuclear Energy Systems: June 3-8 2007; Istanbul, Turkey*; 2007.
24. Schneider M, Marigna Y: Spent Nuclear Fuel Reprocessing in France. *Research Report No 4 International Panel on Fissile Materials* 2008.
25. Loveland WD, Morrissey DJ, Seaborg GT: Modern Nuclear Chemistry In.: Wiley; 2006.
26. Crowder ML, Thompson MC: Studies with Ferrous Sulfamate and Alternate Reductants for 2nd Uranium Cycle. In. Edited by Westinghouse; 2002.
27. Advanced Separation Techniques for Nuclear Fuel Reprocessing and Radioactive Waste Treatment. In: *Series in Energy No 2.* Edited by Nash KL, Lumetta GJ: Woodhead 2011.
28. Riddle CL, Baker JD, Law JD, McGrath CA, Meikrantz DH, Mincher BJ, Peterman DR, Todd TA: Fission Product Extraction (FPEX): Development of a Novel Solvent for the Simultaneous Separation of Strontium and Cesium from Acidic Solutions. *Solvent Extraction and Ion Exchange* 2005, 23:449-461.
29. Egorov NN, Zakharov MA, Lazarev LN, Lyubtsev RI, Nikiforov AS, Strakhov MV, Filippov EA: New Approaches to Solving the Management Problem of Long-Lived Radionuclides. In: *Proceedings of The Third International Conference on Nuclear Fuel Reprocessing and Waste Management: 14-18 April, 1991*: RECOD; 14-18 April, 1991: 357.
30. Lumetta GJ, Braley JC, Sinkov SI, Levitskaia TG, Carter JC, Warner MG, Pittman JW: Sigma Team for Minor Actinide Separation: PNNL FY 2011 Status Report. In. Edited by PNNL FCRaD; 2011.
31. Cotton S: Lanthanide and Actinide Chemistry John Wiley & Sons, Ltd. ; 2006.
32. Lumeta GJ, Thompson MC, Penneman RA, Eller PG: The Chemistry of the Actinide and Transactinide Elements: Curium, 3 edn: Springer; 2008.
33. Clark DL, Hecker SS, Jarvinen GD, Neu MP: Plutonium. In: *The Chemistry of the Actinide and Transactinde Elements.* Edited by L.R. Morss NME, J. Fuger, vol. 2, 4 edn: Springer; 2010: 813-1264.
34. Asprey LB, Stephanou SE, Penneman RA: Hexavalent Americium. *J Am Chem Soc* 1951, 72(12):5715–5717.
35. Delley B: From Molecules to Solids with the $DMol^3$ Approach. *J Chem Phys* 2000, 113:7756–7764.

36. Nikonov MV, Gogolev AV, Tananaev IG, Myasoedov BF: Reaction of Am(VI) with Na4XeO6 in Alkaline Solutions in the Presence of Ozone. *Radiochemistry* 2005, 47(482-483.).
37. Fedoseev AM, Shilov VP: Oxidation of Am(III) to Am(IV) with Ozone in Solutions of Heteropolyanions. *Radiochemistry* 2010, 52(1):40-42.
38. Werner LB, Perlman I: The Pentavalent State of Americium. *J Am Chem Soc* 1951, 73(12):495-496.
39. Asprey LB, Penneman RA: Preparation and Properties of Aqueous Tetravalent Americium. *Inorg Chem* 1962, 1(1):134-136.
40. Tsuyoshi Nishi MN, Akinori Itoh, Chikashi Suzuki,, Masaru Hirata MA: EXAFS and XANES studies of americium dioxide with fluorite structure. *Journal of Nuclear Materials* 2008, 347:339–343.
41. Tian G, Zhua Y, Xua J, Hub T, Xieb Y: Characterization of extraction complexes of Am(III) with dialkyldithiophosphinic acids by extended X-ray absorption fine structure spectroscopy. *Journal of Alloys and Compounds* 2002, 334:86–91.
42. Stumpf S, Billard I, Gaillard C, Panak PJ, Dardenne K: TRLFS and EXAFS investigations of lanthanide and actinide complexation by triflate and perchlorate in an ionic liquid. *Radiochim Acta* 2008, 96:1-10.
43. Stover BJ, Conway JG, Cunningham BB: The solution absorption spectrum of americium. *J Am Chem Soc* 1951, 73:491-492.
44. Bourges JY, Guillaume B, Koely G, Hobart DE, Peterson JR: Coexistance of Americium in Four Oxidaiton States in Sodium-Carbonate and Sodium-BiCarbonate Medium. *Inorg Chem* 1983, 22:1179-1184.
45. Mincher BJ, Schmitt NC, Tillotson RD, Elias G, White BM, Law JD: Characterizing Diamylamylphosphonate (DAAP) as an Americium Ligand for Nuclear Fuel-Cycle Applications. *Solvent Extraction and Ion Exchange* 2014, 32(2):153-166.
46. Goff GS, Long KM, Reilly SD, Jarvinen GD, Runde WH: Americium/Lanthanide Separations in Alkaline Solutions for Advanced Nuclear Fuel Cycles. In: *36th Actinide Separations Conference: May 5, 2012; Chattanooga, TN*; May 5, 2012.
47. The 2013 Fuel Cycle Campaign. In. Edited by DOE. Washington D.C.; 2014.
48. Separations and Waste Forms Research and Development FY 2012 Accomplishments Report. In. Edited by Laboratory IN; 2013: 245.
49. Research and Development FY 2013 Accomplishments Report for DOE. In. Edited by DOE. Washington DC: DOE; 2014.
50. Stephanou SE, Penneman RA: Observations on Curium Valence States: A Rapid Separation of Americum and Curium. *J Am Chem Soc* 1952, 74:3701-3702.
51. Shehee TC, Martin LR, Nash KL: Solid-liquid separation of oxidized americium from fission product lanthanides. In: *IOP Conf Series: Materials Science and Engineering 9* Edited by Science I: IOP Publishing; 2010.
52. Stokely JR, Moore FL: New Separation Method for Americium Based on Liquid-Liquid Extraction Behavior of Americium(V). *Anal Chem* 1967, 39:994-997.
53. Runde W: Americium and Curium. In: *Radionuclides in the Environment.* Edited by Atwood DA. West Sussex: Wiley and Sons, Inc.; 2010.
54. Holcomb HP: Analytical Oxidation of Americium with Sodium Perxenate. *Anal Chem* 1965, 37(3):415.

55. B.F Myasoedov, I.A Lebedev, P.L Khizhnyak, G.A Timofeev, Frenkel VY: Electrochemical Oxidation of Americium and Californium in Carbonate Solutions *Journal of the Less Common Metals* 1986(122):189–193.
56. Lippard SJ: Noble Gas Compounds as Oxidants or Fluorinators in Organic Chemistry. In: *Progress in Inorganic Chemistry.* vol. 29: Wiley and Sons, Inc.; 1982: 190-204.
57. Musikas C, Germain M, Bathellier A: Americium-Curium Separation by Means of Selective Extraction of Hexavalent Americium Using a Centrifugal Contactor. *ACS Symposium Series* 1980, 117:157–173.
58. Proctor SG, W.V. Conner C: Separation of Cerium from Americium. *J Inorg Nucl Chem* 1970, 36(11):3699-3701.
59. Mincher BJ, Schmitt NC, Case ME: A TRUEX-Based Separation of Americium from the Lanthanides. *Solvent Extraction and Ion Exchange* 2011, 29(2):247-259.
60. Argaman N, Makov G: Density Functional Theory — an introduction. *American Journal of Physics* 2000, 68:69-79.
61. Langreth DC, Mehl MJ: Beyond the local-density approximation in calculations of ground-state electronic properties. *Phys Rev B* 1983, 28:1809.
62. Kohn W, Sham L: Self-Consistent Equations Including Exchange and Correlation Effects. *Phys Rev A* 1965, 140:1133.
63. Becke AD: A new mixing of Hartree-Fock and local density-functional theories. *J Chem Phys* 1993, 98:1372.
64. Hohenberg P, Kohn W: Inhomogeneous Electron Gas. *Phys Rev B* 1964(136):864.
65. Advanced Photon Source. In. Argonne, IL: Argonne National Laboratory; 2013.
66. Seaborg GT, James RA, Morgan LO: The new element americium (atomic number 95). In. Edited by (AEC UAEC. Oak Ridge, TN: Argonne National Laboratory (ANL)); 1948.
67. Seaborg GT, Hamilton JG: The production of elements 95 and 96. *Science* 1945, 102:556.
68. Keller OL: Frontiers of Chemistry for Americium and Curium. In: *CONF-841210.* Oak Ridge, TN; 1984.
69. Sonzogni A: National Nuclear Data Center. In.; 2011.
70. Ferrer RM, Asgari M, Bays SE, Forget B: Fast Reactor Alternative Studies: Effects of Transuranic Groupings on Metal and Oxide Sodium Fast Reactor Designs. In. Edited by DOE: Idaho National Laboratory; 2007.
71. Ghiorso A, James RA, Morgan LO, Seaborg GT: Preparation of Transplutonium Isotopes by Neutron Irradiation. *Phys Rev* 1950, 78(4):472–472
72. Kessler G: Sustainable and Safe Nuclear Fission Energy: Technology and Safety of Fast and Thermal Nuclear Reactors. In. Berlin: Springer; 2012.
73. Penneman RA, Keenan TK: The Radiochemistry of Americium and Curium In: *National Acdemy of Sciences-National Research Council, Nuclear Science Series* Technical Information Center U.S. Atomic Energy Commission; 1960.
74. Runde WH, Schulz WW: The Chemistry of the Actinide and Transactinide Elements, third edition: Americium, 2 edn; 2008.
75. Street K, Seaborg GT: The Separation of Americium and Curium from the Rare Earth Elements. *J Am Chem Soc* 1950, 72:2792.

76. Street K, Ghiorso A, Seaborg G: The Isotopes of Americium. *Physical Review* 1950, 79(3).
77. Seaborg GT: he chemical and radioactive properties of the heavy elements. *Chem Eng News* 1945(23):2190-2193.
78. Shannon RD: Revised effective ionic radii and systematic studies of interatomic distances in halides and chalcogenides *Acta Crystallographica Section C Crystal Structure Communications* 1976, 32:751-767.
79. Penneman RA, Keenan TK: The Radiochemistry of Americium and Curium In: *National Acdemy of Sciences-National Research Council, Nuclear Science Series* Technical Information Center U.S. Atomic Energy Commission; 1960.
80. Hall G, Markin TL: The self-reduction of americium(V) and (VI) and the disproportionation of americium(V) in aqueous solution. *Journal of Inorganic and Nuclear Chemistry* 1957, 4(5-6).
81. Americium. In: *Human Health Fact Sheet.* Argonne National Laboratory, EVS August 2005: 1-2.
82. Chmielewski AG, Urbański TS, Migdał W: Separation technologies for metals recovery from industrial wastes. *Hydrometallurgy* 1997, 45:333-344.
83. Coleman JS: The kinetics of the disproportionation of americium(V). *Inorg Chem* 1963, 2:53-57.
84. Folger H, Trautmann N: Preparation of actinide targets by electrodeposition. *Preparation of actinide targets by electrodeposition* 1989, 282:102-106.
85. Burns JD, Shehee TC, Clearfield A, Hobbs DT: Separation of americium from curium by oxidation and ion exchange. *Anal Chem* 2012, 84(16).
86. Serpa J, Allibertb M, A. Le Terriera, R. Malmbecka, M. Ougiera, Rebizanta J, Glatz JP: Electroseparation of Actinides from Lanthanides on Solid Aluminum Electrode in LiCl-KCl Eutectic Melts *J Electrochem Soc* 2006, 153(10).
87. Fardy JJ, Buchanan JM: Separation of oxidised americium from trivalent transplutonium elements and lanthanides by solvent extraction. *J Inorg Nucl Chem Eng News* 1976, 38:149-154.
88. Serrano-Purroya D, Baronb P, Christiansena B, Glatza JP, Madicc C, Malmbecka R, Modolod G: First Demonstration of a Centrifugal Solvent Extraction Process for Minor Actinides from a Concentrated Spent Fuel Solution. *Separation and Purification Technology* 2005, 45(2):157–162.
89. Suzuki T, Aida M, Ban Y, Fujii Y, Hara M, Mitsugashira T: Group separation of trivalent actinides and lanthanides by tertiary pyridine-type anion-exchange resin embedded in silica beads. *Journal of Radioanalytical and Nuclear Chemistry* 2003 255(3):581-583.
90. Lehto J, Hou X: Chemistry and Analysis of Radionuclides. Weinhiem, Germany: Wiley and Sons, Inc.; 2011.
91. Burney GA: Separation of americium from curium by precipitation of $K_3AmO_2(CO_3)_2$. *Nucl Appl* 1968, 4:217-221.
92. Moore FL: Extraction chromatographic method for rapid separation of americium from other transuranium elements. *Anal Chem* 1968, 40:2130-2133.
93. Kamoshida M, Fukasawa T: Solvent Extraction of Americium(VI) byTri-n-Butyl Phosphate. *Journal of Nuclear Science and Technology* 1996, 33(5).

94. Lundell GEF: The Interference of Cobalt in the Bismuthate Method for Manganese *J Am Chem Soc* 1923, 45(11):2600–2603.
95. Tan X, Fang M, Wang X: Sorption Speciation of Lanthanides/Actinides on Minerals by TRLFS, EXAFS and DFT Studies: A Review. *Molecules* 2010, 15:8431-8468;.
96. Bunker G: Introduction to XAFS: A Practical Guide to X-ray Absorption Fine Structure Spectroscopy. In: *Cambridge University Press.* January, 2010.
97. Takao K, Tsushima S, Takao S, Scheinost AC, G.Bernhard, Ikeda Y, Hennig C: X-ray Absorption Fine Structures of Uranyl(V) Complexes in a Nonaqueous Solution. *Inorg Chem* 2009, 48:9602–9604.
98. Stern EA, Durham PJ: X-ray Absorption: Principles, Applicaiton, Techniques of EXAFS, SEXAFS and XANES, vol. 92: John Wiley & Sons; 1988.
99. Bare SR: XANES Measurements and Interpretation. In. EXAFS Data Collection and Analysis Course, APS: UOP, LLC; 2005.
100. Stern EA, Durham PJ: X-ray Absorption: Principles, Applicaiton, Techniques of EXAFS, SEXAFS and XANES, vol. 92: John Wiley & Sons; 1988.
101. Conradson SD, Schecker J: XAFS: A Technique to Probe Local Structure. In: *Challenges in Plutonium Science.* vol. 26: Los Alamos Science; 2000: 422-435.
102. Newville M: Fundamentals of XAFS. *Consortium for Advanced Radiation Sources* 2008, Revision 1.8.
103. Teo BK: EXAFS: Basic principles and Data Analysis; 1986.
104. Bianconi A, Dell'Ariccia M, Durham PJ, Pendry JB: Multiple-scattering resonances and structural effects in the x-ray-absorption near-edge spectra of Fe II and Fe III hexacyanide complexes. *Phys Rev B* 1982, 26:6502–6508.
105. Suzuki C, Nishi T, Nakada M, Akabori M, Hirata M, Kaji Y: Calculation of the Electronic Structure of AmO_2 and Pr_6O_{11} for XANES Analysis With Redox Property *International Journal of Quantum Chemistry* 2009, 109:2744–2752.
106. Beno MA, Jennings G, Engbretson M, Knapp GS, Kurtz C, Zabransky B, Linton J, Seifert S, Wiley C, Montano PA: Basic Energy Sciences Synchrotron Radiation Center Udulator Sector at the Advanced Photon Source. *Nucl Instrum Meth A* 2001, 467-468:690-693.
107. Stanford Synchrotron Radiation Lightsource (SSRL)
108. Update on SSRL Beam Lines and Techniques. In: *SSRL Headline News.* vol. 6; August 2005.
109. Newville M, Livins P, Yacoby Y, Stern EA, J. J. Rehr: Near-edge x-ray-absorption fine structure of Pb: A comparison of theory and experiment. *Phys Rev* 1993, B47:14126--14131.
110. Newville M, Ravel B: ATHENA, ARTEMIS, HEPHAESTUS: data analysis for X-ray absorption spectroscopy using IFEFFIT. *J Synchrotron Radiation* 2005, 12:537-541.
111. Resslel T: WinXAS: a program for x-ray absorption spectroscopy data analysisunder MS-Windows. *J Synchroton Rad* 1998, 5:118-122.
112. Rehr JJ, Alberts RC: Theoretical Approaches to X-ray Sbsorption Fine Structure. *Rev Mod Phys* 2000, 72:621-654.
113. Ravel B: ATOMS: Crystallography for the X-ray Absorption Spectroscopist. *J Synchrotron Rad* 2001, 8:314-316.

114. Klein C, Hurlbut CS: Manual of Mineralogy, 21 edn: John Wiley & Sons, Inc.; 1999.
115. Clegg W, Blake AJ, Gould RO, Main P: Crystal Structure Analysis: Principles and Practice. In. Oxford: Oxford Science Publications; 2001: 261.
116. Thornton ST, Rex A: Modern Physics for Scientists and Engineers. In., 4th edn: Cengage Learning; 2012.
117. Clark CM, Dutrow BL: Single-Crystal X-ray Diffraction. In: *Science Education Resource Center, Carleton College.* 2011.
118. Ibers JA, Hamilton WA: International Tables for X-ray Crystallography, IV. Birmingham, U.K.: Kynoch Press; 1974.
119. Bruker: SMART, SAINT, SHELXTL software. In. Madison, Wi.; 1998.
120. APEX 2 (version 2009.11-0). Program for Bruker CCD X-ray Diffractometer Control, . In: *Bruker AXS Inc.* Madison, WI.; 2009.
121. Sheldrick GM: SHELXTL, version 6.14. ,Program for solution and refinement of crystal structures. In. Universität Göttingen, Germany; 2000.
122. International Tables for Crystallography, Reciprocal Space. Norwell, MA: Springer; 2008.
123. Harris DC: Exploring Chemical Analysis. New York: W.H. Freeman and Co.; 1997.
124. Handbook of Spectroscopy, vol. 2: Wiley-VCH; 2003.
125. Cary 6000i Operation Manual. In.: Varian, Inc.; May 2010.
126. UV-VIS-NIR Cary 4000, 5000, 6000i Spectrophotometers: Preliminary Performance Data. In. Edited by Inc. V. Australia; 2002.
127. Goldstein J: Scanning electron microscopy and x-ray microanalysis. 2003.
128. Clarke AR (ed.): Microscopy techniques for materials science: CRC Press 2002.
129. Egerton RF (ed.): Physical principles of electron microscopy : an introduction to TEM, SEM, and AEM: Springer; 2005.
130. JSM-7600F and JSM-7600FA Field Emission Scanning Electron Microscope Operation Guide In. Edited by Ltd. J; 2008.
131. Echlin P: Handbook of Sample Preparation for Scanning Electron Microscopy and X-Ray Microanalysis. New York, NY: Springer 2009.
132. Hummer® 6.2 Sputter Coater For SEM Sample Preparation manual. In.: Anatech USA.
133. Knoll G (ed.): Radiation Detection and Measurement: John Wiley & Sons, Inc. NY; 1989.
134. Gilmore G: Practical Gamma-Ray Spectroscopy, 2 edn. West Sussex: Wiley and Sons,Ltd; 2008.
135. Gharibyan N, Crable A, Happel S, Sudowe R: Am and Cm Absorption Studies on TEVA Resin from Metal Nitrate Matrices. In: *237th ACS Meeting: 2009; Salt Lake City, Utah*; 2009.
136. ORTEC. In: *wwwortec-onlinecom.* Oak Ridge, TN: AMETEK Advanced Measurement Technology; 2009.
137. Runde WH, Mincher BJ: Higher Oxidation States of Americium: Preparation, Characterization and Use for Separations. *Chemical Reviews* 2011, 111:5723-5741.

138. Meyer D, Fouchard S, Simoni E, DenAuwer C: Selective dissolution of Am in basic media in the presence of ferricyanide ions: a mechanistic and structural study on Am(V) and Am(VI) compounds. *Radiochim Acta* 2002, 90:253–258.
139. Nishi T, Nakada M, Suzuki C, Shibata H, Itoh A, Akabori M, Hirata M: Local and Electronic Structure of Am_2O_3 and AmO_2 with XAFS Spectroscopy. *Journal of Nuclear Materials* 2010, 401:138–142.
140. Yaita T, Tachimori S, Edelstein NM, Bucher JJ, Rao L, Shuh DK, Allen PG: EXAFS Studies of Americium (III)-Benzimidazole Complex in Ethanol *J Synchrotron Rad* 2001, 8:663–665.
141. Schulz WW: The Chemistry of Americium In. Oak Ridge: Atlantic Richfield Hanford Company; 1976: 286.
142. Conradson SD, Clark DL, Neu MP, W.Runde, Tait CD: Characterizing the Plutonium Aquo Ions by XAFS Spectroscopy. In: *Challenges in Plutonium Science*. vol. 26. Los Alamos: LANL; 2000: 418-421.
143. Hay PJ, Martin RL, Schreckenbach G: Theoretical Studies of the Properties and Solution Chemistry of AnO_2^{2+} and AnO_2^{+} Aquo Complexes for An) U, Np, and Pu. *J Phys Chem A* 2000, 104:6259-6270.
144. Reich T, Geipel G, Funke H, Hennig C, Roßberg A, Bernhard G: XANES and EXAFS measurements of plutonium hydrates. In: *Biannual Report, Project-Group ESRF-Beamline (ROBL-CRG), FZR-322*. 2001.
145. Ikeda-Ohno A, Hennig C, Tsushima S, Scheinost AC, Bernhard G, Yaita T: Speciation and Structural Study of U(IV) and -(VI) in Perchloric and Nitric Acid Solutions. *Inorg Chem* 2009, 48:7201–7210.
146. Forbes TZ: The Crystal Chemistry of Neptunium Compounds: Structural Relationships to U^{6+} Mineralogy. Notre Dame: University of Notre Dame; 2007.
147. Carlson VA, Stacy AM: Six New Bi(V) Materials: $LiSr_3BiO_6$, $NaSr_3BiO_6$, $NaBa_3BiO_6$, Li_6KBiO_6, Li_6RbBiO_6, and $Li_2Ba_2Bi_2O_{11}$. *Journal of Solid State Chemistry* 1992, 96:332-343.
148. DGA resins. In. Edited by Eichrom Technologies LAGC; 2013.
149. Americium, An Overview. In. Edited by Muljadi P: 43.
150. Templeton DH, Zalkin A, Ruben H, Templeton LK: Redetermination and Absolute Configuration of Sodium Uranyl(VI) Triacetate. *Acta Cryst* 1985, C41:1439-1441.
151. Zachariasen WH, Plettinger HA: Crystal Chemical Studies of the 5f-Series of Elements. XXV: The Crystal Structure of Sodium Uranyl Acetate. *Acta Cryst* 1959, 12:526-530.
152. McWhan DB, Cunningham BB, Wallmann JC: Crystal Structure, Thermal Expansion and Melting Point of Americium Metal. *Journal of Inorganic and Nuclear Chemistry* 1962, 24(9).
153. Burns JH, Musikas C: Crystal Structure of Barium Neptunyl(V) Triacetate Dihydrate. *Inorganic Chemistry* 1977, 16(7):1619-1622.
154. Dholabhai PP: Probing the 5f Electrons: A Relativistic DFT Study of Americium Surfaces Arlington: The University of Texas at Arlington 2008.
155. Vallet V, Privalov T, Wahlgren U, Grenthe I: The Mechanism of Water Exchange in $AmO_2(H_2O)_5^{2+}$ and in the Isoelectronic $UO_2(H_2O)_5^{+}$ and $NpO_2(H_2O)_5^{2+}$

Complexes as Studied by Quantum Chemical Methods. *J Am Chem Soc* 2004, 126:7766-7767.
156. Tsushima S, Wahlgren U, Grenthe I: Quantum Chemical Calculations of Reduction Potentials of AnO_2^{2+}/AnO_2^{+} (An = U, Np, Pu, Am) and Fe^{3+}/Fe^{2+} Couples. *J Phys Chem A* 2006, 110:9175-9182.
157. Notter FP, Dubillard S, Bolvina H: A theoretical study of the excited states of AmO2n+, n=1,2,3. *J Chem Phys* 2008, 128:164315.
158. Pomogaev V, Tiwari SP, Rai N, Goff GS, Runde W, Schneider WF, Maginn EJ: Development and application of effective pairwise potentials for UO2 n+, NpO2 n+, PuO2 n+, and AmO2 n+ (n = 1, 2) ions with water. *Phys Chem* 2013, 15:15954
159. Seminario JM, Concha MC, Politzer P: Calculation of Molecular Geometries and Energies by a Local Density Functional Approach. *International Journal of Quantum Chemistry: Quantum Chemistry Symposium* 1991, 25:249-259
160. Delley B: An All-Electron Numerical Method for Solving the Local Density Functional for Polyatomic Molecules. *J Chem Phys* 1990, 92(1):508-517.
161. Delley B: The Conductor-Like Screening Model for Polymers and Surfaces. *Molecular Simulation* 2006, 32(2).
162. Datasheet: DMol3. In: *accelryscom.* 2011.
163. Perdew JP, Burke K, Ernzerhof M: Generalized Gradient Approximation Made Simple, *Phys Rev Letters* 1996, 77(18):3865-3868.
164. Perdew JP, Wang Y: Accnrate and Simple Snalytic Representation of the Electron-Gas Correlation Energy. *Phys Rev B* 1992, 45(23):244-249.
165. Shamov GA, Schreckenbach G, Martin RL, Hay P: Crown Ether Inclusion Complexes of the Early Actinide Elements, $[AnO_2(18\text{-crown-}6)]^{n+}$, An = U, Np, Pu and n = 1, 2: A Relativistic Density Functional Study. *J Inorg Chem* 2008, 47(5):1465-1475.
166. Hehre WJ, Radom L, Schleyer PR, Pople JA: Ab Initio Molecular Orbital Theory. New York: Wiley 1986.
167. Weck PR, Kim E, Balakrishnan N, Poineau F, Yeamans CB, Czerwinski KR: First-priciples Study of Single-crystal Uranium Mono- and Dinitride. *Chemical Physics Letters* 2007, 443:82-86.
168. Smith NA: Speciation and Spectroscopy of the Uranyl and Tetravalent Plutonium Nitrate Systems: Fundamental Studies and Applications to Used Fuel Reprocessing. Las Vegas: University of Nevada, Las Vegas; 2010.
169. Weck PF, Gong C-MS, Kim E, Thuery P, Czerwinski KR: One-dimensional uranium-organic coordination polymers: crystal and electronic structures of uranyl-diacetohydroxamate. *Dalton Trans* 2011, 40.
170. Weck PF, Kim E, Masci B, Thuery P, Czerwinski KR: Density Functional Analysis of the Trigonal Uranyl Equatorial Coordination in Hexahomotrioxacalix[3]arene-Based Macrocyclic Complexes. *Inorg Chem* 2010, 49.
171. Manolopoulos DE, May JC, Down SE: Theoretical studies of the fullerenes: C34 to C70. *Chem Phys Lett* 1991, 181(2):105-111.
172. Hard and Soft Acids and Bases. Stroudsburg, PA: Dowden, Hutchinson and Ross; 1973.

173. Davidson ER, Chakravorty S: A Test of the Hirshfeld Definition of Atomic Charges and Moments. *Theoretica chimica acta* 1992 83(5-6):319-330.
174. Heathman S, Rueff JP, Simonelli L, Denecke MA, Griveau JC, Caciuffo R, Lander GH: Resonant X-ray Emission Spectroscopy at the L_3 Edge of Americium Up to 23 GPa. *Physical Review B* 2010, 82:201103-201101 - 201103-201104.

VITA

Graduate College
University of Nevada, Las Vegas

Catherine Lynn Riddle

Degrees:

Bachelor of Science, Chemistry 2000
Idaho State University
Master of Science, Chemistry 2005
University of Idaho

Special Honors and Awards:

INL Exceptional Contribution Award, PINS Army support
INL Exceptional Contribution Award, FPEX

Patents:

Patent # **US 7,291,316 B2**, issued Nov. 6, 2007
Patent # **US 7,524,469 B2** issued Apr. 28, 2009
Patent # **US 8,158,088 B2** issued Apr. 17, 2012

Publications:

R. Arnold, C. Augier, A.S. Barabash, A. Basharina-Freshville, S. Blondel, S. Blot, M. Bongrand, V. Brudanin, J. Busto, A.J. Caffrey, P. Čermák, C. Cerna, A. Chapon, E. Chauveau, L. Dragounová, D. Duchesneau, D. Durand, V. Egorov, G. Eurin, J.J. Evans, R. Flack, X. Garrido, H. Gómez, B. Guillon, P. Guzowski, R. Hodák, P. Hubert, C. Hugon, J. Hůlka, S. Jullian, A. Klimenko, O. Kochetov, S.I. Konovalov, V. Kovalenko, D. Lalanne, K. Lang, Y. Lemière, Z. Liptak, P. Loaiza, G. Lutter, F. Mamedov, C. Marquet, F. Mauger, B. Morgan, J. Mott, I. Nemchenok, M. Nomachi, F. Nova, F. Nowacki, H. Ohsumi, R.B. Pahlka, F. Perrot, F. Piquemal, P. Povinec, Y.A. Ramachers, A. Remoto, J.L. Reyss, B. Richards, **C.L. Riddle**, E. Rukhadze, N. Rukhadze, R. Saakyan, X. Sarazin, Yu. Shitov, L. Simard, F. Šimkovic, A. Smetana, K. Smolek, A. Smolnikov, S. Söldner-Rembold, B. Soulé[j], I. Štekl, J. Suhonen, C.S. Sutton, G. Szklarz, J. Thomas, V. Timkin, S. Torre, V.I. Tretyak, Vl.I. Tretyak, V. Umatov, C. Vilela, V. Vorobel, G. Warot, D. Waters, A. Žukauskas, Investigation of double beta decay of ^{100}Mo to excited states of ^{100}Ru, *Nuclear Physics A*, vol. 925, pp. 25-36, May 2014.

P. Paviet, C.L Riddle, K. Campbell, E. Mausolf, Overview of Reductants Utilized In Nuclear Fuel Reprocessing or recycling, Global, American Nuclear Society conference paper, Sept 29, 2013.

P.R. Zalupski, D.D. Ensor, C.L. Riddle, D.R. Peterman, Complete Recovery of Actinides from UREX-Like Raffinates Using a Combination of Hard and Soft Donor Ligands, *Sol. Extr. and Ion Exch.*, vol. 31, pp. 430-441, 2013.

B.J. Mincher, S.P. Mezyk, G. Elias, G.S. Groenewold, C.L. Riddle, L.G. Olson, The Radiation Chemistry of CMPO: Part 1. Gamma Radiolysis, *Sol. Extr. & Ion Exch.* vol. 31, pp. 715-730, 2013.

K.L. Swancutt, T.D. Cullen, S.P. Mezyk1, G. Elias, W.F. Bauer, R.D. Ball, D.R. Peterman, C.L. Riddle, B.J. Mincher, J.J. Muller, The Radiation Chemistry of the Cs-7SB Modifier used in Cs and Sr Solvent Extraction, *Solv. Extr. Ion Exch*, vol 29, pp. 106-127, 2011.

R. Arnold, C. Augier, A.S. Barabash, A. Basharina-Freshville, S. Blondel, S. Blot, M. Bongrand, V. Brudanin, J. Busto, A.J. Caffrey, P. Čermák, C. Cerna, A. Chapon, E. Chauveau, L. Dragounová, D. Duchesneau, D. Durand, V. Egorov, G. Eurin, J.J. Evans, R. Flack, X. Garrido, H. Gómez, B. Guillon, P. Guzowski, R. Hodák, P. Hubert, C. Hugon, J. Hůlka, S. Jullian, A. Klimenko, O. Kochetov, S.I. Konovalov, V. Kovalenko, D. Lalanne, K. Lang, Y. Lemière, Z. Liptak, P. Loaiza, G. Lutter, F. Mamedov, C. Marquet, F. Mauger, B. Morgan, J. Mott, I. Nemchenok, M. Nomachi, F. Nova, F. Nowacki, H. Ohsumi, R.B. Pahlka, F. Perrot, F. Piquemal, P. Povinec, Y.A. Ramachers, A. Remoto, J.L. Reyss, B. Richards, **C.L. Riddle**, E. Rukhadze, N. Rukhadze, R. Saakyan, X. Sarazin, Yu. Shitov, L. Simard, F. Šimkovic, A. Smetana, K. Smolek, A. Smolnikov, S. Söldner-Rembold, B. Soulé[j], I. Štekl, J. Suhonen, C.S. Sutton, G. Szklarz, J. Thomas, V. Timkin, S. Torre, V.I. Tretyak, Vl.I. Tretyak, V. Umatov, C. Vilela, V. Vorobel, G. Warot, D. Waters, A. Žukauskas, Probing Neutrinoless Double Beta Decay Physics with SuperNEMO, *Eur. Phys.J.*, C70, pp. 927-943, 2010.

J. Argyriades, R. Arnold, C. Augier, A.S. Barabash, A. Basharina-Freshville, S. Blondel, S. Blot, M. Bongrand, V. Brudanin, J. Busto, A.J. Caffrey, P. Čermák, C. Cerna, A. Chapon, E. Chauveau, L. Dragounová, D. Duchesneau, D. Durand, V. Egorov, G. Eurin, J.J. Evans, R. Flack, X. Garrido, H. Gómez, B. Guillon, P. Guzowski, R. Hodák, P. Hubert, C. Hugon, J. Hůlka, S. Jullian, A. Klimenko, O. Kochetov, S.I. Konovalov, V. Kovalenko, D. Lalanne, K. Lang, Y. Lemière, Z. Liptak, P. Loaiza, G. Lutter, F. Mamedov, C. Marquet, F. Mauger, B. Morgan, J. Mott, I. Nemchenok, M. Nomachi, F. Nova, F. Nowacki, H. Ohsumi, R.B. Pahlka, F. Perrot, F. Piquemal, P. Povinec, Y.A. Ramachers, A. Remoto, J.L. Reyss, B. Richards, **C.L. Riddle**, E. Rukhadze, N. Rukhadze, R. Saakyan, X. Sarazin, Yu. Shitov, L. Simard, F. Šimkovic, A. Smetana, K. Smolek, A. Smolnikov, S. Söldner-Rembold, B. Soulé[j], I. Štekl, J. Suhonen, C.S. Sutton, G. Szklarz, J. Thomas, V. Timkin, S. Torre, V.I. Tretyak, Vl.I. Tretyak, V. Umatov, C. Vilela, V. Vorobel, G. Warot, D. Waters, A. Žukauskas,, Spectral Modeling of Scintillator for NEMO-3 and SuperNEMO Detectors, *Nuclear Instruments and Methods in Physics Research Section A*, vol. 625(1), pp. 20-28, 2010.

B.J. Mincher, S.P. Mezyk, W.F. Bauer, G. Elias, C.L. Riddle, D.R. Peterman, FPEX γ-Radiolysis in the Presence of Nitric Acid, *Solv. Extr. Ion Exch*, vol 25(5), pp. 593-601, 2007.

C.L. Riddle, J.D. Baker, J.D. Law, C.A. McGrath, D.H. Meikrantz, B.J. Mincher, D.R. Peterman, T.A. Todd, Fission Product Extraction (FPEX): Development of A Novel Solvent for the Simultaneous Separation of Strontium and Cesium from Acidic Solutions, *Solv. Extr. Ion Exch.*, vol. 23, pp. 449-461, 2005.

B.J. Mincher, R.V. Fox, C.L. Riddle, D.C. Cooper, G.S. Groenewold, Strontium and Cesium Sorption to Snake River Plain, Idaho Soil, *Radiochim. Acta*, 92, pp. 55–61, 2004.

R.J. Gehrke, J.D. Baker, J.K. Hartwell, C.L. Riddle, C.A. McGrath, Measurement of Neutron-to-g-ray production ratios from (a, n) Reactions for their Application to Assey TRU Waste, *Nuclear instruments and Methods in Physics Research Section A*, vol. 511, issue 3, pp. 444-456, 2003.

Dissertation Title: Speciation Behavior of Americium Higher Oxidation States for the Separation of Americium from Curium

Dissertation Examination Committee:
Chairperson, Dr. Kenneth Czerwinski, Ph.D.
Committee Member, Dr. Patricia Paviet, Ph.D.
Committee Member, Dr. Gordon Jarvinen, Ph.D.
Graduate Faculty Representative, Dr. Ralf Sudowe, Ph.D.